

NEW CONSTRAINTS ON Ω_M , Ω_Λ , AND w FROM AN INDEPENDENT SET OF 11 HIGH-REDSHIFT SUPERNOVAE OBSERVED WITH THE *HUBBLE SPACE TELESCOPE*¹

R. A. KNOP,^{2,3,4} G. ALDERING,^{4,5} R. AMANULLAH,⁶ P. ASTIER,⁷ G. BLANC,^{5,7} M. S. BURNS,⁸ A. CONLEY,^{5,9} S. E. DEUSTUA,^{5,10} M. DOI,¹¹ R. ELLIS,¹² S. FABBRO,^{4,13} G. FOLATELLI,⁶ A. S. FRUCHTER,¹⁴ G. GARAVINI,⁶ S. GARMOND,^{5,9} K. GARTON,⁸ R. GIBBONS,⁵ G. GOLDBABER,^{5,9} A. GOOBAR,⁶ D. E. GROOM,^{4,5} D. HARDIN,⁷ I. HOOK,¹⁵ D. A. HOWELL,⁵ A. G. KIM,^{4,5} B. C. LEE,⁵ C. LIDMAN,¹⁶ J. MENDEZ,^{17,18} S. NOBILI,⁶ P. E. NUGENT,^{4,5} R. PAIN,⁷ N. PANAGIA,¹⁴ C. R. PENNYPACKER,⁵ S. PERLMUTTER,⁵ R. QUIMBY,⁵ J. RAUX,⁷ N. REGNAULT,^{5,19} P. RUIZ-LAPUENTE,¹⁸ G. SAINTON,⁷ B. SCHAEFER,²⁰ K. SCHAHMANECHE,⁷ E. SMITH,² A. L. SPADAFORA,⁵ V. STANISHEV,⁶ M. SULLIVAN,^{12,21} N. A. WALTON,²² L. WANG,⁵ W. M. WOOD-VASEY,^{5,9} AND N. YASUDA²³ (THE SUPERNOVA COSMOLOGY PROJECT)

Received 2003 May 24; accepted 2003 July 16

ABSTRACT

We report measurements of Ω_M , Ω_Λ , and w from 11 supernovae (SNe) at $z = 0.36$ – 0.86 with high-quality light curves measured using WFPC2 on the *Hubble Space Telescope* (HST). This is an independent set of high-redshift SNe that confirms previous SN evidence for an accelerating universe. The high-quality light curves available from photometry on WFPC2 make it possible for these 11 SNe alone to provide measurements of the cosmological parameters comparable in statistical weight to the previous results. Combined with earlier Supernova Cosmology Project data, the new SNe yield a measurement of the mass density $\Omega_M = 0.25^{+0.07}_{-0.06}$ (statistical) ± 0.04 (identified systematics), or equivalently, a cosmological constant of $\Omega_\Lambda = 0.75^{+0.06}_{-0.07}$ (statistical) ± 0.04 (identified systematics), under the assumptions of a flat universe and that the dark energy equation-of-state parameter has a constant value $w = -1$. When the SN results are combined with independent flat-universe measurements of Ω_M from cosmic microwave background and galaxy redshift distortion data, they provide a measurement of $w = -1.05^{+0.15}_{-0.20}$ (statistical) ± 0.09 (identified systematic), if w is assumed to be constant in time. In addition to high-precision light-curve measurements, the new data offer greatly improved color measurements of the high-redshift SNe and hence improved host galaxy extinction estimates. These extinction measurements show no anomalous negative $E(B-V)$ at high redshift. The precision of the measurements is such that it is possible to perform a host galaxy extinction correction directly for individual SNe without any assumptions or priors on the parent $E(B-V)$ distribution. Our cosmological fits using full extinction corrections confirm that dark energy is required with $P(\Omega_\Lambda > 0) > 0.99$, a result consistent with previous and current SN analyses that rely on the identification of a low-extinction subset or prior assumptions concerning the intrinsic extinction distribution.

Subject headings: cosmological parameters — cosmology: observations — supernovae: general

¹ Based in part on observations made with the NASA/ESA *Hubble Space Telescope*, obtained at the Space Telescope Science Institute, which is operated by the Association of Universities for Research in Astronomy, Inc., under NASA contract NAS 5-26555. These observations are associated with programs GO-7336, GO-7590, and GO-8346. Some of the data presented herein were obtained at the W. M. Keck Observatory, which is operated as a scientific partnership among the California Institute of Technology, the University of California, and the National Aeronautics and Space Administration. The Observatory was made possible by the generous financial support of the W. M. Keck Foundation. Based in part on observations obtained at the WIYN Observatory, which is a joint facility of the University of Wisconsin at Madison, Indiana University, Yale University, and the National Optical Astronomy Observatory. Based in part on observations made with the European Southern Observatory telescopes (ESO programs 60.A-0586 and 265.A-5721). Based in part on observations made with the Canada-France-Hawaii Telescope, operated by the National Research Council of Canada, le Centre National de la Recherche Scientifique de France, and the University of Hawaii.

² Department of Physics and Astronomy, Vanderbilt University, P.O. Box 1803, Station B, Nashville, TN 37240.

³ Visiting Astronomer, Kitt Peak National Observatory, National Optical Astronomy Observatory, which is operated by the Association of Universities for Research in Astronomy (AURA), Inc., under cooperative agreement with the National Science Foundation.

⁴ Visiting Astronomer, Cerro Tololo Inter-American Observatory, National Optical Astronomy Observatory, which is operated by the Association of Universities for Research in Astronomy (AURA), Inc., under cooperative agreement with the National Science Foundation.

⁵ E. O. Lawrence Berkeley National Laboratory, 1 Cyclotron Road, Berkeley, CA 94720.

⁶ Department of Physics, Stockholm University, SCFAB, S-106 91 Stockholm, Sweden.

⁷ Laboratoire de Physique Nucléaire et de Haute Energies, CNRS-IN2P3, University of Paris VI and VII, Paris, France.

⁸ Colorado College, 14 East Cache La Poudre Street, Colorado Springs, CO 80903.

⁹ Department of Physics, University of California at Berkeley, 366 LeConte Hall, Berkeley, CA 94720-7300.

¹⁰ American Astronomical Society, 2000 Florida Avenue, NW, Suite 400, Washington, DC 20009.

¹¹ Department of Astronomy, and Research Center for the Early Universe, School of Science, University of Tokyo, Bunkyo-ku, Tokyo 113-0033, Japan.

¹² California Institute of Technology, East California Boulevard, Pasadena, CA 91125.

¹³ Centro, Multidisciplinar de Astrofísica, Instituto Superior Técnico, P-1300 Lisbon, Portugal.

¹⁴ Space Telescope Science Institute, 3700 San Martin Drive, Baltimore, MD 21218.

¹⁵ Department of Physics, University of Oxford, Nuclear and Astrophysics Laboratory, Keble Road, Oxford OX1 3RH, UK.

¹⁶ European Southern Observatory, St. Alonso de Córdova 3107, Vitacura, Casilla 19001, Santiago 19, Chile.

¹⁷ Isaac Newton Group of Telescopes, Apartado de Correos 321, Santa Cruz de La Palma, E-38780 Canary Islands, Spain.

¹⁸ Department of Astronomy, University of Barcelona, E-08028 Barcelona, Spain.

¹⁹ Now at Laboratoire Leprince-Ringuet, CNRS-IN2P3, Ecole Polytechnique, Palaiseau, France.

²⁰ Department of Astronomy, University of Texas at Austin, RLM 15.308, Austin, TX 78712.

²¹ Department of Physics, University of Durham, South Road, Durham DH1 3LE, UK.

²² Institute of Astronomy, University of Cambridge, Madingley Road, Cambridge CB3 0HA, UK.

²³ National Astronomical Observatory of Japan, 2-21-1, Ohsawa, Mitaka, Tokyo 181-8588, Japan.

1. INTRODUCTION

Five years ago, the Supernova Cosmology Project (SCP) and the High- z Supernova Search Team both presented studies of distant Type Ia supernovae (SNe Ia) in a series of reports, which gave strong evidence for an acceleration of the universe's expansion, and hence for a nonzero cosmological constant, or dark energy density (Perlmutter et al. 1998, 1999, hereafter P99; Garnavich et al. 1998a; Schmidt et al. 1998; Riess et al. 1998; for a review see Perlmutter & Schmidt 2003). These results ruled out a flat, matter-dominated ($\Omega_M = 1$, $\Omega_\Lambda = 0$) universe. For a flat universe, motivated by inflation theory, these studies yielded a value for the cosmological constant of $\Omega_\Lambda \simeq 0.7$. Even in the absence of assumptions about the geometry of the universe, the SN measurements indicate the existence of dark energy with greater than 99% confidence.

The SN results combined with observations of the power spectrum of the cosmic microwave background (CMB; e.g., Jaffe et al. 2001; Bennett et al. 2003; Spergel et al. 2003), the properties of massive clusters (e.g., Turner 2001; Allen, Schmidt, & Fabian 2002; Bahcall et al. 2003), and dynamical redshift-space distortions (Hawkins et al. 2002) yield a consistent picture of a flat universe with $\Omega_M \simeq 0.3$ and $\Omega_\Lambda \simeq 0.7$ (Bahcall et al. 1999). Each of these measurements is sensitive to different combinations of the parameters; hence, they complement each other. Moreover, because there are three different measurements of two parameters, the combination provides an important consistency check. While the current observations of galaxy clusters and dynamics, as well as of high-redshift SNe, primarily probe the “recent” universe at redshifts of $z < 1$, the CMB measurements probe the early universe at $z \sim 1100$. That consistent results are obtained by measurements of vastly different epochs of the universe's history suggests a vindication of the standard model of the expanding universe.

In the redshift range around $z = 0.4$ – 0.7 , the SN results are most sensitive to a linear combination of Ω_M and Ω_Λ close to $\Omega_M - \Omega_\Lambda$. In contrast, galaxy clustering and dynamics are sensitive primarily to Ω_M alone, while the CMB is most sensitive to $\Omega_M + \Omega_\Lambda$. Although combinations of other measurements lead to a separate confirmation of the universe's acceleration (e.g., Efstathiou et al. 2002), taken alone it is the SNe that provide the best *direct* evidence for dark energy. Therefore, it is of importance to improve the precision of the SN result, to confirm the result with additional independent high-redshift SNe, and also to limit the possible effects of systematic errors.

Perlmutter et al. (1997) P99, and Riess et al. (1998) presented extensive accounts of, and bounds for, possible systematic uncertainties in the SN measurements. One obvious possible source of systematic uncertainty is the effect of host galaxy dust. For a given mass density, the effect of a cosmological constant on the magnitudes of high-redshift SNe is to make their observed brightnesses *dimmer* than would have been the case with $\Omega_\Lambda = 0$. Dust extinction from within the host galaxy of the high-redshift SNe could have a similar effect; however, normal dust will also redden the colors of the SNe. Therefore, a measurement of the color of the high-redshift SNe, compared to the known colors of low-redshift SNe Ia, has been used to provide an upper limit on the effect of host galaxy dust extinction or a direct measurement of that extinction that may then be corrected. Uncertainties on extinction corrections based on these color

measurements usually dominate the statistical error of photometric measurements. Previous analyses either have selected a low-extinction subset of both low- and high-redshift SNe and not applied corrections directly (“fit C,” the primary analysis of P99) or have used an asymmetric Bayesian prior on the intrinsic extinction distribution to limit the propagated uncertainties from errors in color measurements (Riess et al. 1998; “fit E” of P99).

In Sullivan et al. (2003), we set stronger limits on the effects of host galaxy extinction by comparing the extinction, cosmological parameters, and SN peak magnitude dispersion for subsets of the SCP SNe observed in different types of host galaxies, as identified from both *HST* imaging and Keck spectroscopy of the hosts. We found that SNe in early-type (E and S0) galaxies show a smaller dispersion in peak magnitude at high redshift, as had previously been seen at low redshift (e.g., Wang, Hoefflich, & Wheeler 1997). This subset of the P99 sample—in hosts unlikely to be strongly affected by extinction—independently provided evidence at the 5σ level that $\Omega_\Lambda > 0$ in a flat universe and confirmed that host galaxy dust extinction was unlikely to be a significant systematic in the results of P99, as had been suggested previously (e.g., Rowan-Robinson 2002). The natural next step following the work of Sullivan et al. (2003)—presented in the current paper—is to provide high-quality individual unbiased $E(B-V)$ measurements that allow us to directly measure the effect of host galaxy extinction on each SN event without resorting to a prior on the color excess distribution.

The current paper presents 11 new SNe discovered and observed by the SCP at redshifts $0.36 < z < 0.86$, a range very similar to that of the 42 high-redshift SNe reported in P99. The SNe of that paper, with one exception, were observed entirely with ground-based telescopes; 11 of the 14 new SNe reported by Riess et al. (1998) were also observed from the ground. The 11 SNe of this work have light curves in both the R and I bands measured with the Wide Field Planetary Camera 2 (WFPC2) on the *Hubble Space Telescope* (*HST*) and represent the largest sample to date of *HST*-measured SNe Ia at high redshift.

The *HST* provides two primary advantages for photometry of point sources such as SNe. First, the sky background is much lower, allowing a much higher signal-to-noise ratio in a single exposure. Second, because the telescope is not limited by atmospheric seeing, it has very high spatial resolution. This helps the signal-to-noise ratio by greatly reducing the area of background emission that contributes to the noise of the source measurement and, moreover, simplifies the task of separating the variable SN signal from the host galaxy. With these advantages, the precision of the light-curve and color measurements is much greater for the 11 SNe in this paper than was possible for previous ground-based observations. These 11 SNe themselves provide a high-precision *new* set of high-redshift SNe to test the accelerating universe results. Moreover, the higher precision light-curve measurements in both R and I bands allow us to make high-quality, unbiased, individual host galaxy extinction corrections to each SN event.

We first describe the point-spread function (PSF) fit photometry method used for extracting the light curves from the WFPC2 images (§ 2.1). Next, in § 2.2 we describe the light-curve fitting procedure, including the methods used for calculating accurate K -corrections. So that all SNe may be treated consistently, in § 2.3 we apply the slightly

updated K -correction procedure to all of the SNe used in P99. In § 2.4 the cosmological fit methodology we use is described. In § 3 we discuss the evidence for host galaxy extinction (only significant for three of the 11 new SNe) from the $R-I$ light-curve colors. In § 4.1 we present the measurements of the cosmological parameters Ω_M and Ω_Λ from the new data set alone, as well as combining this set with the data of P99. In § 4.2 we perform a combined fit with our data and the high-redshift SNe of Riess et al. (1998). Finally, in § 4.3 we present measurements of w , the dark energy equation-of-state parameter, from these data, and from these data combined with recent CMB and galaxy redshift distortion measurements. These discussions of our primary results are followed by updated analyses of systematic uncertainties for these measurements in § 5.

2. OBSERVATIONS, DATA REDUCTION, AND ANALYSIS

2.1. WFPC2 Photometry

The SNe discussed in this paper are listed in Table 1. They were discovered during three different SN searches, following the techniques described in Perlmutter et al. (1995, 1997) and P99. Two of the searches were conducted with the 4 m Blanco telescope at the Cerro Tololo Inter-American Observatory (CTIO), in 1997 November/December and 1998 March/April. The final search was conducted at the Canada-France-Hawaii Telescope (CFHT) on Mauna Kea in Hawaii in 2000 April/May. In each case, two to three nights of reference images were followed 3–4 weeks later by two to three nights of search images. The two images of each search field were seeing-matched and subtracted, and they were searched for residuals indicating an SN candidate. Weather conditions limited the depth and hence the redshift range of the 1998 March/April search. Out of the three searches, 11 of the resulting SN discoveries were followed with extensive *HST* photometry. These SNe are spaced approximately evenly in the redshift range $0.3 < z < 0.9$. Nine out of the 11 SNe were discovered very close to maximum light; two were discovered several days before maximum light.

Spectra were obtained with the red side of LRIS on the Keck 10 m telescope (Oke et al. 1995), with FORS1 on Antu (VLT-UT1; Appenzeller et al. 1998) and with EFOSC2²⁴ on the ESO 3.6 m telescope. These spectra were used to confirm the identification of the candidates as SNe Ia and to measure the redshift of each candidate. Nine of the 11 SNe in the set have strong confirmation as Type Ia through the presence of Si II $\lambda 6150$, Si II $\lambda 4130$, or Fe II features that match those of a Type Ia observed at a similar epoch. SN 1998ay and SN 1998be have spectra that are consistent with SN Ia spectra, although this identification is less secure for those two. However, we note that the colors (measured at multiple epochs with the *HST* light curves) are inconsistent with other non-Ia types. (We explore the systematic effect of removing those two SNe from the set in § 5.2.)

Where possible, the redshift, z , of each candidate was measured by matching narrow features in the host galaxy of the SNe; the precision of these measurements in z is typically 0.001. In cases in which there were not sufficient host galaxy

features (SN 1998aw and SN 1998ba), redshifts were measured from the SN itself; in these cases, z is measured with a (conservative) precision of 0.01 (Branch & van den Bergh 1993). Even in the latter case, redshift measurements do not contribute significantly to the uncertainties in the final cosmological measurements since these are dominated by the photometric uncertainties.

Each of these SNe was imaged with two broadband filters using the Planetary Camera (PC) CCD of the WFPC2 on the *HST*, which has a scale of $0''.046 \text{ pixel}^{-1}$. Table 1 lists the dates of these observations. The F675W and F814W broadband filters were chosen to have maximum sensitivity to these faint objects, while being as close a match as practical to the rest-frame B and V filters at the targeted redshifts. (Note that all of our WFPC2 observing parameters except the exact target coordinates were fixed prior to the SN discoveries.) The effective system transmission curves provided by the Space Telescope Science Institute indicate that, when used with WFPC2, F675W is most similar to ground-based R band while F814W is most similar to ground-based I band. These filters roughly correspond to redshifted B - and V -band filters for the SNe at $z < 0.7$ and redshifted U - and B -band filters for the SNe at $z > 0.7$.

The *HST* images were reduced through the standard *HST* “on-the-fly reprocessing” data reduction pipeline provided by the Space Telescope Science Institute. Images were then background subtracted, and images taken in the same orbit were combined to reject cosmic rays using the “crrej” procedure (a part of the STSDAS IRAF package). Photometric fluxes were extracted from the final images using a PSF-fitting procedure. Traditional PSF-fitting procedures assume a single isolated point source above a constant background. In this case, the point source was superimposed on the image of the host galaxy. In all cases, the SN image was separated from the core of the host galaxy; however, in most cases the separation was not enough that an annular measurement of the background would be accurate. Because the host galaxy flux is the same in all of the images, we used a PSF-fitting procedure that fits a PSF *simultaneously* to every image of a given SN observed through a given photometric filter. The model we fit was

$$f_i(x, y) = f_{0i} \text{PSF}(x - x_{0i}, y - y_{0i}) + \text{bg}(x - x_{0i}, y - y_{0i}; a_j) + p_i, \quad (1)$$

where $f_i(x, y)$ is the measured flux in pixel (x, y) of the i th image, (x_{0i}, y_{0i}) is the position of the SN on the i th image, f_{0i} is the total flux in the SN in the i th image, $\text{PSF}(u, v)$ is a normalized PSF, $\text{bg}(u, v; a_j)$ is a temporally constant background parametrized by a_j , and p_i is a pedestal offset for the i th image. There are $4n + m - 1$ parameters in this model, where n is the number of images (typically 2, 5, or 6 previously summed images) and m is the number of parameters a_j that specify the background model (typically 3 or 6). (The -1 is due to the fact that a zeroth-order term in the background is degenerate with one of the p_i terms.) Parameters varied include f_{0i} , x_{0i} , y_{0i} , p_i , and a_j .

Because of the scarcity of objects in our PC images, geometric transformations between the images at different epochs using other objects on the four chips of WFPC2 together allowed an a priori determination of (x_{0i}, y_{0i}) good to ~ 1 pixel. Allowing those parameters to vary in the fit (effectively, using the point-source signature of the SN to determine the offset of the image) provided position

²⁴ See <http://www.la.eso.org/lasilla/sciops/efosc>.

TABLE 1
WFPC2 SUPERNOVA OBSERVATIONS

SN Name	z	F675W Observations	F814W Observations
1997ek	0.863	1998 Jan 05 (400 s, 400 s) 1998 Jan 11 (400 s, 400 s)	1998 Jan 05 (500 s, 700 s) 1998 Jan 11 (500 s, 700 s) 1998 Feb 02 (1100 s, 1200 s) 1998 Feb 14 (1100 s, 1200 s) 1998 Feb 27 (1100 s, 1200 s) 1998 Nov 09 (1100 s, 1300 s) 1998 Nov 16 (1100 s, 1300 s)
1997eq	0.538	1998 Jan 06 (300 s, 300 s) 1998 Jan 21 (400 s, 400 s)	1998 Jan 06 (300 s, 300 s) 1998 Jan 11 (300 s, 300 s) 1998 Feb 02 (500 s, 700 s) 1998 Feb 11 (500 s, 700 s)
1997ez	0.778	1998 Feb 19 (400 s, 400 s) 1998 Jan 05 (400 s, 400 s) 1998 Jan 11 (400 s, 400 s)	1998 Feb 19 (500 s, 700 s) 1998 Jan 05 (500 s, 700 s) 1998 Jan 11 (500 s, 700 s) 1998 Feb 02 (1100 s, 1200 s) 1998 Feb 14 (1100 s, 1200 s) 1998 Feb 27 (100 s, 1200 s, 1100 s, 1200 s)
1998as	0.355	1998 Apr 08 (400 s, 400 s) 1998 Apr 20 (400 s, 400 s) 1998 May 11 (400 s, 400 s) 1998 May 15 (400 s, 400 s) 1998 May 29 (400 s, 400 s)	1998 Apr 08 (500 s, 700 s) 1998 Apr 20 (500 s, 700 s) 1998 May 11 (500 s, 700 s) 1998 May 15 (500 s, 700 s) 1998 May 29 (500 s, 700 s)
1998aw	0.440	1998 Apr 08 (300 s, 300 s) 1998 Apr 18 (300 s, 300 s) 1998 Apr 29 (400 s, 400 s) 1998 May 14 (400 s, 400 s) 1998 May 28 (400 s, 400 s)	1998 Apr 08 (300 s, 300 s) 1998 Apr 18 (300 s, 300 s) 1998 Apr 29 (500 s, 700 s) 1998 May 14 (500 s, 700 s) 1998 May 28 (500 s, 700 s)
1998ax	0.497	1998 Apr 08 (300 s, 300 s) 1998 Apr 18 (300 s, 300 s) 1998 Apr 29 (300 s, 300 s) 1998 May 14 (300 s, 300 s) 1998 May 27 (300 s, 300 s)	1998 Apr 08 (300 s, 300 s) 1998 Apr 18 (300 s, 300 s) 1998 Apr 29 (500 s, 700 s) 1998 May 14 (500 s, 700 s) 1998 May 27 (500 s, 700 s)
1998ay	0.638	1998 Apr 08 (400 s, 400 s) 1998 Apr 20 (400 s, 400 s)	1998 Apr 08 (500 s, 700 s) 1998 Apr 20 (500 s, 700 s) 1998 May 11 (1100 s, 1200 s) 1998 May 15 (1100 s, 1200 s) 1998 Jun 03 (1100 s, 1200 s)
1998ba	0.430	1998 Apr 08 (300 s, 300 s) 1998 Apr 19 (300 s, 300 s) 1998 Apr 29 (400 s, 400 s) 1998 May 13 (400 s, 400 s) 1998 May 28 (400 s, 400 s)	1998 Apr 08 (300 s, 300 s) 1998 Apr 19 (300 s, 300 s) 1998 Apr 29 (500 s, 700 s) 1998 May 13 (500 s, 700 s) 1998 May 28 (500 s, 700 s)
1998be	0.644	1998 Apr 08 (300 s, 300 s) 1998 Apr 19 (300 s, 300 s) 1998 Apr 30 (400 s, 400 s) 1998 May 15 (400 s, 400 s) 1998 May 28 (400 s, 400 s)	1998 Apr 08 (300 s, 300 s) 1998 Apr 19 (300 s, 300 s) 1998 Apr 30 (500 s, 700 s) 1998 May 15 (500 s, 700 s) 1998 May 28 (500 s, 700 s)
1998bi	0.740	1998 Apr 06 (400 s, 400 s) 1998 Apr 18 (400 s, 400 s)	1998 Apr 06 (500 s, 700 s) 1998 Apr 18 (500 s, 700 s) 1998 Apr 28 (1100 s, 1200 s) 1998 May 12 (1100 s, 1200 s) 1998 Jun 02 (1100 s, 1200 s)
2000fr	0.543	2000 May 15 (600 s, 600 s) 2000 May 28 (600 s, 600 s) 2000 Jun 10 (500 s, 500 s) 2000 Jun 22 (1100 s, 1300 s) 2000 Jul 08 (1100 s, 1300 s)	2000 May 08 (2200 s) 2000 May 15 (1100 s, 1100 s) 2000 May 28 (600 s, 600 s) 2000 Jun 10 (600 s, 600 s) 2000 Jun 22 (1100 s, 1200 s) 2000 Jul 08 (110 s, 1200 s)

measurements a factor of ~ 10 better.²⁵ The model was fitted to 13×13 pixel patches extracted from all of the images of a time sequence of a single SN in a single filter (except for SN 1998ay, which is close enough to the host galaxy that a 7×7 pixel patch was used to avoid having to fit the core of the galaxy with the background model). In four out of the 99 patches used in the fits to the 22 light curves, a single bad pixel was masked from the fit. The series of f_{0i} values, corrected as described in the rest of this section, provided the data used in the light-curve fits described in § 2.2. For one SN (SN 1997ek at $z = 0.86$), the F814W background was further constrained by an SN-free “final reference” image taken 11 months after the SN explosion.²⁶

A single Tiny Tim PSF (Krist & Hook 2003) was used as PSF(u, v) for all images of a given filter. The Tiny Tim PSF used was subsampled to 10×10 subpixels; in the fit procedure, it was shifted and integrated (properly summing fractional subpixels). After shifting and resampling to the PC pixel scale, it was convolved with an empirical 3×3 electron diffusion kernel with 75% of the flux in the central element (A. Fruchter 2000, private communication).²⁷ The PSF was normalized in a $0''.5$ radius aperture, chosen to match the standard zero-point calibration (Holtzman et al. 1995; Dolphin 2000). Although the use of a single PSF for every image is an approximation (the PSF of WFPC2 depends on the epoch of the observation and the position on the CCD), this approximation should be valid, especially given that for all of the observations the SN was positioned close to the center of the PC. To verify that this approximation is valid, we reran the PSF-fitting procedure with individually generated PSFs for most SNe; we also explored using an SN spectrum instead of a standard-star spectrum in generating the PSF. The measured fluxes were not significantly different, showing differences in both directions generally within 1%–2% of the SN peak flux value, much less than our photometric uncertainties on individual data points.

Although one of the great advantages of the *HST* is its low background, CCD photometry of faint objects over a low background suffers from an imperfect charge transfer efficiency (CTE) effect, which can lead to a systematic underestimate of the flux of point sources (Whitemore, Heyer, & Casertano 1999; Dolphin 2000, 2003).²⁸ On the PC, these effects can be as large as $\sim 15\%$. The measured flux values (f_{0i} above) were corrected for the CTE of WFPC2 following the standard procedure of Dolphin (2000).²⁹ Uncertainties on the CTE corrections were propagated into the corrected SN fluxes, although in all cases these uncer-

tainties were smaller than the uncertainties in the raw measured flux values. Because the host galaxy is a smooth background underneath the point source, it was considered as a contribution to the background in the CTE correction. For an image that was a combination of several separate exposures within the same orbit or orbits, the CTE calculation was performed assuming that each SN image had a measured SN flux whose fraction of the total flux was equal to the fraction of that individual image’s exposure time to the summed image’s total exposure time. This assumption is correct most of the time, with the exception of the few instances where earthshine affects part of an orbit.

In addition to the *HST* data, there exists ground-based photometry for each of these SNe. This includes the images from the search itself, as well as a limited amount of follow-up. The details of which SNe were observed with which telescopes are given with the light curves in the Appendix. Ground-based photometric fluxes were extracted from images using the same aperture photometry procedure of P99. A complete light curve in a given filter (*R* or *I*) combined the *HST* data with the ground-based data (using the color correction procedure described in § 2.3), using measured zero points for the ground-based data and the Vega zero points of Dolphin (2000) for the *HST* data. The uncertainties on those zero points (0.003 for F814W or 0.006 for F675W) were added as correlated errors between all *HST* data points when combining with the ground-based light curve. Similarly, the measured uncertainty in the ground-based zero point was added as a correlated error to all ground-based fluxes. Ground-based photometric calibrations were based on observations of Landolt (1992) standard stars observed on the same photometric night as an SN observation; each calibration is confirmed over two or more nights. Ground-based zero-point uncertainties are generally $\lesssim 0.02$ – 0.03 ; the *R*-band ground-based zero point for SN 1998ay is only good to ± 0.05 . We have compared our ground-based aperture photometry with our *HST* PSF-fitting photometry using the limited number of sufficiently bright stars present in the PC across the 11 SNe fields. We find the difference between the *HST* and ground-based photometry to be 0.02 ± 0.02 in both the *R* and *I* bands, consistent with no offset. The correlated uncertainties between different SNe arising from ground-based zero points based on the same calibration data, as well as between the *HST* SNe (which all share the same zero point), were included in the covariance matrix used in all cosmological fits (see § 2.4).

2.2. Light-Curve Fits

It is the magnitude of the SN at its light-curve peak that serves as a “calibrated candle” in estimating the cosmological parameters from the luminosity-distance relationship. To estimate this peak magnitude, we performed template fits to the time series of photometric data for each SN. In addition to the 11 SNe described here, light-curve fits were also performed to the SNe from P99, including 18 SNe from Hamuy et al. (1996b, hereafter H96) and eight from Riess et al. (1999b, hereafter R99) that match the same selection criteria used for the H96 SNe (having data within 6 days of maximum light and located at $cz > 4000 \text{ km s}^{-1}$, limiting distance modulus error due to peculiar velocities to less than 0.15 mag). Because of new templates and *K*-corrections (see below), light-curve fits to the SNe from H96 and P99 used in

²⁵ Note that this may introduce a bias toward higher flux, as the fit will seek out positive fluctuations on which to center the PSF. However, the covariance between the peak flux and position is typically less than $\sim 4\%$ of the product of the positional uncertainty and the flux uncertainty, so the effects of this bias will be very small in comparison to our photometric errors.

²⁶ Although obtaining final references to subtract the galaxy background is standard procedure for ground-based photometry of high-redshift SNe, the higher resolution of WFPC2 provides sufficient separation between the SN and host galaxy that such images are not always necessary, particularly in this redshift range.

²⁷ See also http://www.stsci.edu/software/tinytim/tinytim_fa.html.

²⁸ Available at http://www.stsci.edu/hst/HST_overview/documents/calworkshop/workshop2002/CW2002_Papers/CW02_dolphin.

²⁹ These CTE corrections used updated coefficients posted on Dolphin’s web page (http://www.noao.edu/staff/dolphin/wfpc2_calib/) in September, 2002.

the analyses below were redone for consistency. The results of these fits are slightly different from those quoted in P99 for the same SNe as a result of the change in the light-curve template, the new K -corrections, and the different fit procedure, all discussed below. For example, because the measured $E(B-V)$ value was considered in the K -corrections (§ 2.3), whereas it was not in P99, one should expect to see randomly distributed differences in fit SN light-curve parameters as a result of scatter in the color measurements.

Light-curve fits were performed using a χ^2 minimization procedure based on MINUIT (James & Roos 1975). For both high- and low-redshift SNe, color corrections and K -corrections are applied (see § 2.3) to the photometric data. These data were then fitted to light-curve templates. Fits were performed to the combined R - and I -band data for each high-redshift SN. For low-redshift SNe, fits were performed using only the B - and V -band data (which correspond to deredshifted R and I bands for most of the high-redshift SNe). The light-curve model fit to the SN has four parameters to modify the light-curve templates: time of rest-frame B -band maximum light, peak flux in R , $R-I$ color at the epoch of rest-frame maximum B -band light, and time-scale stretch s . Stretch is a parameter that linearly scales the time axis, so that an SN with a high stretch has a relatively slow decay from maximum and an SN with a low stretch has a relatively fast decay from maximum (Perlmutter et al. 1997; Goldhaber et al. 2001). For SNe in the redshift range $z = 0.3-0.7$, a B template was fitted to the R -band light curve and a V template was fitted to the I -band light curve. For SNe at $z > 0.7$, a U template was fitted to the R -band light curve and a B template to the I -band light curve. Two of the high-redshift SNe from P99 fall at $z \sim 0.18$ (SN 1997I and SN 1997N); for these SNe, V and R templates were fitted to the R - and I -band data. (The peak B -band magnitude was extracted by adding the intrinsic SN Ia $B-V$ color to the fit V -band magnitude at the epoch of B maximum.)

The B template used in the light-curve fits was that of Goldhaber et al. (2001). For this paper, new V - and R -band templates were generated following a procedure similar to that of Goldhaber et al. (2001), by fitting a smooth parameterized curve through the low-redshift SN data of H96 and R99. A new U -band template was generated with data from Hamuy et al. (1991), Lira et al. (1998), Richmond et al. (1995), Suntzeff et al. (1999), and Wells et al. (1994); comparison of our U -band template shows good agreement with the new U -band photometry from Jha (2002) at the relevant epochs. New templates were generated by fitting a smooth curve, $f(t')$, to the low-redshift light-curve data, where $t' = t/(1+z)/s$; t is the number of observer frame days relative to the epoch of the B -band maximum of each SN, z is the redshift of each SN, and s is the stretch of each SN as measured from the B -band light curves. Light-curve templates had an initial parabola with a 20 day rise time (Aldering, Knop, & Nugent 2000), joined to a smooth spline section to describe the main part of the light curve, then joined to an exponential decay to describe the final tail at greater than ~ 70 days past maximum light. The first 100 days of each of the three templates is listed in Table 2.

Because of a secondary “hump” or “shoulder” ~ 20 days after maximum, the R -band light curve does not vary strictly according to the simple time-axis scaling parameterized by stretch that is so successful in describing the different U -, B -, and V -band light curves. However, for the two $z \sim 0.18$ SNe to which we fit an R -band template, the peak

R - and I -band magnitudes are well constrained, and the stretch is also well measured from the rest-frame V -band light curve.

Some of the high-redshift SNe from P99 lack an SN-free host galaxy image. These SNe were fitted with an additional variable parameter: the zero level of the I -band light curve. The SNe treated in this manner include SN 1997O, SN 1997Q, SN 1997R, and SN 1997am.

The late-time light-curve behavior may bias the result of a light-curve fit (Aldering et al. 2000); it is therefore important that the low- and high-redshift SNe are treated in as consistent a manner as possible. Few or none of the high-redshift SNe have high-precision measurements more than $\sim 40-50$ rest-frame days after maximum light, so as in Perlmutter et al. (1997) and P99 these late-time points were eliminated from the low-redshift light-curve data before the template fit procedure. Additionally, to allow for systematic offset uncertainties on the host galaxy subtraction, an “error floor” of 0.007 times the maximum light-curve flux was applied; any light-curve point with an uncertainty below the error floor had its uncertainty replaced by that value (Goldhaber et al. 2001).

The final results of the light-curve fits, including the effect of color corrections and K -corrections, are listed in Table 3 for the 11 SNe of this paper. Table 4 shows the results of new light-curve fits to the high-redshift SNe of P99 used in this paper (see § 2.5), and Table 5 shows the results of light-curve fits for the low-redshift SNe from H96 and R99.³⁰ The Appendix tabulates all of the light-curve data for the 11 *HST* SNe in this paper. The light curves for these SNe (and the F675W WFPC2 image nearest maximum light) are shown in Figure 1. Note that there are correlated errors between all of the ground-based points for each SN in these figures, as a single ground-based zero point was used to scale each of them together with the *HST* photometry.

2.3. Color and K -Corrections

In order to combine data from different telescopes, color corrections were applied to remove the differences in the spectral responses of the filters relative to the Bessell system (Bessell 1990). For the ground-based telescopes, the filters are close enough to the standard Bessell filters that a single linear color term (measured at each observatory with standard stars) suffices to put the data onto the Bessell system, with most corrections being smaller than 0.01 mag. The WFPC2 filters are different enough from the ground-based filters, however, that a linear term is not sufficient. Moreover, the differences between an SN Ia and standard-star spectral energy distribution are significant. In this case, color corrections were calculated by integrating template SN Ia spectra (described below) through the system response.

In order to perform light-curve template fitting, a cross filter K -correction must be applied to transform the data in the observed filter into a rest-frame magnitude in the filter used for the light-curve template (Kim, Goobar, & Perlmutter 1996). The color correction to the nearest standard Bessell filter followed by a K -correction to a rest-frame filter is equivalent to a direct K -correction from the observed filter to the standard rest-frame filter. In practice,

³⁰ These three tables are available in electronic form from <http://supernova.lbl.gov>.

TABLE 2
U, *V*, AND *R* LIGHT-CURVE TEMPLATES USED

Day ^a	<i>U</i> Flux ^b	<i>V</i> Flux ^b	<i>R</i> Flux ^b	Day ^a	<i>U</i> Flux ^b	<i>V</i> Flux ^b	<i>R</i> Flux ^b
-19.....	6.712E-03	4.960E-03	5.779E-03	31.....	4.790E-02	2.627E-01	3.437E-01
-18.....	2.685E-02	1.984E-02	2.312E-02	32.....	4.524E-02	2.481E-01	3.238E-01
-17.....	6.041E-02	4.464E-02	5.201E-02	33.....	4.300E-02	2.345E-01	3.054E-01
-16.....	1.074E-01	7.935E-02	9.246E-02	34.....	4.112E-02	2.218E-01	2.887E-01
-15.....	1.678E-01	1.240E-01	1.445E-01	35.....	3.956E-02	2.099E-01	2.733E-01
-14.....	2.416E-01	1.785E-01	2.080E-01	36.....	3.827E-02	1.990E-01	2.592E-01
-13.....	3.289E-01	2.430E-01	2.832E-01	37.....	3.722E-02	1.891E-01	2.463E-01
-12.....	4.296E-01	3.174E-01	3.698E-01	38.....	3.636E-02	1.802E-01	2.345E-01
-11.....	5.437E-01	4.017E-01	4.681E-01	39.....	3.565E-02	1.721E-01	2.237E-01
-10.....	6.712E-01	4.960E-01	5.779E-01	40.....	3.506E-02	1.649E-01	2.137E-01
-9.....	7.486E-01	5.889E-01	6.500E-01	41.....	3.456E-02	1.583E-01	2.046E-01
-8.....	8.151E-01	6.726E-01	7.148E-01	42.....	3.410E-02	1.524E-01	1.962E-01
-7.....	8.711E-01	7.469E-01	7.725E-01	43.....	3.365E-02	1.471E-01	1.884E-01
-6.....	9.168E-01	8.115E-01	8.236E-01	44.....	3.318E-02	1.423E-01	1.813E-01
-5.....	9.524E-01	8.660E-01	8.681E-01	45.....	3.266E-02	1.378E-01	1.747E-01
-4.....	9.781E-01	9.103E-01	9.062E-01	46.....	3.205E-02	1.337E-01	1.687E-01
-3.....	9.940E-01	9.449E-01	9.382E-01	47.....	3.139E-02	1.299E-01	1.630E-01
-2.....	1.000E+00	9.706E-01	9.639E-01	48.....	3.072E-02	1.263E-01	1.578E-01
-1.....	9.960E-01	9.880E-01	9.834E-01	49.....	3.005E-02	1.229E-01	1.529E-01
0.....	9.817E-01	9.976E-01	9.957E-01	50.....	2.945E-02	1.195E-01	1.483E-01
1.....	9.569E-01	1.000E+00	1.000E+00	51.....	2.893E-02	1.161E-01	1.440E-01
2.....	9.213E-01	9.958E-01	9.952E-01	52.....	2.853E-02	1.128E-01	1.398E-01
3.....	8.742E-01	9.856E-01	9.803E-01	53.....	2.830E-02	1.096E-01	1.359E-01
4.....	8.172E-01	9.702E-01	9.545E-01	54.....	2.827E-02	1.064E-01	1.320E-01
5.....	7.575E-01	9.502E-01	9.196E-01	55.....	2.849E-02	1.033E-01	1.282E-01
6.....	6.974E-01	9.263E-01	8.778E-01	56.....	2.793E-02	1.003E-01	1.244E-01
7.....	6.375E-01	8.991E-01	8.313E-01	57.....	2.738E-02	9.743E-02	1.207E-01
8.....	5.783E-01	8.691E-01	7.821E-01	58.....	2.684E-02	9.467E-02	1.170E-01
9.....	5.205E-01	8.369E-01	7.324E-01	59.....	2.630E-02	9.207E-02	1.133E-01
10.....	4.646E-01	8.031E-01	6.842E-01	60.....	2.578E-02	8.964E-02	1.097E-01
11.....	4.113E-01	7.683E-01	6.396E-01	61.....	2.527E-02	8.741E-02	1.061E-01
12.....	3.610E-01	7.330E-01	6.007E-01	62.....	2.477E-02	8.538E-02	1.026E-01
13.....	3.145E-01	6.977E-01	5.691E-01	63.....	2.428E-02	8.359E-02	9.910E-02
14.....	2.725E-01	6.629E-01	5.444E-01	64.....	2.380E-02	8.207E-02	9.568E-02
15.....	2.356E-01	6.293E-01	5.254E-01	65.....	2.333E-02	8.083E-02	9.232E-02
16.....	2.044E-01	5.972E-01	5.113E-01	66.....	2.287E-02	7.927E-02	8.902E-02
17.....	1.783E-01	5.667E-01	5.011E-01	67.....	2.242E-02	7.774E-02	8.579E-02
18.....	1.567E-01	5.376E-01	4.938E-01	68.....	2.197E-02	7.624E-02	8.264E-02
19.....	1.388E-01	5.099E-01	4.887E-01	69.....	2.154E-02	7.476E-02	7.958E-02
20.....	1.239E-01	4.835E-01	4.848E-01	70.....	2.111E-02	7.332E-02	7.660E-02
21.....	1.115E-01	4.583E-01	4.814E-01	71.....	2.070E-02	7.191E-02	7.373E-02
22.....	1.008E-01	4.342E-01	4.776E-01	72.....	2.029E-02	7.052E-02	7.096E-02
23.....	9.144E-02	4.113E-01	4.725E-01	73.....	1.989E-02	6.916E-02	6.832E-02
24.....	8.314E-02	3.894E-01	4.653E-01	74.....	1.949E-02	6.782E-02	6.581E-02
25.....	7.583E-02	3.685E-01	4.552E-01	75.....	1.911E-02	6.651E-02	6.344E-02
26.....	6.941E-02	3.486E-01	4.414E-01	76.....	1.873E-02	6.523E-02	6.199E-02
27.....	6.380E-02	3.296E-01	4.247E-01	77.....	1.836E-02	6.397E-02	6.057E-02
28.....	5.891E-02	3.115E-01	4.058E-01	78.....	1.799E-02	6.274E-02	5.918E-02
29.....	5.467E-02	2.943E-01	3.855E-01	79.....	1.764E-02	6.153E-02	5.783E-02
30.....	5.102E-02	2.781E-01	3.645E-01	80.....	1.729E-02	6.034E-02	5.650E-02

^a Day is relative to the epoch of the maximum of the *B*-band light curve. The *B*-band template may be found in Goldhaber et al. 2001.

^b Relative fluxes.

we perform the two steps separately so that all photometry may be combined to provide a light curve effectively observed through a standard (e.g., *R*-band) filter, which may then be fitted with a single series of *K*-corrections. The data tabulated in the Appendix have all been color-corrected to the standard Bessell filters.

Color and *K*-corrections were performed following the procedure of Nugent, Kim, & Perlmutter (2002). In order to perform these corrections, a template SN Ia spectrum for

each epoch of the light curve, as described in that paper, is necessary. The spectral template used in this present work began with the template of that paper. To it was applied a smooth multiplicative function at each day such that integration of the spectrum through the standard filters would produce the proper intrinsic colors for an SN Ia (including a mild dependence of those intrinsic colors on stretch).

The proper intrinsic colors for the SN spectral template were determined in the *BVRI* spectral range by smooth fits

TABLE 3
SUPERNOVA LIGHT-CURVE FITS: *HST* SUPERNOVAE FROM THIS PAPER

SN	z	m_X^a	m_B^b	$m_B^{\text{eff}c}$	$m_B^{\text{eff}} + \text{Extinction Correction}^d$	Stretch	$R - I^e$	$E(B - V)_{\text{Galactic}}^f$	$E(B - V)_{\text{host}}^g$	Excluded from Subsets ^h
1997ek	0.863	23.32	24.51 \pm 0.03	24.59 \pm 0.19	24.95 \pm 0.44	1.056 \pm 0.058	0.838 \pm 0.054	0.042	-0.091 \pm 0.075	
1997eq	0.538	22.63	23.21 \pm 0.02	23.15 \pm 0.18	23.02 \pm 0.17	0.960 \pm 0.027	0.202 \pm 0.030	0.044	0.035 \pm 0.034	
1997ez	0.778	23.17	24.29 \pm 0.03	24.41 \pm 0.18	24.00 \pm 0.42	1.078 \pm 0.030	0.701 \pm 0.048	0.026	0.095 \pm 0.068	
1998as	0.355	22.18	22.72 \pm 0.03	22.66 \pm 0.17	22.02 \pm 0.15	0.956 \pm 0.012	0.226 \pm 0.027	0.037	0.158 \pm 0.030	2, 3
1998aw	0.440	22.56	23.22 \pm 0.02	23.26 \pm 0.17	...	1.026 \pm 0.019	0.300 \pm 0.024	0.026	0.259 \pm 0.026	1-3
1998ax	0.497	22.63	23.25 \pm 0.05	23.47 \pm 0.17	22.96 \pm 0.20	1.150 \pm 0.032	0.212 \pm 0.041	0.035	0.113 \pm 0.044	2, 3
1998ay	0.638	23.26	23.86 \pm 0.08	23.92 \pm 0.19	23.85 \pm 0.33	1.040 \pm 0.041	0.339 \pm 0.067	0.035	0.015 \pm 0.084	3
1998ba	0.430	22.34	22.97 \pm 0.05	22.90 \pm 0.18	22.75 \pm 0.18	0.954 \pm 0.020	0.094 \pm 0.036	0.024	0.040 \pm 0.038	
1998be	0.644	23.33	23.91 \pm 0.04	23.64 \pm 0.18	23.26 \pm 0.27	0.816 \pm 0.028	0.436 \pm 0.051	0.029	0.106 \pm 0.065	3
1998bi	0.740	22.86	23.92 \pm 0.02	23.85 \pm 0.17	23.75 \pm 0.37	0.950 \pm 0.027	0.552 \pm 0.037	0.026	0.026 \pm 0.050	
2000fr	0.543	22.44	23.07 \pm 0.02	23.16 \pm 0.17	23.27 \pm 0.14	1.064 \pm 0.011	0.135 \pm 0.022	0.030	-0.031 \pm 0.025	

^a Magnitude in the observed filter at the peak of the rest-frame B -band light curve; $X = R$ for $z < 0.7$, $X = I$ for $z > 0.7$.

^b This value has been K -corrected and corrected for Galactic extinction: $m_B \equiv m_X - K_{BX} - A_X$, where K_{BX} is the cross filter K -correction and A_X is the Galactic extinction correction. These were the values used in the cosmological fits. The quoted error bar is the uncertainty on the peak magnitude from the light-curve fit.

^c This value includes the stretch correction: $m_B^{\text{eff}} \equiv m_B + \alpha(s - 1)$; α is the best-fit value of the stretch-luminosity slope from the fit to the primary low-extinction subset (fit 3 in § 4). The quoted error bar includes all uncertainties for non-extinction-corrected fits described in § 2.4. Note that these values are only provided for convenience; they were not used directly in any cosmological fits, since α is also a fit parameter.

^d Similar to the previous column, only with the host galaxy extinction correction applied. The stretch-luminosity slope used for this value is that from the fit to the primary subset (fit 6 in § 4). The quoted error bar includes all uncertainties for extinction-corrected fits described in § 2.4. Ellipses indicate an SN that did not appear in the primary subset (see § 2.5).

^e This is the observed $R - I$ color at the epoch of the rest-frame B -band light-curve peak.

^f Schlegel et al. 1998; this extinction is already included in the quoted values of m_B .

^g Measurement uncertainty only; no intrinsic color dispersion included.

^h These SNe are excluded from the indicated subsets; see § 2.5.

TABLE 4
SUPERNOVA LIGHT-CURVE FITS: NEW FITS TO P99 SNe

SN	z	m_X^a	m_B^b	$m_B^{\text{eff}c}$	$m_B^{\text{eff}} + \text{Extinction}$ Correction ^d	Stretch	$R - I^e$	$E(B - V)$ Galactic ^f	$E(B - V)_{\text{host}}^g$	Excluded from Subsets ^h
1995ar	0.465	22.80	23.48 ± 0.08	23.35 ± 0.22	21.54 ± 0.97	0.909 ± 0.104	0.509 ± 0.222	0.022	0.448 ± 0.242	
1995as	0.498	23.03	23.69 ± 0.07	23.74 ± 0.23	23.52 ± 0.87	1.035 ± 0.090	0.155 ± 0.197	0.021	0.051 ± 0.212	3
1995aw	0.400	21.78	22.28 ± 0.03	22.57 ± 0.18	23.17 ± 0.45	1.194 ± 0.037	-0.127 ± 0.103	0.040	-0.160 ± 0.107	
1995ax	0.615	22.56	23.21 ± 0.06	23.38 ± 0.22	23.98 ± 1.02	1.112 ± 0.073	0.152 ± 0.204	0.033	-0.153 ± 0.249	
1995ay	0.480	22.64	23.07 ± 0.04	22.90 ± 0.19	22.74 ± 0.70	0.880 ± 0.064	0.209 ± 0.158	0.114	0.047 ± 0.170	
1995az	0.450	22.46	22.70 ± 0.07	22.66 ± 0.20	23.04 ± 0.58	0.973 ± 0.064	0.087 ± 0.135	0.181	-0.089 ± 0.144	
1995ba	0.388	22.07	22.64 ± 0.06	22.60 ± 0.18	22.74 ± 0.45	0.971 ± 0.047	0.006 ± 0.105	0.018	-0.033 ± 0.110	
1996cf	0.570	22.71	23.31 ± 0.03	23.30 ± 0.18	23.53 ± 0.45	0.996 ± 0.045	0.162 ± 0.091	0.040	-0.054 ± 0.107	3
1996cg	0.490	22.46	23.09 ± 0.03	23.11 ± 0.18	22.26 ± 0.45	1.011 ± 0.040	0.300 ± 0.099	0.035	0.205 ± 0.107	3
1996ci	0.495	22.19	22.83 ± 0.02	22.78 ± 0.18	22.92 ± 0.32	0.964 ± 0.040	0.083 ± 0.070	0.028	-0.033 ± 0.075	
1996cl	0.828	23.37	24.53 ± 0.17	24.49 ± 0.46	25.92 ± 0.97	0.974 ± 0.239	0.549 ± 0.184	0.035	-0.344 ± 0.251	
1996cm	0.450	22.67	23.26 ± 0.07	23.11 ± 0.18	22.63 ± 0.77	0.899 ± 0.061	0.214 ± 0.174	0.049	0.124 ± 0.185	3
1996cn	0.430	22.58	23.25 ± 0.03	23.09 ± 0.19	...	0.890 ± 0.066	0.379 ± 0.090	0.025	0.332 ± 0.097	1-3
1997F	0.580	22.93	23.51 ± 0.06	23.57 ± 0.20	23.30 ± 0.95	1.041 ± 0.066	0.275 ± 0.197	0.040	0.063 ± 0.232	
1997H	0.526	22.70	23.26 ± 0.04	23.09 ± 0.19	22.51 ± 0.80	0.882 ± 0.043	0.303 ± 0.174	0.051	0.150 ± 0.194	
1997I	0.172	20.18	20.34 ± 0.01	20.29 ± 0.17	20.19 ± 0.28	0.967 ± 0.009	0.065 ± 0.047	0.051	0.026 ± 0.064	
1997N	0.180	20.39	20.38 ± 0.02	20.48 ± 0.17	21.28 ± 0.52	1.067 ± 0.015	-0.141 ± 0.093	0.031	-0.200 ± 0.123	
1997O	0.374	22.99	23.53 ± 0.06	23.60 ± 0.18	...	1.048 ± 0.054	0.087 ± 0.152	0.029	0.049 ± 0.162	1-3
1997P	0.472	22.53	23.16 ± 0.04	22.99 ± 0.18	23.24 ± 0.91	0.888 ± 0.039	0.058 ± 0.207	0.033	-0.052 ± 0.219	
1997Q	0.430	22.01	22.61 ± 0.02	22.52 ± 0.17	22.55 ± 0.62	0.935 ± 0.024	0.061 ± 0.140	0.030	-0.002 ± 0.148	
1997R	0.657	23.29	23.89 ± 0.05	23.80 ± 0.19	23.68 ± 0.90	0.940 ± 0.059	0.393 ± 0.175	0.030	0.032 ± 0.222	
1997ac	0.320	21.42	21.87 ± 0.02	21.96 ± 0.17	21.95 ± 0.33	1.061 ± 0.015	0.063 ± 0.065	0.027	0.001 ± 0.072	
1997af	0.579	22.94	23.60 ± 0.07	23.38 ± 0.18	24.31 ± 1.09	0.850 ± 0.045	0.045 ± 0.226	0.028	-0.215 ± 0.265	
1997ai	0.450	22.34	22.94 ± 0.05	22.63 ± 0.22	22.58 ± 0.59	0.788 ± 0.084	0.143 ± 0.133	0.045	0.026 ± 0.142	
1997aj	0.581	22.58	23.24 ± 0.07	23.16 ± 0.18	24.05 ± 0.79	0.947 ± 0.045	0.045 ± 0.164	0.033	-0.213 ± 0.193	
1997am	0.416	22.01	22.58 ± 0.08	22.63 ± 0.18	22.65 ± 0.46	1.032 ± 0.060	0.037 ± 0.113	0.036	-0.008 ± 0.119	
1997ap	0.830	23.16	24.35 ± 0.07	24.38 ± 0.18	23.74 ± 0.50	1.023 ± 0.045	0.903 ± 0.082	0.026	0.155 ± 0.118	

^a $X = R$ for $z < 0.7$, $X = I$ for $z > 0.7$.

^b This value has been K -corrected and corrected for Galactic extinction: $m_B \equiv m_X - K_{BX} - A_X$, where K_{BX} is the cross filter K -correction and A_X is the Galactic extinction correction. These were the values used in the cosmological fits. The quoted error bar is the uncertainty on the peak magnitude from the light-curve fit.

^c This value includes the stretch correction: $m_B^{\text{eff}} \equiv m_B + \alpha(s - 1)$; α is the best-fit value of the stretch-luminosity slope from the fit to the primary low-extinction subset (fit 3 in § 4). The quoted error bar includes all uncertainties for non-extinction-corrected fits described in § 2.4. Note that these values are only provided for convenience; they were not used directly in any cosmological fits, since α is also a fit parameter.

^d Similar to the previous column, only with the host galaxy extinction correction applied. The stretch-luminosity slope used for this value is that from the fit to the primary subset (fit 6 in § 4). The quoted error bar includes all uncertainties for extinction-corrected fits described in § 2.4. Ellipses indicate an SN that did not appear in the primary subset (see § 2.5).

^e This is the observed $R - I$ color at the epoch of the rest-frame B -band light-curve peak.

^f Schlegel et al. 1998; this extinction is already included in the quoted values of m_B .

^g Measurement uncertainty only; no intrinsic color dispersion included.

^h These SNe are excluded from the indicated subsets; see § 2.5.

TABLE 5
SUPERNOVA LIGHT-CURVE FITS: LOW- z SNe FROM H96 AND R99

SN ^a	z	m_B^{measb}	m_B^c	m_B^{effd}	$m_B^{\text{eff}} + \text{Extinction}$ Correction ^e	Stretch	$R - f^f$	$E(B - V)$ Galactic ^g	$E(B - V)_{\text{host}}^h$	Excluded from Subsets ⁱ
1990O	0.030	16.58	16.18 \pm 0.03	16.33 \pm 0.20	16.30 \pm 0.17	1.106 \pm 0.026	0.043 \pm 0.025	0.098	0.001 \pm 0.026	
1990af	0.050	17.92	17.76 \pm 0.01	17.39 \pm 0.18	17.42 \pm 0.13	0.749 \pm 0.010	0.077 \pm 0.011	0.035	0.011 \pm 0.011	
1992P	0.026	16.12	16.05 \pm 0.02	16.14 \pm 0.19	16.16 \pm 0.16	1.061 \pm 0.027	-0.045 \pm 0.018	0.020	-0.008 \pm 0.019	
1992ae	0.075	18.59	18.42 \pm 0.04	18.35 \pm 0.18	18.35 \pm 0.15	0.957 \pm 0.018	0.098 \pm 0.028	0.036	0.003 \pm 0.031	
1992ag	0.026	16.67	16.26 \pm 0.02	16.34 \pm 0.20	15.55 \pm 0.16	1.053 \pm 0.015	0.220 \pm 0.020	0.097	0.189 \pm 0.021	2, 3
1992al	0.014	14.61	14.48 \pm 0.01	14.42 \pm 0.23	14.53 \pm 0.20	0.959 \pm 0.011	-0.054 \pm 0.012	0.034	-0.025 \pm 0.013	
1992aq	0.101	19.38	19.30 \pm 0.02	19.12 \pm 0.17	19.24 \pm 0.15	0.878 \pm 0.017	0.142 \pm 0.023	0.012	-0.019 \pm 0.026	
1992bc	0.020	15.18	15.10 \pm 0.01	15.18 \pm 0.20	15.36 \pm 0.16	1.053 \pm 0.006	-0.087 \pm 0.009	0.022	-0.046 \pm 0.009	
1992bg	0.036	17.41	16.66 \pm 0.04	16.66 \pm 0.20	16.68 \pm 0.16	1.003 \pm 0.014	0.128 \pm 0.025	0.181	-0.006 \pm 0.026	
1992bh	0.045	17.71	17.60 \pm 0.02	17.64 \pm 0.18	17.22 \pm 0.14	1.027 \pm 0.016	0.101 \pm 0.018	0.022	0.100 \pm 0.019	
1992bl	0.043	17.37	17.31 \pm 0.03	17.03 \pm 0.18	17.10 \pm 0.14	0.812 \pm 0.012	0.017 \pm 0.023	0.012	-0.002 \pm 0.024	
1992bo	0.018	15.89	15.78 \pm 0.01	15.42 \pm 0.21	15.31 \pm 0.17	0.756 \pm 0.005	0.048 \pm 0.012	0.027	0.043 \pm 0.012	
1992bp	0.079	18.59	18.29 \pm 0.01	18.16 \pm 0.18	18.41 \pm 0.13	0.906 \pm 0.014	0.088 \pm 0.015	0.068	-0.056 \pm 0.017	1-3
1992br	0.088	19.52	19.37 \pm 0.08	18.93 \pm 0.20	...	0.700 \pm 0.021	0.186 \pm 0.047	0.027	0.030 \pm 0.052	
1992bs	0.063	18.26	18.20 \pm 0.04	18.26 \pm 0.18	18.37 \pm 0.14	1.038 \pm 0.016	0.011 \pm 0.022	0.013	-0.031 \pm 0.024	
1993B	0.071	18.74	18.37 \pm 0.04	18.40 \pm 0.18	18.10 \pm 0.15	1.021 \pm 0.019	0.181 \pm 0.027	0.080	0.071 \pm 0.029	
1993O	0.052	17.87	17.64 \pm 0.01	17.53 \pm 0.18	17.61 \pm 0.13	0.926 \pm 0.007	0.042 \pm 0.012	0.053	-0.014 \pm 0.012	2, 3
1993ag	0.050	18.32	17.83 \pm 0.02	17.73 \pm 0.18	17.26 \pm 0.15	0.936 \pm 0.015	0.217 \pm 0.020	0.111	0.120 \pm 0.021	
1994M	0.024	16.34	16.24 \pm 0.03	16.07 \pm 0.20	15.84 \pm 0.16	0.882 \pm 0.015	0.043 \pm 0.022	0.023	0.063 \pm 0.022	
1994S	0.016	14.85	14.78 \pm 0.02	14.83 \pm 0.22	14.86 \pm 0.19	1.033 \pm 0.026	-0.061 \pm 0.019	0.018	-0.010 \pm 0.019	
1995ac	0.049	17.23	17.05 \pm 0.01	17.17 \pm 0.18	17.17 \pm 0.13	1.083 \pm 0.012	0.026 \pm 0.011	0.042	-0.005 \pm 0.011	1-3
1995bd	0.016	17.34	15.32 \pm 0.01	15.37 \pm 0.30	...	1.039 \pm 0.008	0.735 \pm 0.008	0.490	0.348 \pm 0.009	
1996C	0.030	16.62	16.57 \pm 0.04	16.74 \pm 0.19	16.50 \pm 0.16	1.120 \pm 0.020	0.012 \pm 0.026	0.014	0.051 \pm 0.027	
1996ab	0.125	19.72	19.57 \pm 0.04	19.47 \pm 0.19	19.82 \pm 0.16	0.934 \pm 0.032	0.174 \pm 0.025	0.032	-0.082 \pm 0.029	
1996bl	0.035	17.08	16.66 \pm 0.01	16.71 \pm 0.19	16.55 \pm 0.14	1.031 \pm 0.015	0.093 \pm 0.012	0.099	0.036 \pm 0.012	1-3
1996bo	0.016	16.18	15.85 \pm 0.01	15.65 \pm 0.22	...	0.862 \pm 0.006	0.406 \pm 0.008	0.077	0.383 \pm 0.008	

^a SNe through 1993ag are from H96; later ones are from R99.

^b This is the measured peak magnitude of the B -band light curve.

^c This includes the Galactic extinction correction and a K -correction: $M - B \equiv m_B^{\text{meas}} - K_B - A_B$, where K_B is the K -correction and A_B is the Galactic extinction correction. The quoted error bar is the uncertainty on the peak magnitude from the light-curve fit.

^d This value includes the stretch correction: $m_B^{\text{eff}} \equiv m_B^{\text{meas}} - K_B - A_B + \alpha(s - 1)$; α is the best-fit value of the stretch-luminosity slope from the fit to the primary low-extinction subset (fit 3 in § 4). The quoted error bar includes all uncertainties for non-extinction-corrected fits described in § 2.4. Note that these values are only provided for convenience; they were not used directly in any cosmological fits, since the α is also a fit parameter.

^e Similar to the previous column, only with the host galaxy extinction correction applied. The stretch-luminosity slope used for this value is that from the fit to the primary subset (fit 6 in § 4). The quoted error bar includes all uncertainties for extinction-corrected fits described in § 2.4. Ellipses indicate an SN that did not appear in the primary subset (see § 2.5).

^f This value has been K -corrected and corrected for Galactic extinction.

^g This is the measured $B - V$ color at the epoch of rest-frame B -band light-curve maximum.

^h Schlegel et al. 1998; this extinction is already included in the quoted values of m_B in the fourth column.

ⁱ These SNe are excluded from the indicated subsets; see § 2.5.

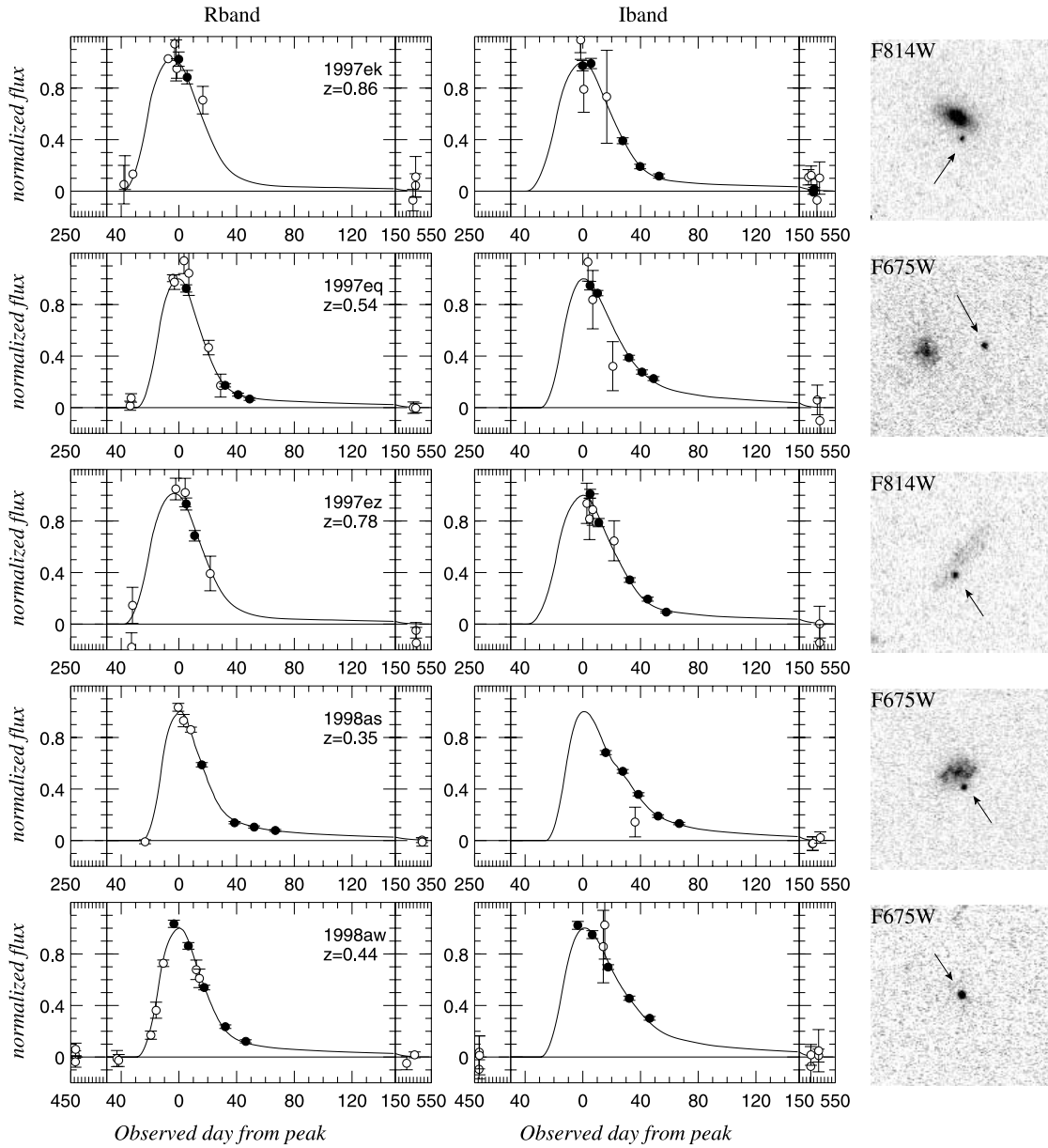


FIG. 1.—Light curves and images from the PC CCD on WFPC2 for the *HST* SNe reported in this paper. The left-hand column shows the *R*-band light curves (including F675W *HST* data), and the middle column shows *I*-band light curves (including F814W *HST* data). Open circles represent ground-based data points, and filled circles represent WFPC2 data points. Note that there are correlated errors between all of the ground-based points for each SN in these figures, as a single ground-based zero point was used to scale each of them together with the *HST* photometry. The right-hand column shows $6'' \times 6''$ images, summed from all *HST* images of the SN in the indicated filter.

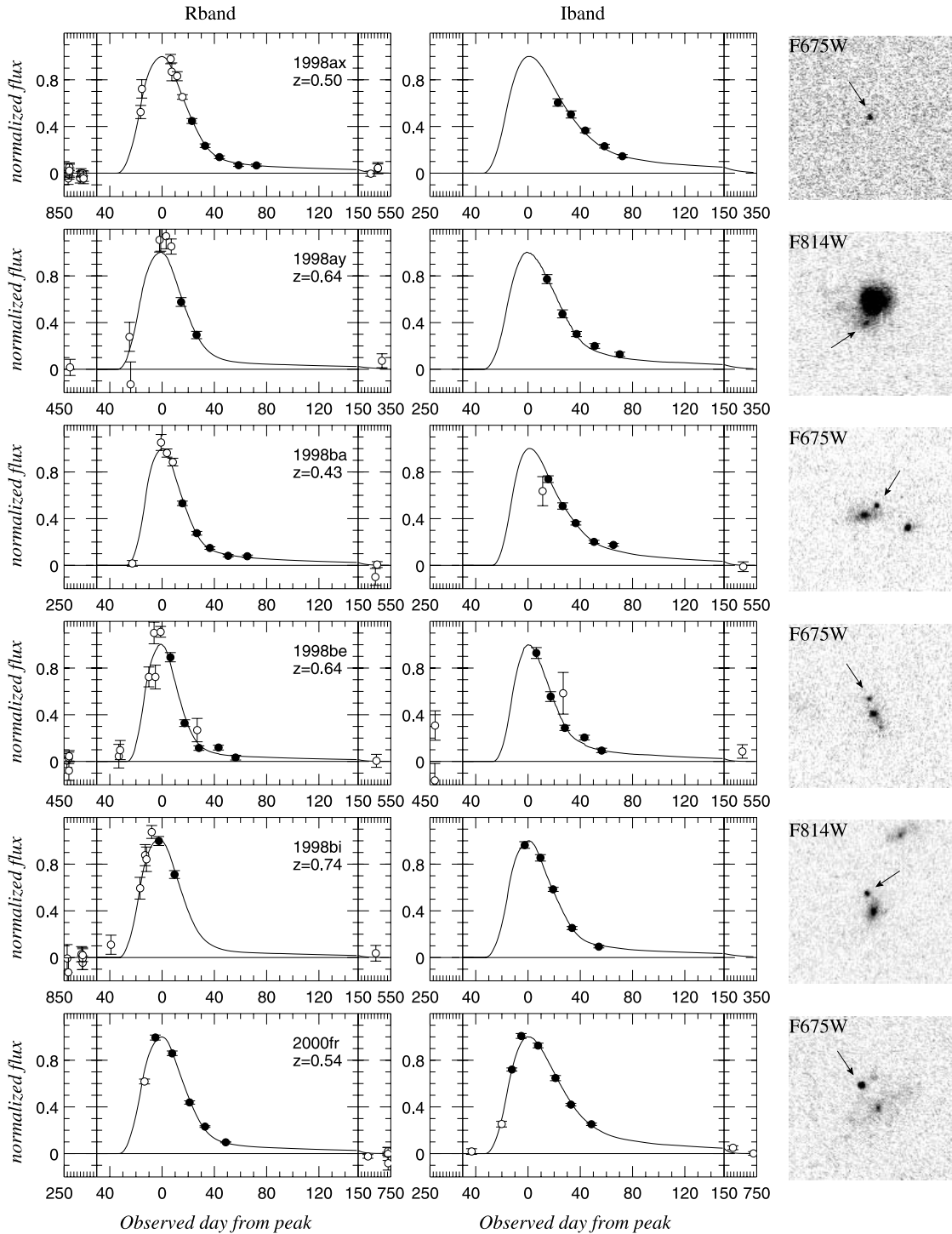
to the low-redshift SN data of H96 and R99. For each color ($B-V$, $V-R$, and $R-I$), every data point from those papers was K -corrected and corrected for Galactic extinction. These data were plotted together, and then a smooth curve was fitted to the plot of color versus date relative to maximum. This curve is given by two parameters, each of which is a function of time and is described by a spline under tension: an “intercept” $b(t)$ and a “slope” $m(t)$. At any given date the intrinsic color is

$$\text{color}(t') = b(t') + m(t')(1/s^3 - 1), \quad (2)$$

where $t' = t/[s(1+z)]$, z is the redshift of the SN, and s is the timescale stretch of the SN from a simultaneous fit to

the B and V light curves (matching the procedure used for most of the high-redshift SNe). This arbitrary functional form was chosen to match the stretch versus color distribution.

As the goal was to determine intrinsic colors without making any assumptions about reddening, no host galaxy extinction corrections were applied to the literature data at this stage of the analysis. Instead, host galaxy extinction was handled by performing a robust blue-side ridgeline fit to the SN color curves, so as to extract the unreddened intrinsic color. Individual color points that were outliers were prevented from having too much weight in the fit with a small added dispersion on each point. The blue ridgeline was selected by allowing any point more than 1σ to the red

FIG. 1.—*Continued*

side of the fit model only to contribute to the χ^2 as if it were 1σ away. Additionally, those SNe that were most reddened were omitted. The resulting fit procedure provided $B-V$, $V-R$, and $R-I$ as a function of epoch and stretch; those colors were used to correct the template spectrum as described above.

Some of our data extend into the rest-frame U -band range of the spectrum. This is obvious for SNe at $z > 0.7$ where a U -band template is fitted to the R -band data. However, even for SNe at $z \gtrsim 0.55$, the deredshifted R -band filter

begins to overlap the U -band range of the rest-frame spectrum. Thus, it is also important to know the intrinsic $U-B$ color so as to generate a proper spectral template. We used data from the literature, as given in Table 6. Here there is an insufficient number of SN light curves to reasonably use the sort of ridgeline analysis used above to eliminate the effects of host galaxy extinction in determining the intrinsic $BVRI$ colors. Instead, for $U-B$, we perform extinction corrections using the $E(B-V)$ values from Phillips et al. (1999). Based on Table 6, we adopt a $U-B$ color of -0.4 at the epoch of

TABLE 6
 $U-B$ SN Ia COLORS AT EPOCH OF B -BAND MAXIMUM

SN	Raw $U-B^a$	Corrected $U-B^b$	References
1980N	-0.21	-0.29	1
1989B	0.08	-0.33	2
1990N	-0.35	-0.45	3
1994D	-0.50	-0.52	4
1998bu	-0.23	-0.51	5

^a This is the measured $U-B$ value from the cited paper.

^b This $U-B$ value is K -corrected and corrected for host galaxy and Galactic extinction.

REFERENCES.—(1) Hamuy et al. 1991. (2) Wells et al. 1994. (3) Lira et al. 1998. (4) Wu, Yan, & Zou 1995. (5) Suntzeff et al. 1999.

rest- B maximum. This value is also consistent with the data shown in Jha (2002) for SNe with timescale stretch of $s \sim 1$, although the data are not determinative. In contrast to the other colors, $U-B$ was not considered to be a function of stretch. Even though Jha (2002) does show $U-B$ depending on light-curve stretch, the SNe in this work that would be most affected [those at $z > 0.7$ where $E(B-V)$ is estimated from the rest-frame $U-B$ color] cover a small range in stretch; current low-redshift $U-B$ data do not show a significant slope within that range. See § 5.4 for the effect of systematic error in the assumed intrinsic $U-B$ colors.

Any intrinsic uncertainty in $B-V$ is already subsumed within the assumed intrinsic dispersion of extinction-corrected peak magnitudes (see § 2.4); however, we might expect a larger dispersion in intrinsic $U-B$ due to, e.g., metallicity effects (Hoefflich, Wheeler, & Thielemann 1998; Lentz et al. 2000). The low-redshift U -band photometry may also have unmodeled scatter, e.g., related to the lack of extensive UV SN spectrophotometry for K -corrections. The effect on extinction-corrected magnitudes will be further increased by the greater effect of dust extinction on the bluer U -band light. The scatter of our extinction-corrected magnitudes about the best-fit cosmology suggests an intrinsic uncertainty in $U-B$ of 0.04 mag. This is also consistent with the $U-B$ data of Jha (2002) over the range of timescale stretch of our $z > 0.7$ SNe Ia, after two extreme color outliers from Jha (2002) are removed; there is no evidence of such extreme color objects in our data set. Note that this intrinsic $U-B$ dispersion is in addition to the intrinsic magnitude dispersion assumed after extinction correction.

The template spectrum that has been constructed may be used to perform color and K -corrections on both the low- and high-redshift SNe to be used for cosmology. However, it must be further modified to account for the reddening effects of dust extinction in the SN host galaxy and extinction of the redshifted spectrum due to Galactic dust. To calculate the reddening effects of both Galactic and host galaxy extinction, we used the interstellar extinction law of O'Donnell (1994) with the standard value of the parameter $R_V = 3.1$. Color excess $[E(B-V)]$ values due to Galactic extinction were obtained from Schlegel, Finkbeiner, & Davis (1998).

The $E(B-V)$ values quoted in Tables 3, 4, and 5 are the values necessary to reproduce the observed $R-I$ color at the epoch of the maximum of the rest-frame B light curve. This reproduction was performed by modifying the spectral template exactly as described above, given the intrinsic color of

the SN from the fit stretch, the Galactic extinction, and the host galaxy $E(B-V)$ parameter. The modified spectrum was integrated through the Bessell R - and I -band filters, and $E(B-V)$ was varied until the $R-I$ value matched the peak color from the light-curve fit.

For each SN, this finally modified spectral template was integrated through the Bessell and WFPC2 filter transmission functions to provide color and K -corrections. The exact spectral template needed for a given data point on a given SN is dependent on parameters of the fit: the stretch, the time of each point relative to the epoch of rest- B maximum, and the host galaxy $E(B-V)$ (measured as described above). Thus, color and K -corrections were performed iteratively with light-curve fitting in order to generate the final corrections used in the fits described in § 2.2. An initial date of maximum, stretch, and host galaxy extinction was assumed in order to generate K -corrections for the first iteration of the fit. The parameters resulting from that fit were used to generate new color and K -corrections, and the whole procedure was repeated until the results of the fit converged. Generally, the fit converged within two to three iterations.

2.4. Cosmological Fit Methodology

Cosmological fits to the luminosity distance modulus equation from the Friedmann-Robertson-Walker metric followed the procedure of P99. The set of SN redshifts (z) and K -corrected peak B magnitudes (m_B) were fitted to the equation

$$m_B = \mathcal{M} + 5 \log \mathcal{D}_\varphi(z; \Omega_M, \Omega_\Lambda) - \alpha(s - 1), \quad (3)$$

where s is the stretch value for the SN, $\mathcal{D}_\varphi \equiv H_0 d_L$ is the “Hubble constant-free” luminosity distance (Perlmutter et al. 1997), and $\mathcal{M} \equiv M_B - 5 \log H_0 + 25$ is the “Hubble constant-free” B -band peak absolute magnitude of an $s = 1$ SN Ia with true absolute peak magnitude M_B . With this procedure, neither H_0 nor M_B need be known independently. The peak magnitude of an SN Ia is mildly dependent on the light-curve decay timescale, such that SNe with a slow decay (high stretch) tend to be overluminous, while SNe with a fast decay (low stretch) tend to be underluminous (Phillips 1993); α is a slope that parameterizes this relationship.

There are four parameters in the fit: the mass density Ω_M and cosmological constant Ω_Λ , as well as the two nuisance parameters, \mathcal{M} and α . The four-dimensional ($\Omega_M, \Omega_\Lambda, \mathcal{M}, \alpha$) space is divided into a grid, and at each grid point a χ^2 value is calculated by fitting the luminosity distance equation to the peak B -band magnitudes and redshifts of the SNe. The range of parameter space explored included $\Omega_M = [0, 3]$, $\Omega_\Lambda = [-1, 3]$ (for fits where host galaxy extinction corrections are not directly applied) or $\Omega_M = [0, 4]$, $\Omega_\Lambda = [-1, 4]$ (for fits with host galaxy extinction corrections). The two nuisance parameters are fitted in the ranges $\alpha = [-1, 4]$ and $\mathcal{M} = [-3.9, 3.2]$. No further constraints are placed on the parameters. (These ranges for the four fit parameters contain greater than 99.99% of the probability.) At each point on the four-dimensional grid, a χ^2 is calculated, and a probability is determined from $P \propto e^{-\chi^2/2}$. The probability of the whole four-dimensional grid is normalized and then integrated over the two dimensions corresponding to the “nuisance” parameters.

For each fit, all peak m_B values were corrected for Galactic extinction using $E(B-V)$ values from Schlegel

et al. (1998), using the extinction law of O'Donnell (1994) integrated through the *observed* filter.³¹ For our primary fits, the total effective statistical uncertainty on each value of m_B included the following contributions:

1. The uncertainty on m_B from the light-curve fits.
2. The uncertainty on s , multiplied by α .
3. The covariance between m_B and s .
4. A contribution from the uncertainty in the redshift due to peculiar velocity (assumed to have a dispersion of 300 km s^{-1} along the line of sight).
5. 10% of the Galactic extinction correction.
6. 0.17 mag of intrinsic dispersion (H96).

Fits where host galaxy extinction corrections are explicitly applied use the first five items above plus the following:

1. The uncertainty on $E(B-V)$ multiplied by R_B .
2. The covariance between $E(B-V)$ and m_B .
3. 0.11 mag of intrinsic dispersion (Phillips et al. 1999).
4. An additional 0.04 mag of intrinsic $U-B$ dispersion for $z > 0.7$.

Host galaxy extinction corrections used a value $R_B \equiv A_B/E(B-V) = 4.1$, which results from passing an SN Ia spectrum through the standard O'Donnell (1994) extinction law. Except where explicitly noted below, the $E(B-V)$ uncertainties are *not* reduced by any prior assumptions on the intrinsic color excess distribution. Although there is almost certainly some intrinsic dispersion either in R_B or in the true $B-V$ color of an SN Ia (Nobili et al. 2003), we do not explicitly include such a term. The effect of such a dispersion is included, in principle, in the 0.11 mag of intrinsic magnitude dispersion that Phillips et al. (1999) found after applying extinction corrections.

As discussed in § 2.3, the intrinsic $U-B$ dispersion is likely to be greater than the intrinsic $B-V$ dispersion. For those SNe most affected by this (i.e., those at $z > 0.7$), we included an additional uncertainty corresponding to 0.04 mag of intrinsic $U-B$ dispersion, converted into a magnitude error using the O'Donnell extinction law.

This set of statistical uncertainties is slightly different from that used in P99. For these fits, the test value of α was used to propagate the stretch errors into the corrected B -band magnitude errors; in contrast, P99 used a single value of α for purposes of error propagation.

2.5. Supernova Subsets

In P99, separate analyses were performed and compared for the SN sample before and after removing SNe with less secure identification as Type Ia. The results were shown to be consistent, providing a cross-check of the cosmological conclusions. For the analyses of this paper, adding and comparing 11 very well measured SNe Ia, we only consider from P99 the more securely spectrally identified SNe Ia with reasonable color measurements (i.e., $\sigma_{R-I} < 0.25$); those SNe are listed in Table 4. Following P99, we omit one SN that is an outlier in the stretch distribution, with $s < 0.7$ (SN 1992br), and one SN that is a greater than 6σ outlier from the best-fit cosmology (SN 1997O). We also omit those SNe that are most seriously reddened, with $E(B-V) > 0.25$ and

greater than 3σ above zero; host galaxy extinction corrections have been found in studies of low-redshift SNe to overcorrect these reddest objects (Phillips et al. 1999). This cut removes two SNe at low redshift (SN 1995bd and SN 1996bo), one from P99 (SN 1996cn), and one of the 11 *HST* SNe from this paper (SN 1998aw). The resulting “full primary subset” of SNe Ia is identified as subset 1 in the tables.

For the analyses of a “low-extinction primary subset,” subset 2, we further cull out four SNe with host galaxy $E(B-V) > 0.1$ and greater than 2σ above zero, including two of the *HST* SNe from this paper (SN 1992ag, SN 1993ag, SN 1998as, and SN 1998ax). The low-extinction primary subset includes eight of the 11 new *HST* SNe presented in this paper.

Subset 3, the “low-extinction strict Ia subset,” makes an even more stringent cut on spectral confirmation, including only those SNe whose confirmations as Type Ia SNe are unquestionable. This subset is used in § 5.2 to estimate any possible systematic bias resulting from type contamination. An additional six SNe, including two of the *HST* SNe from this paper, are omitted from subset 3 beyond those omitted from subset 2; these are SN 1995as, SN 1996cf, SN 1996cg, SN 1996cm, SN 1998ay, and SN 1998be.

3. COLORS AND EXTINCTION

In this section we discuss the limits on host galaxy extinction we can set based on the measured colors of our SNe. For the primary fit of our P99 analysis, extinction was estimated by comparing the mean host galaxy $E(B-V)$ values from the low- and high-redshift samples. Although the uncertainties on individual $E(B-V)$ values for high-redshift SNe were large, the uncertainty on the mean of the distribution was only 0.02 mag. P99 showed that there was no significant difference in the mean host galaxy reddening between the low- and high-redshift samples of SNe of the primary analysis (fit C). This tightly constrained the systematic uncertainty on the cosmological results due to differences in extinction. The models of Hatano, Branch, & Deaton (1998) suggest that most SNe Ia should be found with little or no host galaxy extinction. By making a cut to include only those objects that have small $E(B-V)$ values (and then verifying the consistency of low- and high-redshift mean reddening), we are creating a subsample likely to have quite low extinction. The strength of this method is that it does not depend on the exact shape of the intrinsic extinction distribution but only requires that most SNe show low extinction. Figure 2 (discussed below) demonstrates that most SNe indeed have low extinction, as expected from the Hatano et al. (1998) models. Monte Carlo simulations of our data using the Hatano et al. (1998) extinction distribution function and our low-extinction $E(B-V)$ cuts confirm the robustness of this approach and further demonstrate that similarly low extinction subsamples are obtained for both low- and high-redshift data sets despite the larger color uncertainties for some of the P99 SNe.

Riess et al. (1998) used the work of Hatano et al. (1998) differently, by applying a one-sided Bayesian prior to their measured $E(B-V)$ values and uncertainties. A prior formed from the Hatano et al. (1998) extinction distribution function would have zero probability for negative values of $E(B-V)$, a peak at $E(B-V) \sim 0$ with roughly 50% of the probability, and an exponential tail to higher extinctions. As discussed in P99 (see the “fit E” discussion, where P99

³¹ This supersedes P99, where an incorrect dependence on z of the effective R_R for Galactic extinction was applied. The corrected procedure decreases the flat-universe value of Ω_M by 0.03.

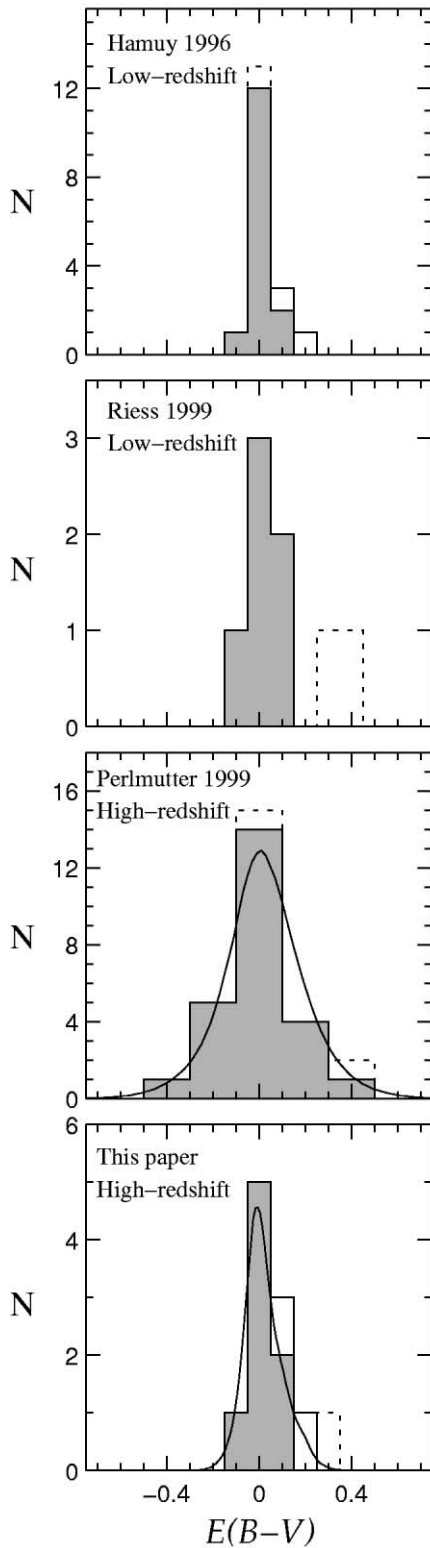


FIG. 2.—Histograms of $E(B-V)$ for the four samples of SNe used in this paper. The filled gray histogram represents just the low-extinction subset (subset 2). The open boxes on top of that represent SNe that are in the primary subset (subset 1) but excluded from the low-extinction subset. Finally, the dotted histogram represents those SNe that are in the full sample but omitted from the primary subset. The solid lines drawn over the bottom two panels are a simulation of the distribution expected if the low-extinction subset of the H96 sample represented the true distribution of SN colors, given the error bars of the low-extinction subset of each high-redshift sample.

apply the same method), when uncertainties on high- and low-redshift SN colors differ, use of an asymmetric prior may introduce bias into the cosmological results, depending on the details of the prior. While a prior with a tight enough peak at low-extinction values introduces little bias (especially when low- and high-redshift SNe have comparable uncertainties), it does reduce the apparent $E(B-V)$ error bars on all but the most reddened SNe. As we will show in Figure 9 (§ 4.1) the use of this prior almost completely eliminates the contribution of color uncertainties to the size of the cosmological confidence regions, meaning that an extinction correction using a sharp enough prior is much more akin to simply selecting a low-extinction subset than to performing an assumption-free extinction correction using the $E(B-V)$ measurement uncertainties.

The high-precision measurements of the $R-I$ color afforded by the WFPC2 light curves for the new SNe in this work allow a direct estimation of the host galaxy $E(B-V)$ color excess without any need to resort to any prior assumptions concerning the intrinsic extinction distribution.

Figure 2 shows histograms of the host galaxy $E(B-V)$ values from different samples of the SNe used in this paper. For the bottom two panels, a line is overplotted that treats the H96 low-extinction subset's $E(B-V)$ values as a parent distribution and shows the expected distribution for the other samples given their measurement uncertainties. The low-extinction subset of each sample (*gray histogram*) has a color excess distribution that is consistent with that of the low-extinction subset of H96. Table 7 lists the variance-weighted mean $E(B-V)$ values for the low-redshift SNe and for each sample of high-redshift SNe. Although varying amounts of extinction are detectable in the mean colors of each full sample, the SNe in the low-extinction primary subset (§ 2.5) of each sample are consistent with $E(B-V) = 0$. This subset is consistent with the models of Hatano et al. (1998), discussed above, in which most SNe Ia are observed in regions of very low extinction. We will consider cosmological fits to both this low-extinction subset and the primary subset with host galaxy reddening corrections applied.

Figure 3 shows $E(B-V)$ versus redshift for the 11 SNe of this paper. Three of the lowest redshift SNe are likely to be significantly reddened: SN 1998as at $z = 0.36$, SN 1998aw at $z = 0.44$, and SN 1998ax at $z = 0.50$. This higher incidence of extinguished SNe at the low-redshift end of our sample is consistent with expectations for a flux-limited survey, where extinguished SNe will be preferentially detected at lower redshifts. Indeed, the distribution of $E(B-V)$ values versus redshift shown in Figure 3 is consistent with the results of a Monte Carlo simulation similar to that of Hatano et al. (1998), but including the effects of the survey flux limit.

TABLE 7
MEAN $E(B-V)$ VALUES

Sample	Complete Set	Low-Extinction Primary Subset SNe ^a
Low z	0.095 ± 0.003	-0.001 ± 0.003
P99	0.018 ± 0.024	-0.004 ± 0.025
HST	0.090 ± 0.012	0.012 ± 0.015

^a SNe omitted from our low-extinction primary subset, subset 2 (§ 2.5), have been omitted from these means. This excludes outliers, as well as SNe with both $E(B-V) > 0.1$ and $E(B-V) > 2\sigma$ above zero.

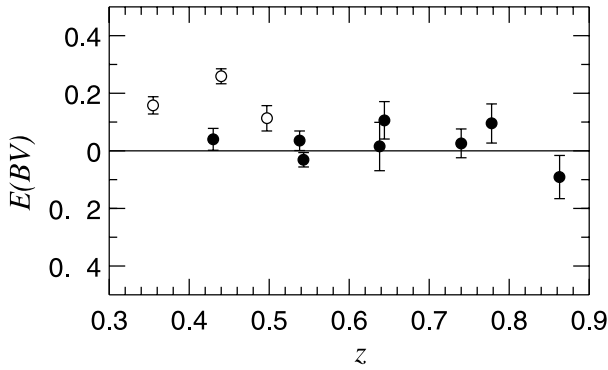


FIG. 3.—Plot of $E(B-V)$ as a function of redshift for the 11 *HST*-observed SNe of this paper, showing that the blue edge of the distribution shows no significant evolution with redshift. (The larger dispersion at lower redshifts is expected for a flux-limited sample.) Error bars include only measurement errors and no assumed intrinsic color dispersion. Filled circles are those SNe in the low-extinction subset (subset 2).

Several authors (including Leibundgut 2001 and Falco et al. 1999) have suggested that there is evidence from the $E(B-V)$ values in Riess et al. (1998) that high-redshift SNe are bluer statistically than their low-redshift counterparts. Our data show no such effect (nor did our P99 SNe).

The mean host galaxy color excess calculated for the highest redshift SNe is critically dependent on the assumed intrinsic $U-B$ color (see § 2.3). An offset in this assumed $U-B$ will affect the high-redshift SNe much more than the low-redshift SNe (whose measurements are primarily of the rest frame B - and V -band light curves). The K -corrected,

rest-frame B -band magnitudes are also dependent on the assumed SN colors that went into deriving the K -corrections. If the assumed $U-B$ color is too red, it will affect the cross filter K -correction applied to R -band data at $z \gtrsim 0.5$, thereby changing derived rest-frame colors. In § 5 we consider the effect of changing the reference $U-B$ color.

4. COSMOLOGICAL RESULTS

4.1. Ω_M and Ω_Λ

Figures 4–6 show Hubble diagrams of effective B -band peak magnitudes and redshifts for the new SNe of this paper; these magnitudes have been K - and stretch-corrected and have been corrected for Galactic extinction. Figure 4 shows all of the data in the low-extinction subset of SNe. For the sake of clarity, Figure 5 shows the same subset, but for this figure SNe with redshifts within 0.01 of each other have been combined in a variance-weighted average. The bottom panel of Figure 5 shows the residuals from an empty universe ($\Omega_M = 0$, $\Omega_\Lambda = 0$), illustrating the strength with which dark energy has been detected. In both Figures 4 and 5, the solid line represents the flat-universe cosmology resulting from our fits to the low-extinction subset. Figure 6 shows just the 11 *HST* SNe from this paper. In the top panel of this figure, the stretch- and K -corrected effective m_B values and uncertainties are plotted. In the bottom panel, effective m_B values have also been corrected for host galaxy extinction based on measured $E(B-V)$ values. The solid line in this figure represents the best-fit flat-universe cosmology to the full primary subset with extinction corrections applied.

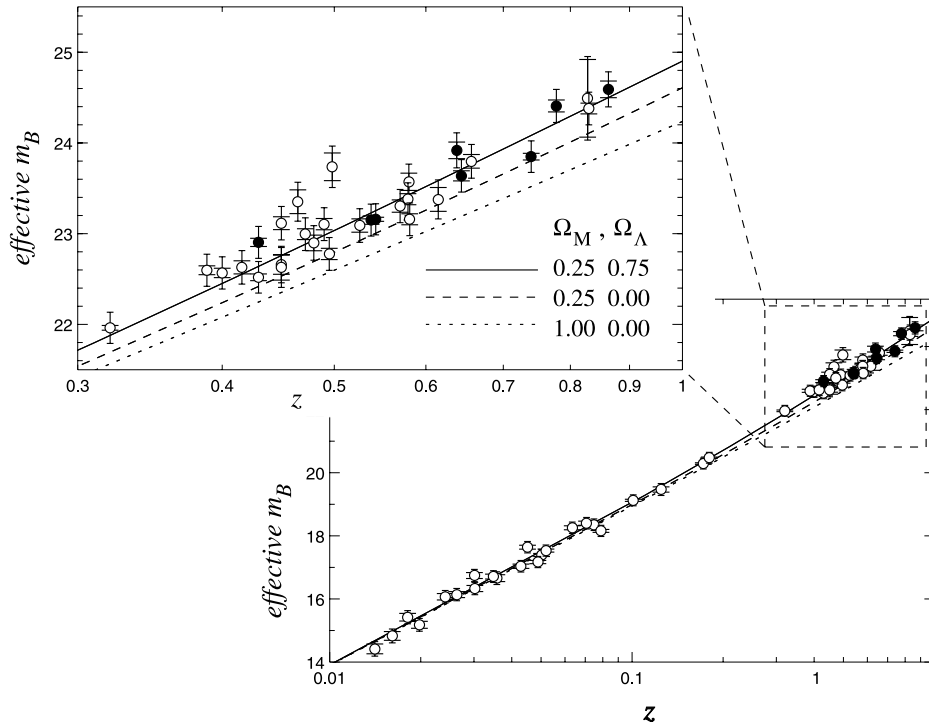


FIG. 4.—Hubble diagram of effective K - and stretch-corrected m_B vs. redshift for the SNe in the primary low-extinction subset. Filled circles represent the *HST* SNe of this paper. Inner error bars show just the measurement uncertainties; outer error bars include 0.17 mag of intrinsic dispersion. The solid line is the best-fit flat-universe cosmology from the low-extinction subset; the dashed and dotted lines represent the indicated cosmologies.

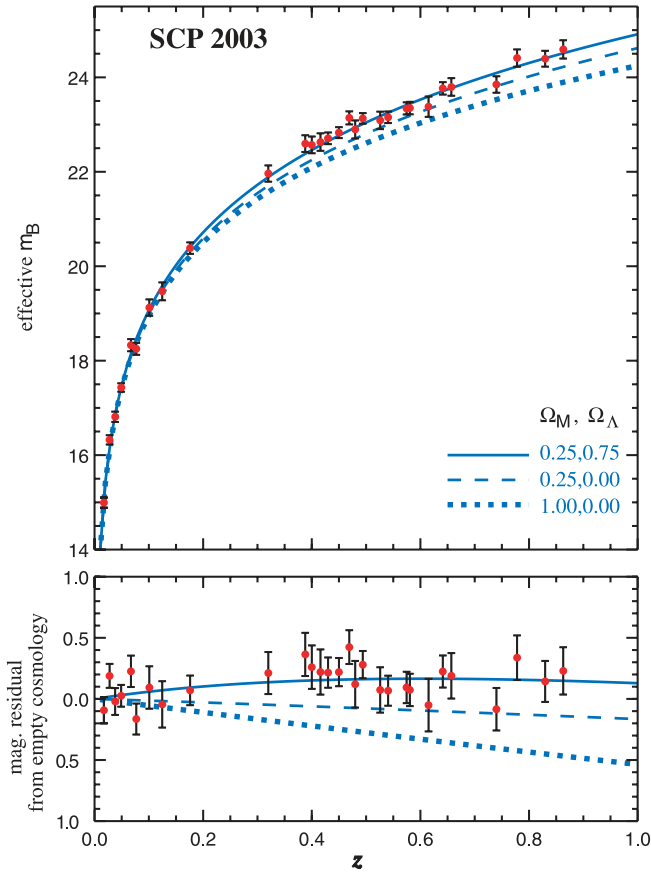


FIG. 5.—*Top*: Averaged Hubble diagram with a linear redshift scale for all SNe from our low-extinction subsample. Here SNe within $\Delta z < 0.01$ of each other have been combined using a weighted average in order to more clearly show the quality and behavior of the data set. (Note that these averaged points are for display only and have not been used for any quantitative analyses.) The solid curve overlaid on the data represents our best-fit flat-universe model, $(\Omega_M, \Omega_\Lambda) = (0.25, 0.75)$ (fit 3 of Table 8). Two other cosmological models are shown for comparison: $(\Omega_M, \Omega_\Lambda) = (0.25, 0)$ and $(\Omega_M, \Omega_\Lambda) = (1, 0)$. *Bottom*: Residuals of the averaged data relative to an empty universe, illustrating the strength with which dark energy has been detected. Also shown are the suite of models from the top panel, including a solid curve for our best-fit flat-universe model.

Table 8 lists results from fits to both of our primary subsets of SNe. SNe from both the H96 and R99 low-redshift samples were included in all fits. The first three lines show fits to the low-extinction primary subset. So that the new sample of high-redshift SNe may be compared to those from P99, each high-redshift sample was fitted separately (fits 1 and 2). Fit 3 combines all of the current SCP high-redshift SNe from the low-extinction subsets and represents the primary result on Ω_M and Ω_Λ for this paper; Figure 7 shows the confidence regions for Ω_M versus Ω_Λ from this fit. Figure 8 shows the comparison of the confidence regions when each high-redshift sample is treated separately. Note that fit 2 provides comparable and consistent measurements of Ω_M and Ω_Λ to fit 1. Additionally, the sizes of the confidence regions from the eight *HST* SNe in fit 2 are similar to those in fit 1, which includes 25 high-redshift SNe from P99.

Fits 4–6 in Table 8 show the results for the primary subset when host galaxy extinction corrections have been applied. Figure 9 compares these results to those of the primary low-extinction fit. The primary fits of Figure 8 are reproduced in the top row of Figure 9. The second row has host galaxy

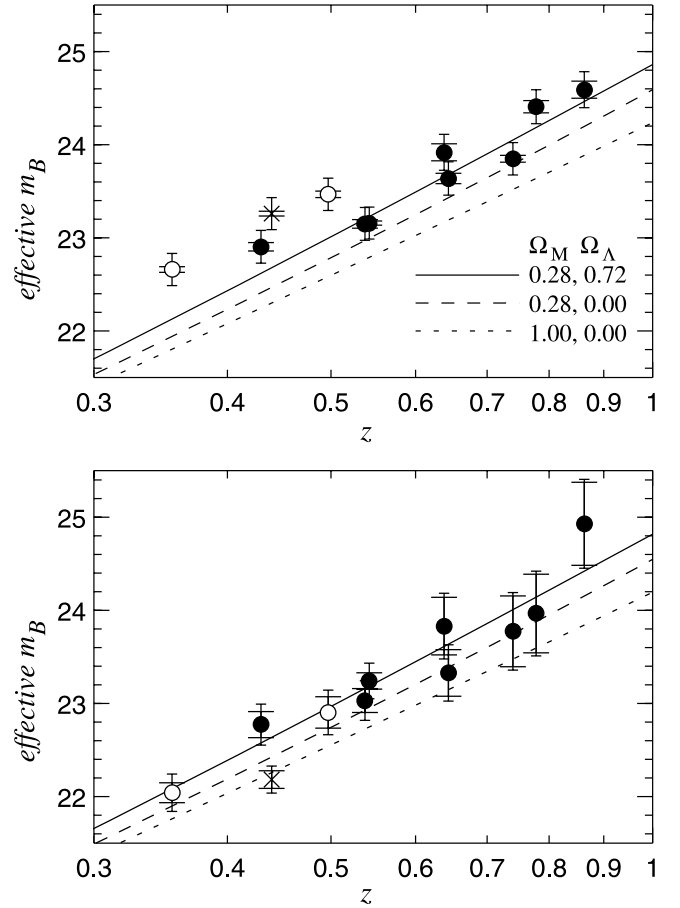


FIG. 6.—Hubble diagram of effective K - and stretch-corrected m_B vs. redshift for the 11 SNe observed with WFPC2 and reported in this paper. Circles represent SNe in the primary subset (subset 1); the one point plotted as a cross (the very reddened supernova SN 1998aw) is omitted from that subset. Open circles represent reddened SNe omitted from the low-extinction primary subset (subset 2), while filled circles are in both subsets 1 and 2. *Top*: No host galaxy $E(B-V)$ extinction corrections have been applied. Inner error bars only include the measurement error. Outer error bars include 0.17 mag of intrinsic dispersion. *Bottom*: Extinction corrections have been applied using the standard interstellar extinction law. Error bars have been increased by the uncertainty in this extinction correction. Again, inner error bars represent only measurement uncertainties, while outer error bars include 0.11 mag of intrinsic dispersion. Lines are for three example cosmologies with the indicated values of Ω_M and Ω_Λ ; the solid line is the best-fit flat-universe cosmology to our full primary subset with extinction corrections applied.

extinction corrections applied using the one-sided prior used by fit E of P99 and Riess et al. (1998) discussed in § 3. The third row has full extinction corrections applied without any prior assumptions on the intrinsic $E(B-V)$ distribution. Three conclusions are apparent from this plot. First, using a strongly peaked prior on extinction prevents the $E(B-V)$ error bars from being fully propagated into the cosmological confidence regions and hence apparently tightens the constraints. However, for a peaked prior, this is very similar to assuming no extinction and not performing an extinction correction (but without testing the assumption), while for a wider prior there is a danger of introducing bias. Second, the current set of SNe provide much smaller confidence regions on the Ω_Λ versus Ω_M plane than do the SNe Ia from previous high-redshift samples when unbiased extinction corrections are applied. Whereas Figure 8 shows

TABLE 8
COSMOLOGICAL FITS

Fit Number	High-Redshift SNe Included in Fit ^a	N_{SNe}	Minimum χ^2	Ω_M for Flat ^b	Ω_Λ for Flat ^b	$P(\Omega_\Lambda > 0)$	\mathcal{M}	α
Fits to the Low-Extinction Primary Subset								
1.....	SNe from P99	46	52	$0.25^{+0.08}_{-0.07}$	$0.75^{+0.07}_{-0.07}$	0.9995	-3.49 ± 0.05	1.58 ± 0.31
2.....	New <i>HST</i> SNe from this paper	29	30	$0.25^{+0.09}_{-0.08}$	$0.75^{+0.08}_{-0.09}$	0.9947	-3.47 ± 0.05	1.06 ± 0.37
3.....	All SCP SNe	54	60	$0.25^{+0.07}_{-0.06}$	$0.75^{+0.06}_{-0.07}$	0.9997	-3.48 ± 0.05	1.47 ± 0.29
Fits to Full Primary Subset, with Extinction Correction								
4.....	SNe from P99	48	56	$0.21^{+0.18}_{-0.15}$	$0.79^{+0.15}_{-0.18}$	0.9967	-3.55 ± 0.05	1.30 ± 0.30
5.....	New <i>HST</i> SNe from this paper	33	39	$0.27^{+0.12}_{-0.10}$	$0.73^{+0.10}_{-0.12}$	0.9953	-3.54 ± 0.05	1.29 ± 0.28
6.....	All SCP SNe	58	65	$0.28^{+0.11}_{-0.10}$	$0.72^{+0.10}_{-0.11}$	0.9974	-3.53 ± 0.05	1.18 ± 0.30

^a All fits include the low-redshift SNe from H96 and R99. See § 2.5 for the definitions of the SN subsets.

^b This is the intersection of the fit probability distribution with the line $\Omega_M + \Omega_\Lambda = 1$.

that the current set of SNe give comparable measurements of Ω_M and Ω_Λ when the low-extinction subsample is used with no host galaxy extinction corrections, Figure 9 shows that the much higher precision color measurements from the WFPC2 data allow us directly to set much better limits on the effects of host galaxy extinction on the cosmological results. Finally, the cosmology that results from the extinction-corrected fits is consistent with the fits to our low-extinction primary subset. Contrary to the assertion of Rowan-Robinson (2002), even when host galaxy extinction

is directly and fully accounted for, dark energy is required with $P(\Omega_\Lambda > 0) > 0.99$.

4.2. Combined High-Redshift Supernova Measurements

Figure 10 shows measurements of Ω_M and Ω_Λ that combine the high-redshift SN data of Riess et al. (1998) together with the SCP data presented in this paper and in P99. The contours show confidence intervals from the 54 SNe of the low-extinction primary subset 2 (used in fit 3 of Table 8), plus the nine well-observed confirmed SNe Ia from Riess et al. (1998) (using the light-curve parameters resulting from their template-fitting analysis); following the criteria of subset 2, SN 1997ck from that paper has been omitted, as that

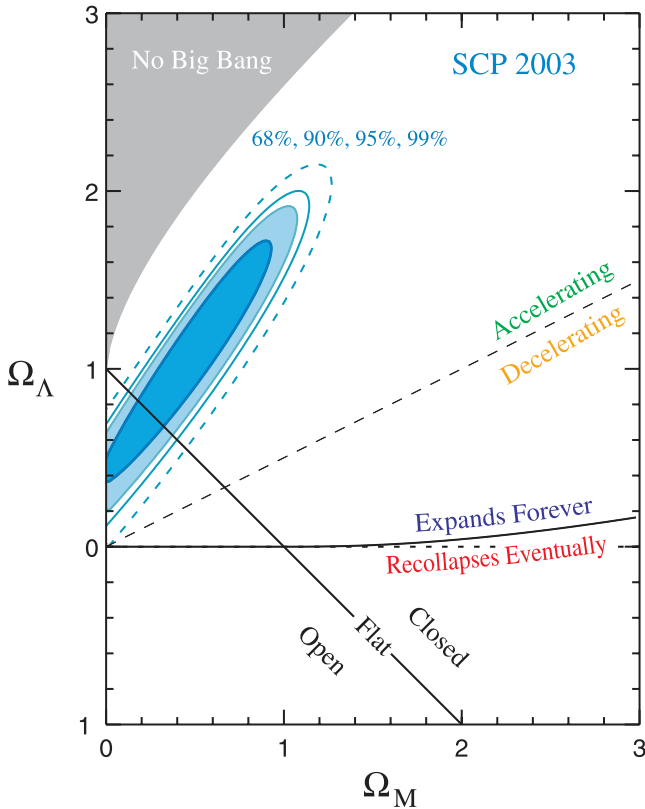


FIG. 7.—Plot of 68%, 90%, 95%, and 99% confidence regions for Ω_M and Ω_Λ from this paper's primary analysis, the fit to the low-extinction primary subset (fit 3).

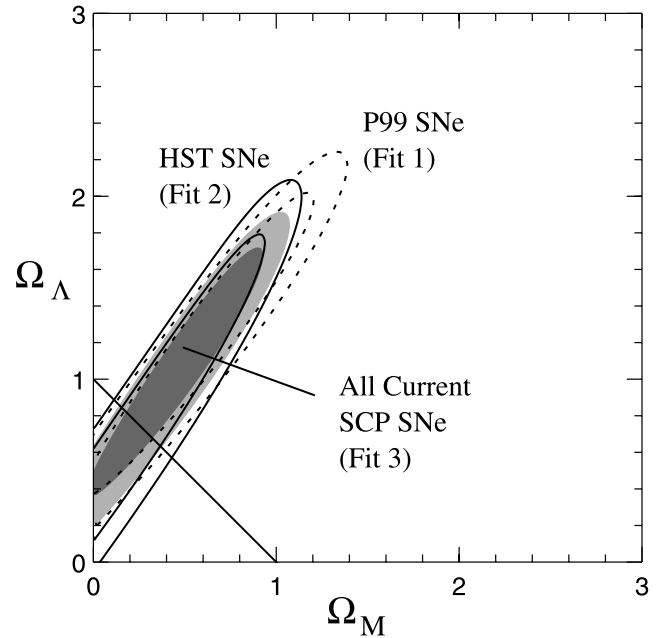


FIG. 8.—Contours indicating 68% and 90% confidence regions for fits to SNe from the low-extinction primary subset, including just the high-redshift SNe from P99 (dotted lines), just the new *HST* high-redshift SNe (solid lines), and all SCP high-redshift SNe (filled contours). The low-redshift SNe from the primary subset are included in all fits. The new, independent sample of high-redshift SNe provide measurements of Ω_M and Ω_Λ consistent with those from the P99 sample.

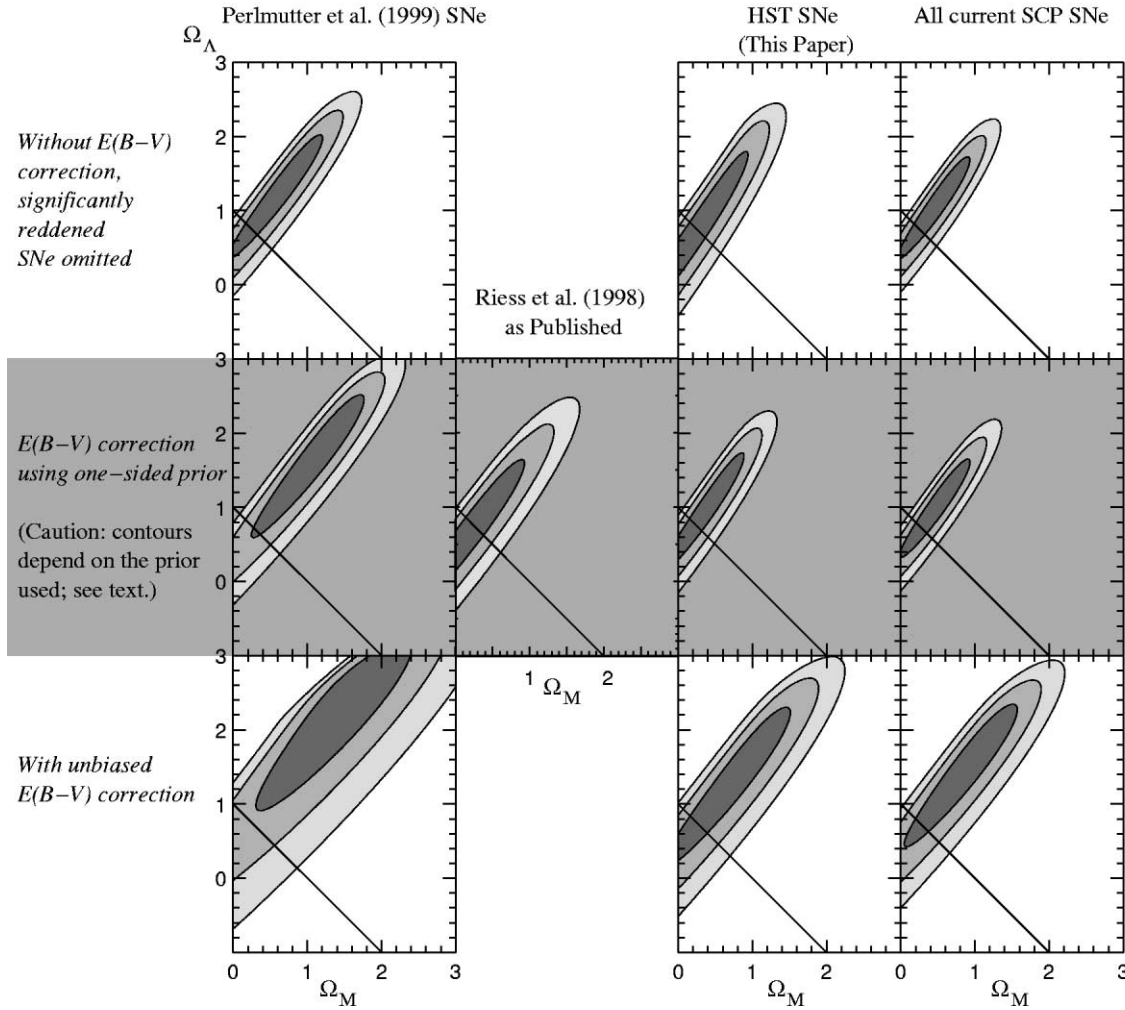


FIG. 9.—Plot of 68.3%, 95.4%, and 99.7% confidence regions for Ω_M and Ω_Λ using different data subsets and methods for treating host galaxy extinction corrections. The top row represents our fits to the low-extinction primary subset, where significantly reddened SNe have been omitted and host galaxy extinction corrections are not applied. The second row shows fits where extinction corrections have been applied using a one-sided extinction prior. These fits are sensitive to the choice of prior and can either yield results equivalent to analyses assuming low extinction (but without testing the assumption) or yield biased results (see text). Note that the published contours from Riess et al. (1998, their Fig. 6; *solid contours*) presented results from fits that included nine well-observed SNe (that are comparable to the primary subsets used in the other panels), but also four SNe with very sparsely sampled light curves, one SN at $z = 0.97$ without a spectral confirmation, as well as two SNe from the P99 set. The third row shows fits with unbiased extinction corrections applied to our primary subset. The *HST* SNe presented in this paper show a marked improvement in the precision of the color measurements and hence in the precision of the Ω_M and Ω_Λ measurements when a full extinction correction is applied. With full and unbiased extinction corrections, dark energy is still required with $P(\Omega_\Lambda > 0) = 0.99$.

SN was not confirmed spectrally. We also omit from Riess et al. (1998) the SNe they measured using the “snapshot” method (as a result of the very sparsely sampled light curve) and two SCP SNe that Riess et al. (1998) used from the P99 data set that are redundant with our sample. This fit has a minimum χ^2 of 65 with 63 SNe. Under the assumption of a flat universe, it yields a measurement of the mass density of $\Omega_M = 0.26^{+0.07}_{-0.06}$, or equivalently a cosmological constant of $\Omega_\Lambda = 0.74^{+0.06}_{-0.07}$. Recent ground-based data on eight new high-redshift SNe from Tonry et al. (2003) (not included in this fit) are consistent with these results. Note that in this fit, the nine SNe from Riess et al. (1998) were not treated in exactly the same manner as the others. The details of the template fitting will naturally have been different, which can introduce small differences (see § 5.1). More importantly, the K -corrections applied by Riess et al. (1998) to derive distance moduli were almost certainly different from those used in this paper.

4.3. Dark Energy Equation of State

The fits of the previous section used a traditional constrained cosmology where Ω_M is the energy density of nonrelativistic matter (i.e., pressure $p = 0$), and Ω_Λ is the energy density in a cosmological constant (i.e., pressure $p = -\rho$, where ρ is the energy density). In Einstein’s field equations, the gravitational effect enters in terms of $\rho + 3p$. If $w \equiv p/\rho$ is the equation-of-state parameter, then for matter $w = 0$, while for vacuum energy (i.e., a cosmological constant) $w = -1$. In fact, it is possible to achieve an accelerating universe so long as there is a component with $w \lesssim -\frac{1}{2}$. (If there were no contribution from Ω_M , only $w < -\frac{1}{3}$ dark energy would be necessary for acceleration; however, for plausible mass densities $\Omega_M \gtrsim 0.2$, the dark energy must have a more negative value of w .) The Hubble diagram for high-redshift SNe provides a measurement of w (P99, Garnavich et al.

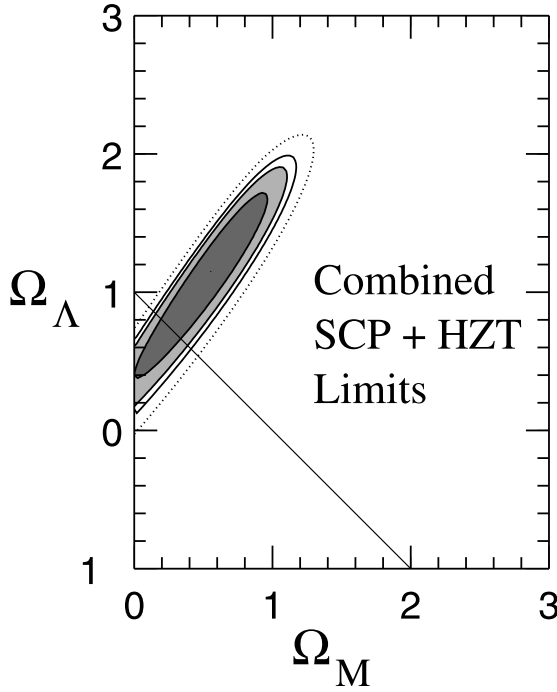


FIG. 10.—Plot of 68%, 90%, 95%, and 99% confidence regions for Ω_M and Ω_Λ , combining the high-redshift data of the SCP (this paper and P99) and Riess et al. (1998). The fit includes subset 2 SNe from the SCP plus the nine well-observed confirmed SNe Ia from Riess et al. (1998).

1998b). Figures 11a and 11b show the joint confidence regions for Ω_M versus w from the SCP SNe, including the new *HST* SNe, under the assumptions that w is constant with time and that the universe is flat, i.e., $\Omega_M + \Omega_X = 1$ (where Ω_X is the energy density in the component with equation of state w , in units of the critical density). The SN alone data set a 99% confidence limit of $w < -0.64$ for any positive value of Ω_M , without any prior assumptions on w .

A fit with extinction corrections applied to the full primary subset (fit 6, shown in Fig. 11b) gives a 99% confidence limit of $w < -1.00$. However, the latter limit should be approached with caution because w is not well bounded from below with the SN data alone. Although Figure 11 only shows confidence intervals down to $w = -2$, the 68% confidence interval from fit 3 extends to $w < -4$, and the 99% confidence interval extends to $w < -10$; these confidence intervals extend to even further negative w in fit 6. The weight of probability at very low (and probably implausible) w pulls the 68% confidence interval in fit 6 (Fig. 11b) downward. A fit that used a prior to restrict w to more reasonable values (say, $w > -2$) would show similar outer confidence intervals but a 68% confidence interval more similar to that of the low-extinction subset in Figure 11a.

Other methods provide measurements of Ω_M and w that are complementary to the SN results. Two of these measurements are plotted in the middle row of Figure 11, compared with the SN measurements (in dotted contours). In filled contours are results from the redshift distortion parameter and bias factor measurement of the Two-Degree Field Galaxy Redshift Survey (2dFGRS; Hawkins et al. 2002;

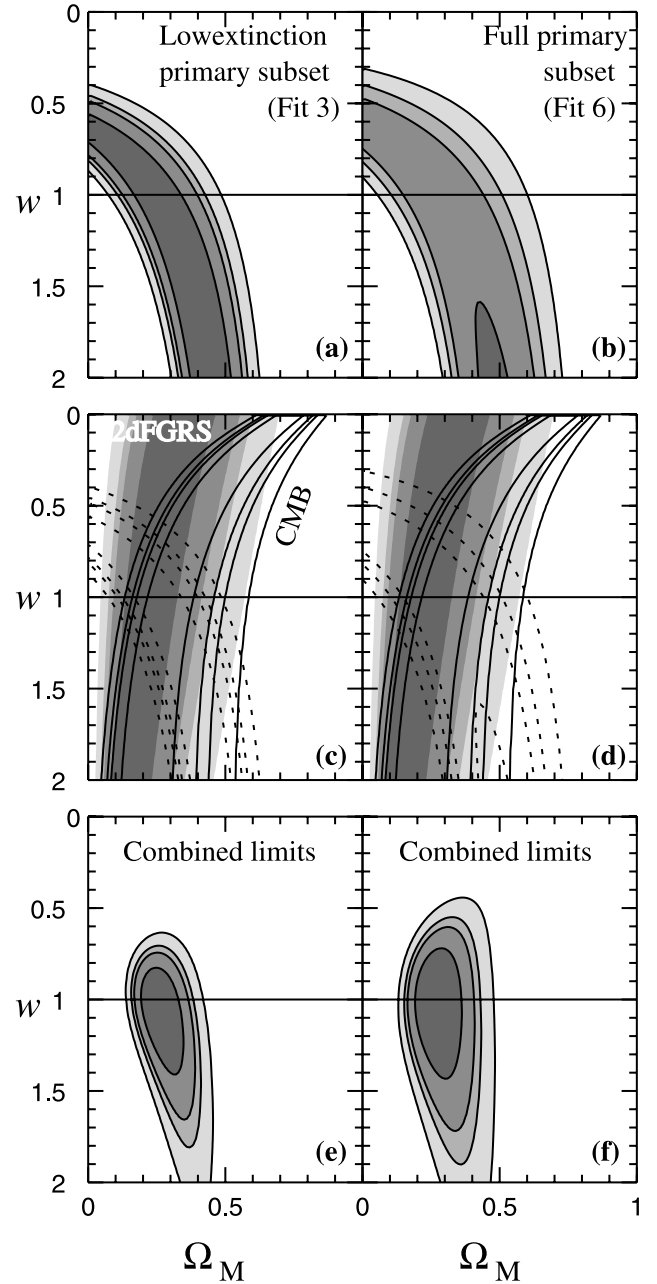


FIG. 11.—Joint measurements of Ω_M and w assuming $\Omega_M + \Omega_X = 1$ and that w is not time varying. Confidence regions plotted are 68%, 90%, 95%, and 99%. The left-hand column shows fits to the low-extinction primary subset; the right-hand column shows fits to the primary subset with unbiased individual host galaxy extinction corrections applied to each SN. The top panels show the confidence intervals from the SCP SNe alone. The middle panels overlay this (dotted lines) with measurements from 2dFGRS (filled contours; Hawkins et al. 2002) and combined CMB measurements (solid contours; Bennett et al. 2003; Spergel et al. 2003). The bottom panels combine the three confidence regions to provide a combined measurement of Ω_M and w .

Verde et al. 2002). These provide a measurement of the growth parameter, $f = 0.51 \pm 0.11$, at the survey redshift $z = 0.15$. We have used the method of Linder & Jenkins (2003) to directly solve for $f(\Omega_M, w, z)$ rather than convert f to Ω_M , as the conversion formula given in Hawkins et al. (2002) is valid only for $w = -1$. Comparison of the

2dFGRS value of f with the calculated values of $f(\Omega_M, w, z)$ yields the joint confidence region for Ω_M and w .³²

The solid lines in Figures 11c and 11d are contours representing confidence regions based on the distance to the surface of last scattering at $z = 1089$ from the *Wilkinson Microwave Anisotropy Probe* (*WMAP*) and other CMB measurements (Bennett et al. 2003; Spergel et al. 2003). For a given Ω_M and w , this reduced distance to the surface of last scattering, I , is given by

$$I = \int_0^{1089} \left\{ [(1 - \Omega_M)/\Omega_M](1 + z)^{3(1+w)} + (1 + z)^3 \right\}^{-1/2} dz. \quad (4)$$

The plotted CMB constraints come from the “WMAPext” sample, which includes other CMB experiments in addition to *WMAP*. They yield a measurement of $I_0 = 1.76 \pm 0.058$, corresponding to $\Omega_M = 0.29$ at $w = -1$. Confidence intervals are generated by calculating a probability using $\chi^2 = [(I - I_0)/\sigma_{I_0}]^2$, where I is calculated for each Ω_M, w .

As both of these measurements show mild correlations between Ω_M and w in a different sense from that of the SN measurement, the combined measurements provide much tighter overall constraints on both parameters. The confidence regions that combine these three measurements are shown in Figures 11e and 11f. When the resulting probability distribution is marginalized over Ω_M , we obtain a measurement of $w = -1.05^{+0.15}_{-0.20}$ (for the low-extinction subset), or $w = -1.02^{+0.19}_{-0.24}$ (for the full primary subset with host galaxy extinction corrections applied). When the probability distribution is marginalized over w , we obtain a flat-universe measurement of $\Omega_M = 0.27^{+0.06}_{-0.05}$ (for the low-extinction subset), or $\Omega_M = 0.28^{+0.06}_{-0.05}$ (for the primary subset with host galaxy extinction corrections applied). The 95% confidence limits on w when our data are combined with CMB and 2dFGRS are $-1.61 < w < -0.78$ for the low-extinction primary subset, or $-1.67 < w < -0.62$ for the full extinction-corrected primary subset. If we add an additional prior that $w \geq -1$, we obtain a 95% upper confidence limit of $w < -0.78$ for the low-extinction primary subset, or $w < -0.67$ for the extinction-corrected full primary subset. These values may be compared with the limit in Spergel et al. (2003), which combines the CMB, 2dFGRS power spectrum, and *HST* Key Project H_0 measurements to yield a 95% upper limit of $w < -0.78$ assuming $w \geq -1$. Although both our measurement and that of Spergel et al. (2003) include CMB data, they are complementary in that our limit does not include the H_0 prior, nor does it include any of the same external constraints, such as those from large-scale structure.

These combined measurements remain consistent with a low-density universe dominated by vacuum energy (constant $w = -1$) but are also consistent with a wide range of other both time-varying w and constant- w dark energy models.

5. SYSTEMATIC ERRORS

The effect of most systematic errors in the Ω_M versus Ω_Λ plane is asymmetric in a manner similar to the asymmetry of

our statistical errors. For the effects listed below, a systematic difference will tend to move the confidence ellipses primarily along their major axis. In other words, these systematic effects produce a larger uncertainty in $\Omega_M + \Omega_\Lambda$ than in $\Omega_M - \Omega_\Lambda$ (or, equivalently, in a measurement of Ω_M or Ω_Λ alone under the assumption of a flat universe). This means that systematic effects do not currently hamper the cosmological measurements from SNe where they have the greatest weight relative to other techniques, nor do they significantly diminish the direct evidence from SNe for the presence of dark energy. However, they do limit the ability of SNe to measure the spatial curvature (“geometry”) of the universe. (Note that the semimajor axis is not precisely in the direction of $\Omega_M + \Omega_\Lambda$, nor is the semiminor axis precisely aligned with $\Omega_M - \Omega_\Lambda$, but since these are useful constraints, we will quantify the systematic uncertainties along these two directions.) Figure 12 shows the effects of some of the systematics discussed in the following subsections.

Systematic effects on flat-universe measurements of w are smaller than the current statistical uncertainties. The right-hand column of Figure 12 shows the effect of the systematics on the Ω_M versus w confidence regions derived from our SN data alone. To quantify the effect of identified systematics in the following subsections, we determine the shift in the maximum likelihood value of w when the SN data are combined with the Ω_M versus w confidence regions from 2dFGRS and the CMB (see § 4.3).

5.1. Fit Method, Subset Selection, and Choice of α

There are multiple reasonable choices for light-curve fitting methods that yield slightly different results for the light-curve parameters. For the SNe in P99, the *R*-band data on high-redshift SNe provided much stronger limits on the stretch (the shape of the light curve) than did more sparse *I*-band light curves. For consistency, in P99 the stretch values for the low-redshift SNe were therefore measured using only the *B*-band light curves.

In this paper there are high-quality photometric measurements from WFPC2 in both *R* and *I* bands. Thus, data in both colors contribute significantly to the constraints on stretch. Additionally, photometry is extracted from *HST* and ground-based images in very different apertures, meaning that different amounts of host galaxy light will be included; this background must be subtracted from each before the two are combined. As such, it is more appropriate to fit these SNe with fixed rather than floating light-curve zero offsets. As this is the most appropriate fit method for the *HST* SNe, the low-redshift SNe should be treated consistently. These procedures that are most appropriate for the *HST* SNe were used for all new fits performed in this paper and listed in Tables 3–5.

To estimate the size of the effect due to these differences in fitting method, cosmological confidence intervals were generated from the “case C” subset of P99 using the new fits presented in this paper and compared to the results quoted in P99 and other variations on the fitting method. Differences in the fit method can change the flat-universe value of Ω_M by ~ 0.03 and the value of $\Omega_M + \Omega_\Lambda$ by up to ~ 0.8 . (This is still much less than the major-axis extent of the statistical confidence ellipse in this direction.) We use these values as the “fit method” systematic uncertainties. We similarly performed joint fits to Ω_M, w in the flat-universe, constant- w case to the SNe from P99 with different light-curve fit

³² Note that we have not used the independent 2dFGRS power spectrum constraint on $\Omega_M h$ because it has not yet been generalized for different values of w .

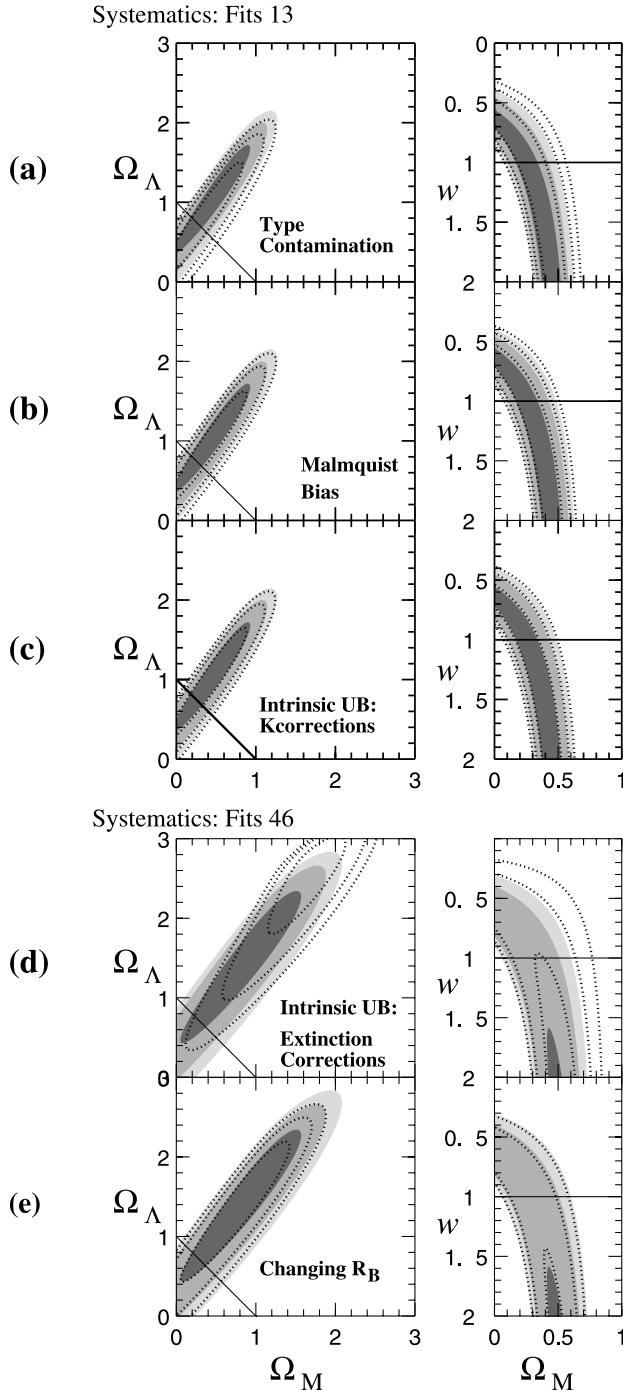


FIG. 12.—Simulated effects of identified systematic errors on the cosmological parameters, estimated by applying the systematic effect to the SN parameters used in the cosmological fits. The left-hand column shows fits to Ω_M and Ω_Λ , and the right-hand column to Ω_M and the dark energy equation-of-state parameter w . The top three rows show our primary fit (fit 3) in filled contours. (a) Dotted contours show the results of a fit to subset 3, only those SNe with the most secure spectral identifications as Type Ia SNe. (b) Dotted contours show a fit to subset 1 where the SN magnitudes have been dimmed to correct for Malmquist bias. (c) Dotted contours show a fit to subset 2, where K -corrections have been applied using a template spectrum with an intrinsic value of $U-B = -0.5$ at the epoch of B maximum. (d) Filled contours show fit 6, the fit to the full primary subset with host galaxy extinction corrections applied; the dotted contours show a fit to the same subset, but using a template spectrum with an intrinsic value of $U-B = -0.5$ for estimating both K -corrections and color excesses. (e) Dotted contours apply extinction corrections to subset 1 using a value of $R_B = 3.5$ rather than the standard $R_B = 4.1$ that was used for fit 6 (filled contours).

methodologies, and from these fits we adopt a fit method systematic uncertainty of 0.02 on constant w (once combined with measurements from 2dFGRS and the CMB).

We have also performed a fit without any stretch correction at all, i.e., using fixed $\alpha = 0$. Although the quality of the fit is worse ($\chi^2 = 82$ with 54 SNe, in comparison to $\chi^2 = 60$ from fit 3), it yields consistent cosmological results, with shifts ($\Delta\Omega_M^{\text{flat}} < 0.01$) much smaller than the already adopted “fit method” systematic. We have likewise performed a fit to the complete set of SNe (including all from P99 with measured colors). The fit cosmological values are similarly consistent with the primary low-extinction fit. We therefore conclude that the effects of these choices are subsumed in the “fit method” systematic.

5.2. Non-Type Ia Supernova Contamination

All subsets of SNe used for cosmological fits in this paper omit SNe for which there is not a spectral confirmation of the SN type. Nonetheless, it is possible in some cases where that confirmation is weak that we may have contamination from non-Type Ia SNe. To estimate such an effect, we performed fits using only those SNe that have a firm identification as Type Ia; this is the “strict-Ia subset” from § 2.5. The comparison between our primary fit (fit 3) and this fit with a more stringent type cut is shown in Figure 12a. This fit has a value of Ω_M in a flat universe that is 0.03 higher than that of fit 3. The value of $\Omega_M + \Omega_\Lambda$ is 0.48 lower than that of fit 3. We adopt these values as our “type contamination” systematic error.

The size of this systematic for w is shown in the right-hand panel of Figure 12a. Combined with CMB and 2dFGRS measurements, the best-fit value of w is larger by 0.07; we adopt this as our type contamination systematic error on w .

5.3. Malmquist Bias

As most of our SNe are from flux-limited samples, they will suffer Malmquist bias (Malmquist 1924, 1936). This effect was discussed extensively in P99, and here we update that discussion to include our new *HST* SNe Ia. For the measurement of the cosmological parameters, it is the difference between the Malmquist bias of the low-redshift and high-redshift samples that matters. In particular, the apparent probability of $\Omega_\Lambda > 0$ is enhanced only if the low-redshift SNe suffer more Malmquist bias than the high-redshift SNe, as this makes the high-redshift SNe Ia seem fainter.

The P99 high-redshift data set was estimated to have little Malmquist bias (0.01 mag) because the SN discovery magnitudes were decorrelated with the measured peak magnitudes. However, for the new *HST* sample, nine of the 11 SNe Ia (selected from larger samples of SNe found in the searches) were found almost exactly at maximum light. This may reflect a spectroscopic flux limit superimposed on the original search flux limit since only spectroscopically confirmed SNe Ia were considered, and of those, generally the higher redshift SNe Ia from a given search were chosen for *HST* for follow-up. In particular, the SNe Ia selected for follow-up from the fall 1997 search were all found at maximum light, while all but SN 1998aw from the spring 1998 search were found at maximum light. SN 2000fr was found well before maximum. Thus, the new high-redshift data set is likely to suffer more Malmquist bias than the P99 data set. Further complicating the interpretation for the high-redshift SNe is the fact that our new *HST* SNe are spread over a wide range in redshift,

such that a single brightness correction for Malmquist bias causes a more complicated change in the fitted cosmological parameters. This is unlike the situation in P99 in which most SNe were at $z \sim 0.5$. Following the calculation in P99 for a high-redshift flux-limited SN sample, we estimate that the maximum Malmquist bias for the ensemble of *HST* SNe is ~ 0.03 mag. However, we caution that it is SNe near the flux limit that are most strongly biased and, therefore, that a subsample comprised of the highest redshift members drawn from a larger flux-limited sample will be more biased. When combined with the P99 high-redshift SNe, the bias is likely to be ~ 0.02 mag since both samples have roughly the same statistical weight.

As for the low-redshift SNe Ia, in P99 we established that since most of the SNe Ia from the H96 flux-limited search were found near maximum, that sample suffered about 0.04 mag of Malmquist bias. On the other hand, some of the R99 SNe Ia were discovered using a galaxy-targeted technique, which therefore is not limited by the SN flux and may be more akin to a volume-limited sample (Li, Filippenko, & Riess 2001). Thus, the addition of the R99 SNe Ia could slightly reduce the overall Malmquist bias of the low-redshift sample. If we were to assume no Malmquist bias for the R99 SNe Ia, and allowing for the fact that they contribute only $\sim \frac{1}{4}$ the statistical weight of the H96 SNe, we estimate that the Malmquist bias in the current low-redshift sample is roughly 0.03 mag.

Since Malmquist bias results in the selection of overly bright SNe at the limits of a flux-limited survey, and since the flux limit can be strongly correlated with redshift,³³ this bias can result in an apparent distortion of the shape of the Hubble diagram. This may affect estimates of the dark energy equation of state. The selection effects for the current high-redshift SNe are not sufficiently well defined to warrant a more detailed modeling of this effect than is presented here. However, for future work, much better control of the selection criteria for SNe Ia at both low- and high-redshift will be required in order to properly estimate the impact of this small bias.

For the current study, however, we simply note that since the *differences* in the Malmquist biases of the high- and low-redshift subsets of SN are likely to be *smaller* in this work than in P99, the current results are less likely to be affected by Malmquist bias. Given the above estimates of 0.03 mag of bias in the low-redshift sample and 0.02 mag of bias in the high-redshift sample, the *difference* in the biases is only 0.01 mag. To perform a quantitative estimate of the effects of Malmquist bias, we have performed a fit by applying the mean offsets described above to each member of a sample in our primary subset. This fit is plotted in Figure 12*b*. The H96 SNe have their magnitudes increased (made dimmer) by 0.04, the P99 SNe by 0.01, and six of the eight *HST* SNe in our primary subset have their magnitudes increased by 0.04. The two *HST* SNe (SN 1998bi and SN 2000fr) that were found before maximum light are assumed not to be biased, and the other nine are offset by 0.04, yielding the above estimated 0.03 mag for the sample. A fit with these changed values to the SN peak magnitudes yields a flat-universe value that is different from our primary fit by $\Omega_M = 0.01$ and a value of $\Omega_M + \Omega_\Lambda$ that is different by 0.18.

The best-fit value of w , when combined with the other cosmological measurements, is 0.03 larger. We adopt these values—all much less than our statistical uncertainties—as our Malmquist bias systematic error.

5.4. *K-Corrections and Supernova Colors*

The generation of the spectral template used for calculating *K*-corrections is described in § 2.3. The degree to which uncertainties in the *K*-correction introduce systematic uncertainties into the cosmological parameters depends on whether or not extinction corrections are being individually applied to SNe. In particular, our *K*-corrections are most uncertain in the rest-frame *U*-band range of the SN spectrum, as a result of limited published spectrophotometry. As discussed in § 2.2, our primary fits use a spectral template that has a color $U-B = -0.4$ at the epoch of *B* maximum. We have investigated the effects on our cosmology of replacing the spectral template used both for *K*-corrections and for determining color excesses with a template that has $U-B = -0.5$ at the epoch of maximum *B* light.

Figure 12*c* shows the effect on the fitted cosmology caused by using the different template for calculating *K*-corrections when individual host galaxy extinction corrections are not applied. These effects are very mild, indicating that our *K*-corrections are robust with respect to the intrinsic $U-B$ color of an SN. Based on the comparison of these fits, we adopt a *K*-correction systematic uncertainty of 0.13 on $\Omega_M + \Omega_\Lambda$ and of 0.01 in w ; the systematic uncertainty on the flat-universe value of Ω_M due to this effect is negligible.

Although the effects of a different intrinsic $U-B$ color on the *K*-corrections are mild, the effects on calculated color excesses are much greater. Figure 12*d* shows the difference between fit 6, where host galaxy extinction corrections have been applied using our standard color excess values, and a fit where color excess values have been determined assuming that the intrinsic $U-B$ color of an SN is -0.5 at maximum light. As with other systematics, the primary effect is to move the confidence intervals along their major axis. In this case, the large shift in $\Omega_M + \Omega_\Lambda$ is mainly due to the fact that with this bluer reference $U-B$ color, we would believe that all of our $z > 0.7$ SNe are suffering from an amount of host galaxy extinction that is greater than that suffered by SNe at lower redshift. Given that the more distant SNe are dimmer and thus closer to our detection limits than the moderate-redshift SNe, this scenario is implausible. If anything, one would expect the higher redshift SNe to be *less* subject to host galaxy extinction due to selection effects. Nonetheless, a value of $U-B = -0.5$ at the epoch of *B*-band maximum is currently possible given the *U*-band information available. Only for those fits where extinction corrections are applied, we have an additional intrinsic $U-B$ systematic error of 0.07 on the flat-universe value of Ω_M and a systematic error of 1.78 on $\Omega_M + \Omega_\Lambda$. The systematic uncertainty on w is 0.10. It is likely that these values represent an overestimate of this systematic.

5.5. *Dust Properties*

As discussed in § 3, Phillips et al. (1999) found that some of the reddest SNe at low redshift appear to be overcorrected for extinction given the standard reddening law. As shown in the bottom panel of Figure 6, our most reddened high-redshift SN (SN 1998as, which is omitted from the primary subset) is similarly overcorrected. One possible

³³ They are 100% correlated for a single field, but this correlation can be diluted by combining fields of different depths.

explanation is that a lower value of R_B is appropriate for SN Ia host galaxies. If we use a value of $R_B = 3.5$ (Phillips et al. 1999) rather than the standard value of $R_B = 4.1$ to perform extinction corrections, it slightly changes the best-fit cosmological values for fits where extinction corrections are applied (fit 6); this change is shown in Figure 12e. The best-fit value of $\Omega_M + \Omega_\Lambda$ changes by 0.18, and the best-fit value of w when combined with the other cosmological measurements changes by 0.01; this systematic has a negligible effect on the flat-universe value of Ω_M .

A related source of systematic error is possible evolution in the properties of the host galaxy dust. To examine the scale of the effect, we consider a situation where dust in $z < 0.3$ spiral galaxies has a Cardelli, Clayton, & Mathis (1989) $R_V = 3.1$ law, whereas higher redshift galaxy dust has a ratio of selective-to-total extinction that is half as large, i.e., $R_V = 1.6$. We use the Monte Carlo code described in Kim et al. (2003) to study the bias induced when an $R_V = 3.1$ extinction correction is inappropriately applied to all SNe. We incorporate the redshift and $E(B-V)$ distributions of the SNe considered in this paper and an $E(B-V) < 0.1$ cut is applied. For an input cosmology of $\Omega_M = 0.21$ and $\Omega_\Lambda = 0.79$, we find a modest shift in the cosmological parameters to $\Omega_M = 0.25$ and $\Omega_\Lambda = 0.77$ without assuming a flat universe.

This bias moves almost exactly along the line $\Omega_M + \Omega_\Lambda = 1$, increasing uncertainty along the thin axis of the error contour. However, the extreme difference in dust properties considered in the Monte Carlo contributes a shift in the cosmological parameters that is less than 1σ of our quoted statistical error bars. We adopt 0.04 as the “dust evolution” systematic uncertainty on Ω_M in a flat universe for those fits where host galaxy extinction corrections are applied; this particular systematic is insignificant along the major axis of the confidence ellipses.

The flat-universe value of w , when combined with the 2dFGRS and CMB results, increases by 0.06 under this simple model of dust evolution. We adopt this as the dust evolution systematic on w for those fits where host galaxy extinction corrections are applied.

5.6. Gravitational Lensing

Gravitational lensing decreases the modal brightness and causes increased dispersion and positive skewness in the Hubble diagram for high-redshift SNe. The size of the effect depends on the fraction of compact objects of the total mass density of the universe, Ω_M . This has been discussed in some detail in the literature (Wambsganss et al. 1997; Frieman 1997; Holz 1998; Kantowski 1998; Seljak & Holz 1999; Metcalf & Silk 1999; Metcalf 1999; Holz 2001; Wang, Holz, & Munshi 2002; Minty, Heavens, & Hawkins 2002; Amanullah, Mörtzell, & Goobar 2003; Dalal et al. 2003; Oguri, Suto, & Turner 2003), especially in relation to the P99 and Riess et al. (1998) SN data sets. A very conservative assumption of an “empty beam” model in a universe filled with compact objects allowed P99 to demonstrate that gravitational lensing does not alter the case for dark energy.

Gravitational lensing may result in a biased determination of the cosmological parameter determination, as discussed in Amanullah et al. (2003). The potential bias increases with the redshift of the SNe in the sample. For example, for the most distant known SN Ia, SN 1997ff at $z = 1.7$, there is evidence for significant magnification,

$\Delta m \sim -0.3$ (Lewis & Ibata 2001; Mörtzell, Gunnarsson, & Goobar 2001; Benitez et al. 2002).

As the SN sample considered in this paper does not reach as far, the (de)magnification distortions are expected to be small, in general below 0.05 mag, and less than 1% for the cases considered in P99. To estimate the systematic uncertainties in the cosmological parameters, we have used the SNOC package (Goobar et al. 2002b) to simulate 100 realizations of our data sets assuming a 20% universal fraction of Ω_M in compact objects, i.e., of the same order as the halo fraction deduced for the Milky Way from microlensing along the line of sight to the Large Magellanic Cloud (Alcock et al. 2000). The light beams are otherwise assumed to travel through space randomly filled with galaxy halos with mass density equally divided into SIS and NFW profiles, as described in Bergström et al. (2000). According to our simulations, we find that (for a flat universe) the fitted value of Ω_M is systematically shifted by 0.01 on the average, with a statistical dispersion $\sigma_{\Delta\Omega_M} = 0.01$. We adopt 0.01 as our gravitational lensing systematic error in the flat-universe value of Ω_M . The effect on $\Omega_M + \Omega_\Lambda$ is very small compared to other systematics, biasing the sum by only 0.04.

The simulated offsets due to gravitational lensing, when combined with CMB and galaxy redshift distortion measurements, increase the value of w by 0.05; we adopt this as a gravitational lensing systematic on w .

5.7. Supernova Population Drift

In P99 we discussed in detail whether the high-redshift SNe Ia could have systematically different properties than low-redshift SNe Ia and, in particular, whether intrinsic differences might remain after correction for stretch. One might imagine this to occur if the range of the physical parameters controlling SN Ia brightnesses have little overlap between low and high redshift such that corrections applied to low redshift are inappropriate or incomplete for high-redshift SNe Ia. Since P99, considerable additional work has been done to address this issue.

In addition to comparisons of stretch range (P99), as well as spectral (Perlmutter et al. 1998; Coil et al. 2000) and light-curve (Goldhaber et al. 2001) features, several tests performed directly with the P99 high-redshift SNe Ia have shown excellent consistency with low-redshift SNe Ia. Most recently, in Sullivan et al. (2003) we have presented results on the Hubble diagram of distant SNe Ia from P99 that have been morphologically typed with *HST*. We found no difference in the cosmological results from their morphologically segregated subsamples. In particular, E/S0 galaxies, for which one expects the tightest possible correlation between progenitor mass and redshift, not only agree with the cosmological fits using only spiral galaxies but by themselves confirm the results of P99. This is strong evidence that, while age or metallicity could in principle affect the brightnesses of SNe Ia, stretch correction eliminates these differences. Likewise, the light-curve rise time, a possible indicator of the energetics of the SN explosion (see Nugent et al. 1995; Hoefflich et al. 1998), while initially suggested to be different between high- and low-redshift SNe Ia (Riess et al. 1999a), has been demonstrated to agree very well (within 1.8 ± 1.2 days; Aldering et al. 2000).

On the theoretical side, the SN formation models of Kobayashi et al. (1998) and Nomoto, Nakamura, & Kobayashi (1999) suggest that the progenitor binary system must have $[\text{Fe}/\text{H}] > -1$ in order to produce an SN Ia. This would impose a lower limit to the metallicities of all SNe Ia and thus limit the extent of any metallicity-induced brightness differences between high- and low-redshift SNe Ia. On the empirical side, the lack of a gradient in the intrinsic luminosities of SNe Ia with galactocentric distance, coupled with the fact that metallicity gradients are common in spiral galaxies (Henry & Worthey 1999), leads Ivanov, Hamuy, & Pinto (2000) to suggest that metallicity is not a key parameter in controlling SN Ia brightnesses at optical wavelengths, although note that Lentz et al. (2000) show how it can affect the ultraviolet. In addition, Hamuy et al. (2000) find that light-curve width is not dependent on host galaxy metallicity.

Alternatively, population age effects, including pre-explosion cooling undergone by the progenitor white dwarf and other effects linked to the mass of the primary exploding white dwarf, have been suggested (for a review see Ruiz-Lapuente 2003). As the local sample of SNe Ia represents populations of all ages and metallicities, both effects can be studied locally. Several low-redshift studies have presented data suggesting that SN Ia intrinsic luminosities (i.e., those prior to stretch correction) may correlate with host galaxy environment (Hamuy et al. 1996a, 2000; Branch, Romanishin, & Baron 1996; Wang et al. 1997, 2003; Ivanov et al. 2000; Howell 2001; R99). These findings are actually encouraging, since unlike stretch itself, there is some hope that host galaxy environment variations can be translated into physical parameters such as age and metallicity. These parameters can help relate any drifts in the SN Ia population to evolution of the host galaxies.

More importantly for cosmology, R99 used their sample of 22 local SNe Ia to demonstrate that any brightness variations between SNe Ia in different host galaxy environments disappear after correction for light-curve width. We have quantified this agreement using a larger local sample of SNe compiled in Wang et al. (2003), 14 of which have E/S0 hosts and 27 of which have spiral hosts. We find that after light-curve-width correction there can be less than a 0.01 ± 0.05 mag offset between SNe Ia in local spiral and elliptical galaxies. This indicates that light-curve width is able to correct for age or other differences.

Finally, Wang et al. (2003) demonstrate a new method, CMAGIC, which is able to standardize the vast majority of local SNe Ia to within 0.08 mag (in contrast to ~ 0.11 mag, which light-curve-width corrections can attain; Phillips et al. 1999). This imposes even more severe limits on the fraction of SNe Ia generated by any alternate progenitor scenario or requires that variations in the progenitor properties have little effect on whether the resulting SN can be standardized.

The data from the new SNe Ia presented here do offer one new test for consistency between low- and high-redshift SNe Ia. The quality of our *HST* data provides measurements of the SN peak magnitudes and light-curve widths rivaling those for nearby SNe Ia. This allows a direct comparison between the stretch-luminosity relations at low and high redshifts. Figure 13 shows that the *HST* high-redshift SNe are found at similar stretches and luminosities as the low-redshift SNe. The low- and high-redshift samples are consistent with the same stretch-luminosity relationship, although

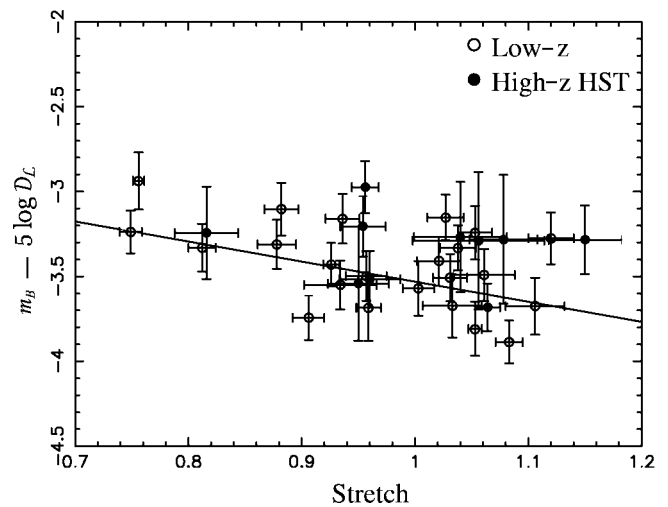


FIG. 13.—Stretch-luminosity relationship for low-redshift SNe (*open circles*) and high-redshift *HST* SNe (*filled circles*). Each point is the K -corrected and extinction-corrected m_B for that SN, minus \mathcal{D}_L , the “Hubble constant-free luminosity distance” (see § 2.4), plotted against the stretch of that SN. The line drawn represents the best-fit values of α and M from fit 6, the fit to all subset 1 SNe with host galaxy extinction corrections applied. Note in particular that our *HST* SNe Ia all have low-redshift counterparts.

it is primarily the low-redshift SNe that require a nonzero slope for this relationship.

5.8. Possible Additional Sources of Systematic Uncertainties

Other potential sources of systematic uncertainties have been suggested. Aguirre (1999a, 1999b) and Aguirre & Zoltan (2000) argued that the presence of “gray” dust, i.e., a homogeneous intergalactic component with weak differential extinction properties over the rest-frame optical wavelength regime, could not be ruled out by the P99 data. Since then, measurements of an SN Ia at $z \simeq 1.7$ (Riess et al. 2001) were claimed to rule out the gray dust scenario as a noncosmological alternative explanation to the dimming of high-redshift SNe; however, there remain some outstanding issues with this interpretation (e.g., Goobar, Bergström, & Mörtzell 2002a; Blakeslee et al. 2003). A direct test for extinction over a wide wavelength range, rest-frame $B-I$ has been performed by Riess et al. (2000) on a single SN at $z = 0.46$, SN 1999Q, which showed no gray dust signature (however, see Nobili et al. 2003). Although the situation remains inconclusive, there is no direct evidence that gray dust is a dominant source of uncertainties. It remains an important issue to be addressed by future data sets, including near-infrared observations.

More recently, the possibility of axion-photon oscillations making high-redshift SNe appear dimmer was suggested by Csáki, Kaloper, & Terning (2002). This attenuation would be wavelength dependent and thus could be explored with spectroscopic studies of high-redshift sources (Mörtzell, Bergstrom, & Goobar 2002). Preliminary studies of QSO spectra between $z = 0.15$ and 5.3 set a very conservative upper limit on the possible dimming of $z \sim 0.8$ SNe to 0.2 mag (Mörtzell & Goobar 2003).

For the current data sample, the above-mentioned sources of systematic uncertainties are difficult to quantify at present but are believed to be subdominant in the total error budget.

TABLE 9
IDENTIFIED SYSTEMATIC UNCERTAINTIES

SOURCE OF UNCERTAINTY	SYSTEMATIC UNCERTAINTY			NOTES
	Flat Universe Ω_M or Ω_Λ	$\Omega_M + \Omega_\Lambda$	Constant w^b	
Fit method	0.03 (0.5 σ)	0.80	0.02	
Type contamination.....	0.03 (0.5 σ)	0.48	0.07	
Malmquist bias	0.01 (0.2 σ)	0.18	0.03	
Intrinsic $U-B$: K -corrections	0.00 (0.0 σ)	0.13	0.01	1
Gravitational lensing	0.01 (0.2 σ)	0.04	0.05	
Systematic with host galaxy extinction corrections:				
Intrinsic $U-B$: color excess.....	0.07 (0.7 σ)	1.78	0.10	2
Extinction slope	0.00 (0.0 σ)	0.18	0.01	2
Dust evolution	0.03 (0.3 σ)	0.02	0.06	2

NOTES.—(1) Only used where host galaxy extinction corrections are not applied. (2) Only used where host galaxy extinction corrections are applied.

^a Each systematic is given as an offset from the flat-universe value of Ω_M and in terms of the smaller side of the statistical error bar (0.06 for fit 3 to the low-extinction subset, 0.10 for fit 6 to the full primary subset).

^b This is the offset on the maximum likelihood value of w when the fit is combined with the 2dFGRS and CMB measurements.

5.9. Total Identified Systematic Uncertainty

The identified systematic errors are summarized in Table 9. Adding together these errors in quadrature, we obtain a total systematic error of 0.04 on the flat-universe value of Ω_M (along approximately the minor axis of the confidence ellipses shown in Ω_M vs. Ω_Λ plots); this is smaller than but approaching our statistical uncertainty of 0.06. The total systematic uncertainty on $\Omega_M + \Omega_\Lambda$ is 0.96 (along approximately the major axis of the confidence ellipses). Finally, for the low-extinction subset, we have a systematic uncertainty on constant w of 0.09, less than our high-side statistical uncertainty of 0.15.

For fits with host galaxy extinction corrections applied, we have to consider the additional systematic effects of an uncertainty in the intrinsic value of $U-B$ on determined color excesses and of dust properties. In this case, we have a total systematic error of 0.09 on the flat-universe value of Ω_M or Ω_Λ and a total systematic error of 2.0 on $\Omega_M + \Omega_\Lambda$; as discussed in § 5.4, this is likely to be an overestimate of the true systematic error. The total systematic uncertainty on constant w for the extinction-corrected full primary sample is 0.15.

6. SUMMARY AND CONCLUSIONS

Our conclusions are as follows:

1. We present a new, independent set of 11 high-redshift SNe ($z = 0.36$ – 0.86). These SNe have very high quality photometry measured with WFPC2 on the *HST*. The higher quality light-curve measurements have small enough errors on each $E(B-V)$ measurement to allow an unbiased correction of host galaxy reddening. We have performed improved color and K -corrections, necessary to combine WFPC2 photometric filters with ground-based photometric filters.

2. The cosmological fits to Ω_M and Ω_Λ are consistent with the SCP's previous results (P99), providing strong evidence for a cosmological constant. This is a significant confirmation of the results of P99 and Riess et al. (1998) and represents a completely new set of high-redshift SNe yielding the same results as the earlier SN work. Moreover, these results

are consistent with a number of other cosmological measurements and, together with other current cosmological observations, are pointing toward a consensus $\Omega_M \sim 0.3$, $\Omega_\Lambda \sim 0.7$ universe.

3. Most identified systematic errors on Ω_M and Ω_Λ affect the cosmological results primarily by moving them along the direction where the statistical uncertainty is largest, that is, along the major axis of the confidence ellipses. Systematics are much smaller along the minor (approximately $\Omega_M - \Omega_\Lambda$) axis of the confidence regions and may be described by giving the systematic error on Ω_M or Ω_Λ alone in the flat-universe case. Our total identified systematic error for the low-extinction sample analysis is 0.04 on the flat-universe value of Ω_M or Ω_Λ . For fits with host galaxy extinction corrections, a conservative estimate of the total identified systematic error is 0.09. In the more uncertain major axis, our total identified systematic error is 0.96 on $\Omega_M + \Omega_\Lambda$ for the low-extinction primary subset and 2.0 on the extinction-corrected full primary subset. Given the large size of these systematics in this direction, any conclusions drawn from the positions of SN confidence ellipses along this direction should be approached with caution.

4. Under the assumption of a flat universe with vacuum energy (constant $w = -1$), we find a value of $\Omega_M = 0.25^{+0.07}_{-0.06}$ (statistical) ± 0.04 (identified systematic), or equivalently, a cosmological constant of $\Omega_\Lambda = 0.75^{+0.06}_{-0.07}$ (statistical) ± 0.04 (identified systematic). This result is robust to host galaxy extinction, and a fit with full, unbiased, individual extinction corrections applied yields a flat-universe cosmological constant of $\Omega_\Lambda = 0.72^{+0.10}_{-0.11}$ (statistical) ± 0.09 (identified systematic). Our best confidence regions for Ω_M versus Ω_Λ are shown in Figure 7.

5. When combined with the 2dFGRS galaxy redshift distortion measurement and recent CMB data, we find a value for the dark energy equation-of-state parameter $w = -1.05^{+0.15}_{-0.20}$ marginalizing over Ω_M (or a mass density $\Omega_M = 0.27^{+0.06}_{-0.05}$ marginalizing over w), under the assumptions that the universe is spatially flat and that w is constant in time. The identified systematic uncertainty on w is 0.09. The current confidence regions on the flat-universe values of Ω_M and w are shown in Figure 11. The SN data are consis-

tent with a low-mass universe dominated by vacuum energy ($w = -1$), but they are also consistent with a wide range of constant or time-varying dark energy models.

In summary, high-redshift SNe continue to be the best single tool for directly measuring the density of dark energy. This new set of SNe observed with the *HST* confirm and strengthen previous SN evidence for an accelerating universe and show that those results are robust even when host galaxy extinction is fully accounted for. High-redshift SNe, together with other cosmological measurements, are providing a consistent picture of a low-mass, flat universe filled with dark energy. The next task for cosmologists is to better measure the properties of the dark energy, so as to further our understanding of its nature. Combinations of current cosmological techniques have begun to provide measurements of its most general property (specifically, the equation-of-state parameter when it is assumed to be constant). Future work will refine these measurements and, in particular, reduce the systematic uncertainties that will soon limit the current series of SN studies. As new instruments become available,³⁴ it will begin to be possible to relax the condition of a constant equation-of-state parameter and to question whether the properties of the dark energy have been changing throughout the history of the universe.

The authors wish to thank our *HST* program coordinator, Doug Van Orsow, and the excellent *HST* support staff for their help in the planning, scheduling, and execution of the observations presented herein. Support for this work was provided by NASA through grants HST-GO-07336.01-A and HST-GO-08346.01-A from the Space Telescope Science Institute, which is operated by the Association of Universities for Research in Astronomy, Inc., under NASA contract NAS 5-26555. The authors are indebted to Malcolm Smith and Patrick Hall for trading several crucial hours of observing time at the CTIO 4 m, which played a key role in our SN search in 1998 March. The authors acknowledge the tremendous help of the night assistants and support staff at the many telescopes from which data for this paper were obtained; we are particularly grateful to the CTIO staff for crucial support during our key search nights and to Di Harmer and Paul Smith of the WIYN Queue. We thank Gary Bernstein and Tony Tyson for developing and supporting the Big Throughput Camera at the CTIO 4 m. This wide-field camera was important in the discovery of most of the high-redshift SNe presented in this paper and enabled the high discovery rate needed to guarantee SNe for follow-up with *HST*. The authors are grateful to Eric Linder for the use of his growth parameter solver and to Ramon Miguel for assistance with gravitational lensing calculations. We also wish to acknowledge NOAO for providing and supporting the astronomical data reduction package IRAF. The authors wish to recognize and acknowledge the very significant cultural role and reverence that the summit of Mauna Kea has always had within the indigenous Hawaiian community. We are most fortunate to have the opportunity to conduct observations from this mountain. This work was supported in part by the Director, Office of Science, Office of High Energy and Nuclear Physics, of the US Department of Energy under Contract DE-AC03-76SF000098, by the Center for Particle Astrophysics, an NSF Science and Technology Center operated by the University of California, Berkeley, under Cooperative Agreement

AST 91-20005. This work was supported in part by a NASA LTSA grant to P. E. N., G. A., S. P., and S. E. D., and W. M. W.-V. was supported in part by a National Science Foundation Graduate Research Fellowship. A. G. is a Royal Swedish Academy Research Fellow supported by a grant from the Knut and Alice Wallenberg Foundation.

APPENDIX

LIGHT-CURVE DATA

Tabulated below are light-curve data for the 11 *HST* SNe presented in this paper (see Tables 10–31). For each event, there are two light curves, one for *R* band and one for *I* band. All photometry has been color-corrected to the standard Bessel filters as described in § 3, using color corrections that assume the light-curve parameters in Table 3. These light curves, together with a $7'' \times 7''$ thumbnail of the F675W WFPC2 image closest to maximum light, are shown in Figure 1. Note that there are correlated errors between the data points. For the ground-based data, there is a covariance because for a given SN the same final reference images were subtracted from all other ground-based points. Similarly, the *HST* data include a covariance due to a single background model having been used for all points for a given SN (see § 2.1). In addition to this, the relative photometric zero-point magnitudes were determined separately for the ground-based and *HST* photometry; in the former case, standard stars from Landolt (1992) were used to measure magnitudes of secondary standard stars in the SN field of view. In the latter case, zero points from Dolphin (2000) were used. These covariance matrices will be available from the SCP Web site.³⁵

Because uncertainties are flux uncertainties rather than magnitude uncertainties, each light curve is presented in arbitrary flux units. For each light curve, the zero point necessary to convert these to magnitudes is given. The magnitude may be calculated using the standard formula:

$$m = -2.5 \log f + m_{zp}, \quad (A1)$$

where m_{zp} is the quoted zero point and f is the flux value from the table. (Because we include early-time and late-time light-curve points when the SN flux is undetected given our photometry errors, some of the measured fluxes scatter to negative values. Note that it is impossible to formally calculate a magnitude for these points and also that flux values are the proper way to quote the data as they better reflect the units in which our photometry errors are approximately Gaussian.)

The telescope used for each data point is indicated. BTC represents the Big Throughput Camera on the CTIO 4 m telescope. CTIO represents the prime focus imager on the CTIO 4 m telescope. WIYN represents the Nasmyth $2k \times 2k$ imager on the WIYN 3.5 m telescope at Kitt Peak observatory. INT represents the WFC (wide-field camera) on the INT 2.5 m telescope at La Palma. KECK represents the LRIS imager on the Keck 10 m telescope. NTT represents the SUSI-2 imager on the NTT 3.6 m telescope at ESO. CFHT represents the CFHT12K multichip imager on the 3.6 m CFHT telescope on Mauna Kea in Hawaii. Finally, HSTPC indicates data obtained from the Planetary Camera CCD on WFPC2.

³⁴ See, e.g., <http://snap.lbl.gov>.

³⁵ Available at <http://supernova.lbl.gov>.

TABLE 10
SN 1997EK-*R*

Julian Day (−2,400,000)	Flux ^a	Telescope
50780.63.....	0.24 ± 1.27	BTC
50780.69.....	0.57 ± 0.93	BTC
50781.61.....	−0.28 ± 1.05	BTC
50781.66.....	1.22 ± 0.89	BTC
50781.67.....	0.29 ± 0.89	BTC
50781.72.....	0.16 ± 1.01	BTC
50810.58.....	2.71 ± 1.28	BTC
50810.59.....	4.63 ± 1.29	BTC
50810.60.....	5.25 ± 1.24	BTC
50810.67.....	4.85 ± 1.32	BTC
50810.68.....	5.04 ± 1.24	BTC
50810.69.....	5.70 ± 1.28	BTC
50811.66.....	4.34 ± 1.10	BTC
50811.68.....	4.53 ± 1.07	BTC
50811.69.....	3.55 ± 1.22	BTC
50817.67.....	4.92 ± 0.91	BTC
50817.68.....	5.09 ± 0.84	BTC
50817.69.....	3.17 ± 0.83	BTC
50817.70.....	2.65 ± 0.84	BTC
50817.71.....	3.71 ± 0.85	BTC
50817.72.....	3.34 ± 1.02	BTC
50817.73.....	4.45 ± 1.06	BTC
50817.73.....	4.77 ± 1.04	BTC
50817.74.....	3.10 ± 1.04	BTC
50818.92.....	4.18 ± 0.23	HSTPC
50824.77.....	3.61 ± 0.21	HSTPC
50835.67.....	2.49 ± 0.87	BTC
50835.68.....	3.20 ± 0.90	BTC
50835.69.....	2.56 ± 0.99	BTC
50835.70.....	3.01 ± 1.05	BTC
50835.70.....	3.26 ± 1.12	BTC
51165.71.....	−0.05 ± 0.60	BTC
51165.71.....	−0.67 ± 0.61	BTC
51165.74.....	−0.55 ± 0.71	BTC
51166.63.....	0.44 ± 2.12	BTC
51166.65.....	1.20 ± 1.28	BTC
51166.66.....	−0.67 ± 1.49	BTC
51193.59.....	0.47 ± 0.77	BTC
51193.60.....	−0.86 ± 0.79	BTC
51193.61.....	0.76 ± 0.70	BTC
51193.62.....	0.18 ± 0.73	BTC
51194.65.....	0.46 ± 0.64	BTC

^a Zero point: 25.678.

TABLE 11
SN 1997EK-*I*

Julian Day (−2,400,000)	Flux ^a	Telescope
50816.60.....	5.62 ± 1.45	BTC
50817.56.....	3.22 ± 1.30	BTC
50817.57.....	4.27 ± 1.35	BTC
50817.58.....	4.70 ± 1.40	BTC
50817.58.....	5.41 ± 1.43	BTC
50817.59.....	5.82 ± 1.36	BTC
50817.60.....	4.47 ± 1.66	BTC
50817.61.....	5.16 ± 1.52	BTC
50817.63.....	3.68 ± 1.52	BTC
50817.64.....	4.48 ± 1.48	BTC
50817.64.....	3.31 ± 1.59	BTC
50817.65.....	5.89 ± 1.23	BTC
50817.66.....	4.38 ± 1.44	BTC
50818.93.....	3.83 ± 0.16	HSTPC
50819.74.....	2.02 ± 1.70	WIYN
50819.76.....	3.05 ± 1.65	WIYN
50819.78.....	4.18 ± 1.90	WIYN
50819.79.....	1.71 ± 1.60	WIYN
50819.81.....	4.31 ± 1.57	WIYN
50819.82.....	3.84 ± 2.09	WIYN
50824.78.....	3.89 ± 0.16	HSTPC
50835.72.....	2.72 ± 1.96	BTC
50835.73.....	3.06 ± 2.05	BTC
50846.74.....	1.54 ± 0.09	HSTPC
50858.84.....	0.75 ± 0.07	HSTPC
50871.95.....	0.46 ± 0.06	HSTPC
51072.07.....	0.50 ± 0.57	KECK
51072.07.....	0.35 ± 0.58	KECK
51072.07.....	0.69 ± 0.58	KECK
51072.11.....	0.31 ± 0.55	KECK
51072.11.....	0.94 ± 0.58	KECK
51072.12.....	−0.23 ± 0.57	KECK
51101.99.....	−0.37 ± 0.54	KECK
51102.00.....	0.51 ± 0.58	KECK
51102.00.....	0.58 ± 0.59	KECK
51102.05.....	1.20 ± 0.75	KECK
51102.06.....	1.53 ± 0.90	KECK
51126.93.....	−0.04 ± 0.06	HSTPC
51134.26.....	0.06 ± 0.05	HSTPC
51165.70.....	−0.66 ± 1.15	BTC
51165.72.....	0.21 ± 1.06	BTC
51165.73.....	−0.44 ± 1.12	BTC
51193.64.....	0.01 ± 1.12	BTC
51193.65.....	−0.28 ± 1.13	BTC
51193.67.....	−0.46 ± 1.50	BTC
51194.59.....	0.99 ± 1.17	BTC
51194.60.....	1.34 ± 1.30	BTC
51194.60.....	0.73 ± 1.15	BTC

^a Zero point: 24.801.

TABLE 12
SN 1997EQ-*R*

Julian Day (−2,400,000)	Flux ^a	Telescope
50780.60.....	0.01 ± 0.12	BTC
50780.66.....	0.21 ± 0.12	BTC
50781.60.....	−0.08 ± 0.10	BTC
50781.63.....	0.19 ± 0.10	BTC
50781.68.....	0.09 ± 0.10	BTC
50781.72.....	0.14 ± 0.11	BTC
50810.61.....	1.76 ± 0.12	BTC
50810.62.....	1.80 ± 0.12	BTC
50810.63.....	1.88 ± 0.13	BTC
50810.64.....	1.87 ± 0.11	BTC
50810.70.....	1.91 ± 0.12	BTC
50810.71.....	1.82 ± 0.11	BTC
50811.70.....	1.78 ± 0.10	BTC
50818.34.....	2.23 ± 0.28	INT
50818.36.....	1.98 ± 0.24	INT
50819.85.....	1.69 ± 0.05	HSTPC
50821.66.....	2.14 ± 0.54	WIYN
50821.67.....	1.79 ± 0.39	WIYN
50835.41.....	0.85 ± 0.13	INT
50835.42.....	0.87 ± 0.18	INT
50835.43.....	0.85 ± 0.34	INT
50843.68.....	0.37 ± 0.18	WIYN
50843.70.....	0.02 ± 0.40	WIYN
50846.81.....	0.32 ± 0.02	HSTPC
50855.82.....	0.18 ± 0.02	HSTPC
50863.82.....	0.12 ± 0.02	HSTPC
51165.56.....	0.01 ± 0.12	BTC
51165.61.....	0.01 ± 0.41	BTC
51165.62.....	−0.61 ± 0.67	BTC
51165.64.....	0.00 ± 0.12	BTC
51193.58.....	−0.03 ± 0.10	BTC
51193.63.....	0.02 ± 0.09	BTC

^a Zero point: 23.284.

TABLE 13
SN 1997EQ-*I*

Julian Day (−2,400,000)	Flux ^a	Telescope
50818.37.....	1.15 ± 0.50	INT
50818.38.....	1.05 ± 0.32	INT
50818.39.....	1.20 ± 0.32	INT
50818.41.....	0.94 ± 0.49	INT
50818.43.....	1.20 ± 0.48	INT
50818.46.....	1.05 ± 0.25	INT
50819.87.....	0.91 ± 0.03	HSTPC
50821.68.....	0.93 ± 0.35	WIYN
50821.69.....	0.83 ± 0.41	WIYN
50821.70.....	0.65 ± 0.38	WIYN
50824.90.....	0.86 ± 0.02	HSTPC
50835.54.....	0.59 ± 0.27	INT
50835.56.....	0.13 ± 0.29	INT
50835.58.....	−0.11 ± 0.50	INT
50846.82.....	0.38 ± 0.02	HSTPC
50855.83.....	0.27 ± 0.02	HSTPC
50863.83.....	0.22 ± 0.01	HSTPC
51165.57.....	0.03 ± 0.29	BTC
51165.60.....	0.06 ± 0.34	BTC
51165.63.....	0.07 ± 0.20	BTC
51165.65.....	0.06 ± 0.17	BTC
51193.58.....	−0.10 ± 0.17	BTC

^a Zero point: 22.388.

TABLE 14
SN 1997EZ-*R*

Julian Day (−2,400,000)	Flux ^a	Telescope
50780.75.....	−0.41 ± 1.15	BTC
50780.82.....	−0.88 ± 0.96	BTC
50781.74.....	−1.46 ± 1.01	BTC
50781.79.....	0.29 ± 1.18	BTC
50781.79.....	1.09 ± 0.96	BTC
50811.77.....	6.05 ± 1.04	BTC
50811.77.....	3.90 ± 1.89	WIYN
50811.77.....	5.82 ± 1.03	BTC
50811.78.....	5.62 ± 1.02	BTC
50811.78.....	5.82 ± 2.22	WIYN
50811.79.....	3.97 ± 4.73	WIYN
50811.81.....	5.97 ± 1.04	BTC
50811.81.....	4.83 ± 1.16	BTC
50817.84.....	5.51 ± 1.22	BTC
50817.85.....	7.72 ± 1.63	BTC
50817.86.....	4.58 ± 2.15	BTC
50818.70.....	4.93 ± 1.13	INT
50818.72.....	5.04 ± 1.09	INT
50819.06.....	4.96 ± 0.25	HSTPC
50824.97.....	3.65 ± 0.22	HSTPC
50835.66.....	4.69 ± 1.49	INT
50835.67.....	2.88 ± 1.68	INT
50835.81.....	1.81 ± 1.49	BTC
50835.82.....	−0.07 ± 1.66	BTC
50835.83.....	0.52 ± 1.70	BTC
51193.75.....	−0.14 ± 0.74	BTC
51193.76.....	0.37 ± 0.69	BTC
51193.76.....	0.00 ± 1.08	BTC
51193.77.....	−1.23 ± 0.85	BTC
51193.78.....	−0.20 ± 0.83	BTC
51193.79.....	−0.21 ± 0.78	BTC
51193.80.....	−1.80 ± 1.63	WIYN
51195.73.....	−1.37 ± 1.26	WIYN
51195.75.....	−0.21 ± 1.40	WIYN
51195.77.....	−0.58 ± 1.18	WIYN
51195.78.....	−0.92 ± 1.36	WIYN

^a Zero point: 25.688.

TABLE 15
SN 1997EZ-*I*

Julian Day (−2,400,000)	Flux ^a	Telescope
50816.74.....	2.05 ± 1.90	BTC
50816.76.....	4.83 ± 2.03	BTC
50816.77.....	4.64 ± 1.89	BTC
50816.78.....	6.11 ± 1.90	BTC
50816.78.....	5.02 ± 2.02	BTC
50816.85.....	6.84 ± 2.14	BTC
50818.63.....	4.19 ± 2.23	INT
50818.65.....	4.24 ± 1.55	INT
50818.66.....	4.12 ± 1.54	INT
50818.68.....	4.30 ± 1.54	INT
50819.07.....	5.23 ± 0.18	HSTPC
50820.79.....	4.42 ± 1.56	WIYN
50820.81.....	5.69 ± 1.50	WIYN
50820.83.....	3.92 ± 1.46	WIYN
50820.84.....	4.22 ± 1.42	WIYN
50820.86.....	6.08 ± 1.67	WIYN
50820.87.....	3.26 ± 1.70	WIYN
50824.99.....	4.07 ± 0.17	HSTPC
50835.60.....	5.27 ± 1.77	INT
50835.61.....	0.53 ± 2.03	INT
50835.63.....	5.55 ± 1.94	INT
50835.64.....	5.62 ± 2.52	INT
50835.84.....	3.39 ± 2.13	BTC
50835.85.....	1.78 ± 2.23	BTC
50835.86.....	−0.47 ± 2.56	BTC
50846.55.....	1.77 ± 0.09	HSTPC
50858.98.....	1.00 ± 0.08	HSTPC
50871.89.....	0.48 ± 0.04	HSTPC
51189.97.....	0.80 ± 1.13	WIYN
51189.98.....	−0.74 ± 1.22	WIYN
51190.00.....	−0.20 ± 1.35	WIYN
51191.90.....	−0.54 ± 1.34	WIYN
51191.92.....	−1.64 ± 1.16	WIYN
51191.93.....	0.15 ± 1.28	WIYN
51194.70.....	−3.19 ± 2.44	BTC
51194.71.....	−1.06 ± 2.73	BTC
51194.72.....	−0.60 ± 2.43	BTC
51194.73.....	−0.52 ± 2.81	BTC
51194.74.....	−1.26 ± 2.28	BTC
51194.75.....	−0.84 ± 2.49	BTC
51194.76.....	−0.27 ± 1.90	BTC
51194.77.....	−2.00 ± 2.19	BTC
51194.78.....	−1.89 ± 2.02	BTC
51194.78.....	−1.58 ± 2.61	BTC
51194.79.....	−0.68 ± 2.38	BTC

^a Zero point: 24.954.

TABLE 16
SN 1998AS-*R*

Julian Day (−2,400,000)	Flux ^a	Telescope
50872.63.....	−0.10 ± 0.10	BTC
50872.66.....	−0.07 ± 0.09	BTC
50872.67.....	0.06 ± 0.09	BTC
50872.72.....	−0.07 ± 0.10	BTC
50872.73.....	−0.06 ± 0.11	BTC
50873.57.....	0.06 ± 0.11	BTC
50873.58.....	0.03 ± 0.10	BTC
50895.58.....	2.33 ± 0.12	BTC
50895.62.....	2.47 ± 0.15	BTC
50896.58.....	2.64 ± 0.12	BTC
50899.70.....	2.24 ± 0.12	BTC
50904.68.....	2.15 ± 0.11	BTC
50904.69.....	2.05 ± 0.10	BTC
50904.70.....	2.20 ± 0.10	BTC
50904.71.....	1.95 ± 0.11	BTC
50904.72.....	2.00 ± 0.10	BTC
50912.29.....	1.42 ± 0.04	HSTPC
50935.01.....	0.33 ± 0.02	HSTPC
50948.52.....	0.25 ± 0.02	HSTPC
50963.17.....	0.19 ± 0.02	HSTPC
51193.83.....	0.06 ± 0.08	BTC
51193.84.....	−0.07 ± 0.08	BTC
51193.86.....	0.04 ± 0.08	BTC
51196.03.....	0.21 ± 0.13	WIYN
51196.04.....	−0.19 ± 0.12	WIYN
51196.05.....	−0.11 ± 0.16	WIYN

^a Zero point: 23.139.

TABLE 17
SN 1998AS-*I*

Julian Day (−2,400,000)	Flux ^a	Telescope
50912.31.....	9.24 ± 0.21	HSTPC
50924.07.....	7.27 ± 0.19	HSTPC
50932.65.....	1.95 ± 1.56	WIYN
50935.02.....	4.86 ± 0.17	HSTPC
50948.53.....	2.57 ± 0.14	HSTPC
50963.19.....	1.79 ± 0.12	HSTPC
51194.86.....	−1.02 ± 0.98	BTC
51194.87.....	0.60 ± 1.12	BTC
51196.93.....	−0.55 ± 1.23	WIYN
51196.94.....	0.73 ± 1.12	WIYN
51196.96.....	−1.44 ± 1.28	WIYN
51280.50.....	0.53 ± 1.60	BTC
51280.51.....	−2.08 ± 1.50	BTC
51280.51.....	0.67 ± 1.50	BTC
51280.52.....	0.60 ± 1.33	BTC
51280.53.....	1.32 ± 1.45	BTC
51280.54.....	0.72 ± 1.46	BTC

^a Zero point: 24.788.

TABLE 18
SN 1998_{AW-R}

Julian Day (−2,400,000)	Flux ^a	Telescope
50513.71.....	0.08 ± 0.14	BTC
50513.73.....	−0.08 ± 0.16	BTC
50513.75.....	0.06 ± 0.13	BTC
50514.71.....	0.08 ± 0.14	BTC
50517.74.....	−0.19 ± 0.14	BTC
50517.76.....	0.04 ± 0.16	BTC
50518.79.....	0.31 ± 0.17	BTC
50518.81.....	−0.02 ± 0.17	BTC
50872.56.....	−0.03 ± 0.21	BTC
50872.59.....	−0.03 ± 0.22	BTC
50873.73.....	−0.03 ± 0.18	BTC
50873.74.....	−0.09 ± 0.15	BTC
50895.60.....	0.02 ± 0.16	BTC
50895.64.....	0.55 ± 0.16	BTC
50896.58.....	0.67 ± 0.15	BTC
50896.60.....	0.39 ± 0.16	BTC
50899.69.....	0.89 ± 0.15	BTC
50904.63.....	1.87 ± 0.14	BTC
50904.64.....	1.66 ± 0.14	BTC
50904.65.....	1.75 ± 0.13	BTC
50904.66.....	1.82 ± 0.14	BTC
50904.67.....	1.82 ± 0.14	BTC
50912.03.....	2.53 ± 0.07	HSTPC
50922.11.....	2.11 ± 0.06	HSTPC
50927.56.....	2.05 ± 0.38	BTC
50927.57.....	1.80 ± 0.34	BTC
50927.60.....	1.69 ± 0.36	BTC
50927.61.....	0.96 ± 0.41	BTC
50929.64.....	1.48 ± 0.28	WIYN
50929.65.....	1.06 ± 0.33	WIYN
50929.67.....	1.90 ± 0.31	WIYN
50933.07.....	1.32 ± 0.04	HSTPC
50947.71.....	0.58 ± 0.03	HSTPC
50961.83.....	0.30 ± 0.03	HSTPC
51192.96.....	−0.19 ± 0.26	WIYN
51192.98.....	−0.14 ± 0.39	WIYN
51193.00.....	0.18 ± 0.28	WIYN
51193.02.....	−0.14 ± 0.24	WIYN
51193.03.....	−0.29 ± 0.28	WIYN
51279.60.....	0.01 ± 0.13	BTC
51279.61.....	0.04 ± 0.14	BTC
51279.63.....	−0.04 ± 0.12	BTC
51279.66.....	0.01 ± 0.13	BTC
51280.56.....	0.14 ± 0.16	BTC
51280.57.....	0.17 ± 0.15	BTC

^a Zero point: 23.536.

TABLE 19
SN 1998_{AW-I}

Julian Day (−2,400,000)	Flux ^a	Telescope
50513.76.....	−0.33 ± 0.25	BTC
50514.74.....	−0.10 ± 0.22	BTC
50514.76.....	−0.12 ± 0.21	BTC
50514.78.....	0.06 ± 0.23	BTC
50518.73.....	0.18 ± 0.42	BTC
50518.75.....	−0.08 ± 0.34	BTC
50912.04.....	1.79 ± 0.05	HSTPC
50922.12.....	1.67 ± 0.05	HSTPC
50929.70.....	1.50 ± 0.49	WIYN
50930.71.....	1.80 ± 0.46	WIYN
50933.08.....	1.23 ± 0.03	HSTPC
50947.73.....	0.80 ± 0.03	HSTPC
50961.84.....	0.53 ± 0.03	HSTPC
51194.03.....	−0.07 ± 0.32	WIYN
51194.05.....	−0.26 ± 0.51	WIYN
51195.97.....	−0.21 ± 0.32	WIYN
51195.98.....	0.13 ± 0.27	WIYN
51196.00.....	0.10 ± 0.29	WIYN
51196.02.....	0.05 ± 0.27	WIYN
51279.59.....	−0.03 ± 0.21	BTC
51279.62.....	−0.06 ± 0.25	BTC
51279.64.....	0.15 ± 0.21	BTC
51279.65.....	0.01 ± 0.23	BTC
51279.66.....	0.19 ± 0.25	BTC
51280.55.....	0.14 ± 0.31	BTC
51280.57.....	−0.02 ± 0.28	BTC
51280.59.....	−0.30 ± 0.29	BTC
51280.60.....	0.09 ± 0.29	BTC

^a Zero point: 22.874.

TABLE 20
SN 1998_{AX-R}

Julian Day (−2,400,000)	Flux ^a	Telescope
50138.65.....	−0.03 ± 0.09	CTIO
50138.67.....	−0.09 ± 0.10	CTIO
50159.64.....	−0.09 ± 0.08	CTIO
50159.66.....	0.03 ± 0.07	CTIO
50160.67.....	0.01 ± 0.07	CTIO
50160.68.....	0.02 ± 0.06	CTIO
50168.59.....	−0.03 ± 0.07	CTIO
50168.65.....	0.14 ± 0.06	CTIO
50169.64.....	0.13 ± 0.15	CTIO
50169.67.....	−0.01 ± 0.08	CTIO
50432.83.....	−0.06 ± 0.06	CTIO
50453.84.....	−0.01 ± 0.08	CTIO
50454.77.....	0.01 ± 0.06	CTIO
50459.82.....	−0.02 ± 0.04	CTIO
50459.83.....	−0.02 ± 0.05	CTIO
50459.84.....	0.02 ± 0.05	CTIO
50490.79.....	0.01 ± 0.06	BTC
50490.79.....	0.07 ± 0.06	BTC
50490.80.....	−0.04 ± 0.06	BTC
50490.80.....	−0.04 ± 0.06	BTC
50513.71.....	−0.03 ± 0.06	BTC
50514.72.....	−0.06 ± 0.06	BTC
50872.54.....	0.72 ± 0.12	BTC
50872.57.....	0.58 ± 0.12	BTC
50873.53.....	0.84 ± 0.17	BTC
50873.55.....	0.95 ± 0.10	BTC
50895.52.....	1.42 ± 0.09	BTC
50895.55.....	1.06 ± 0.19	BTC
50895.71.....	1.24 ± 0.07	BTC
50896.53.....	1.14 ± 0.10	BTC
50900.70.....	1.14 ± 0.07	BTC
50900.71.....	1.04 ± 0.07	BTC
50904.59.....	0.91 ± 0.06	BTC
50904.60.....	0.84 ± 0.06	BTC
50904.61.....	0.81 ± 0.06	BTC
50904.62.....	0.84 ± 0.06	BTC
50904.63.....	0.89 ± 0.06	BTC
50911.96.....	0.59 ± 0.03	HSTPC
50922.04.....	0.31 ± 0.02	HSTPC
50933.00.....	0.18 ± 0.02	HSTPC
50947.65.....	0.09 ± 0.01	HSTPC
50961.23.....	0.09 ± 0.01	HSTPC
51193.80.....	−0.00 ± 0.05	BTC
51193.81.....	−0.00 ± 0.05	BTC
51193.82.....	−0.01 ± 0.06	BTC
51279.52.....	−0.01 ± 0.08	BTC
51279.57.....	0.11 ± 0.08	BTC
51280.61.....	0.06 ± 0.06	BTC

^a Zero point: 22.922.

TABLE 21
SN 1998_{AX-I}

Julian Day (−2,400,000)	Flux ^a	Telescope
50911.97.....	1.95 ± 0.10	HSTPC
50922.05.....	1.62 ± 0.10	HSTPC
50933.01.....	1.18 ± 0.06	HSTPC
50947.66.....	0.75 ± 0.05	HSTPC
50961.24.....	0.47 ± 0.04	HSTPC

^a Zero point: 23.685.

TABLE 22
SN 1998_{AY-R}

Julian Day (−2,400,000)	Flux ^a	Telescope
50521.85.....	0.02 ± 0.50	WIYN
50521.86.....	0.17 ± 0.56	WIYN
50872.54.....	2.11 ± 1.08	BTC
50872.57.....	1.27 ± 0.97	BTC
50873.53.....	0.57 ± 1.81	BTC
50873.55.....	−0.70 ± 1.04	BTC
50895.52.....	5.69 ± 0.90	BTC
50895.55.....	6.69 ± 1.91	BTC
50895.71.....	6.10 ± 0.78	BTC
50896.53.....	6.70 ± 1.24	BTC
50900.70.....	5.74 ± 0.76	BTC
50900.71.....	6.74 ± 0.91	BTC
50904.59.....	5.48 ± 0.78	BTC
50904.60.....	5.64 ± 0.75	BTC
50904.61.....	5.61 ± 0.78	BTC
50904.62.....	5.76 ± 0.82	BTC
50904.63.....	5.91 ± 0.79	BTC
50912.16.....	3.11 ± 0.20	HSTPC
50923.99.....	1.58 ± 0.17	HSTPC
51193.80.....	−0.09 ± 0.60	BTC
51193.81.....	0.61 ± 0.48	BTC
51193.82.....	0.53 ± 0.64	BTC

^a Zero point: 25.093.

TABLE 23
SN 1998_{AY-I}

Julian Day (−2,400,000)	Flux ^a	Telescope
50912.17.....	1.56 ± 0.08	HSTPC
50924.00.....	0.96 ± 0.07	HSTPC
50934.68.....	0.61 ± 0.04	HSTPC
50948.59.....	0.40 ± 0.04	HSTPC
50967.81.....	0.26 ± 0.04	HSTPC

^a Zero point: 23.685.

TABLE 24
SN 1998BA-*R*

Julian Day (−2,400,000)	Flux ^a	Telescope
50873.79.....	0.03 ± 0.09	BTC
50873.80.....	0.09 ± 0.09	BTC
50873.81.....	0.01 ± 0.09	BTC
50873.82.....	0.03 ± 0.09	BTC
50873.83.....	0.01 ± 0.08	BTC
50873.84.....	−0.03 ± 0.09	BTC
50895.78.....	1.50 ± 0.14	BTC
50895.85.....	1.64 ± 0.15	BTC
50899.75.....	1.52 ± 0.11	BTC
50899.84.....	1.43 ± 0.14	BTC
50899.90.....	1.20 ± 0.21	BTC
50900.74.....	1.54 ± 0.10	BTC
50900.75.....	1.32 ± 0.10	BTC
50904.77.....	1.36 ± 0.11	BTC
50904.78.....	1.20 ± 0.11	BTC
50904.79.....	1.42 ± 0.13	BTC
50904.80.....	1.30 ± 0.09	BTC
50904.81.....	1.34 ± 0.11	BTC
50912.10.....	0.79 ± 0.03	HSTPC
50923.12.....	0.41 ± 0.02	HSTPC
50933.21.....	0.22 ± 0.02	HSTPC
50947.12.....	0.12 ± 0.01	HSTPC
50961.90.....	0.12 ± 0.01	HSTPC
51258.01.....	−0.15 ± 0.11	WIYN
51279.82.....	0.07 ± 0.08	BTC
51279.85.....	−0.05 ± 0.10	BTC
51280.69.....	−0.02 ± 0.07	BTC
51280.70.....	0.03 ± 0.06	BTC

^a Zero point: 22.779.

TABLE 25
SN 1998BA-*I*

Julian Day (−2,400,000)	Flux ^a	Telescope
50907.82.....	3.18 ± 1.99	WIYN
50907.83.....	3.96 ± 1.75	WIYN
50907.84.....	6.80 ± 1.81	WIYN
50907.85.....	6.04 ± 2.36	WIYN
50912.11.....	5.74 ± 0.22	HSTPC
50923.13.....	3.95 ± 0.21	HSTPC
50933.22.....	2.81 ± 0.12	HSTPC
50947.13.....	1.57 ± 0.10	HSTPC
50961.92.....	1.37 ± 0.10	HSTPC
51279.83.....	−1.51 ± 1.00	BTC
51279.84.....	0.88 ± 1.09	BTC
51280.69.....	−1.04 ± 0.83	BTC
51280.71.....	0.66 ± 0.72	BTC
51280.72.....	−0.06 ± 0.68	BTC
51280.73.....	0.13 ± 0.68	BTC

^a Zero point: 24.477.

TABLE 26
SN 1998BE-*R*

Julian Day (−2,400,000)	Flux ^a	Telescope
50490.86.....	0.49 ± 0.55	BTC
50490.87.....	−0.39 ± 0.54	BTC
50513.83.....	−0.02 ± 0.52	BTC
50513.84.....	0.15 ± 0.54	BTC
50514.83.....	0.53 ± 0.60	BTC
50514.86.....	−0.51 ± 0.53	BTC
50517.88.....	0.33 ± 0.70	BTC
50517.90.....	−0.26 ± 0.71	BTC
50517.90.....	0.69 ± 0.81	BTC
50518.86.....	0.22 ± 0.62	BTC
50518.87.....	0.57 ± 0.66	BTC
50872.74.....	−0.75 ± 0.91	BTC
50872.89.....	1.36 ± 0.93	BTC
50873.87.....	0.63 ± 0.53	BTC
50895.78.....	4.22 ± 0.70	BTC
50895.84.....	5.34 ± 0.88	BTC
50899.75.....	7.13 ± 0.79	BTC
50899.82.....	6.98 ± 0.91	BTC
50900.76.....	4.64 ± 0.65	BTC
50904.73.....	6.58 ± 0.65	BTC
50904.74.....	6.90 ± 0.67	BTC
50904.75.....	6.31 ± 0.72	BTC
50904.75.....	7.32 ± 0.73	BTC
50904.76.....	8.29 ± 0.76	BTC
50904.86.....	7.95 ± 0.89	BTC
50912.23.....	5.73 ± 0.25	HSTPC
50923.19.....	2.11 ± 0.18	HSTPC
50932.74.....	2.04 ± 0.89	WIYN
50932.77.....	1.38 ± 0.93	WIYN
50934.08.....	0.73 ± 0.12	HSTPC
50949.00.....	0.76 ± 0.13	HSTPC
50962.17.....	0.21 ± 0.13	HSTPC
51279.68.....	−0.16 ± 0.67	BTC
51279.71.....	0.31 ± 0.68	BTC
51279.75.....	0.21 ± 0.73	BTC
51279.77.....	−0.30 ± 0.79	BTC

^a Zero point: 25.350.

TABLE 27
SN 1998BE-*I*

Julian Day (−2,400,000)	Flux ^a	Telescope
50514.85.....	-0.21 ± 0.83	BTC
50514.87.....	-1.02 ± 0.78	BTC
50518.84.....	2.00 ± 0.90	BTC
50518.85.....	1.47 ± 0.86	BTC
50518.85.....	0.31 ± 0.82	BTC
50912.25.....	3.66 ± 0.18	HSTPC
50923.20.....	2.19 ± 0.17	HSTPC
50932.80.....	2.35 ± 1.10	WIYN
50932.85.....	2.26 ± 0.92	WIYN
50934.09.....	1.13 ± 0.09	HSTPC
50949.01.....	0.80 ± 0.08	HSTPC
50962.19.....	0.37 ± 0.08	HSTPC
51279.69.....	0.81 ± 0.89	BTC
51279.70.....	0.49 ± 0.87	BTC
51279.72.....	1.51 ± 0.73	BTC
51279.73.....	-0.02 ± 0.71	BTC
51279.76.....	0.62 ± 0.83	BTC
51279.77.....	0.58 ± 0.85	BTC
51280.64.....	-0.87 ± 0.82	BTC
51280.64.....	0.36 ± 0.84	BTC
51280.65.....	0.12 ± 0.73	BTC
51280.66.....	-0.13 ± 0.78	BTC
51280.67.....	1.24 ± 0.76	BTC
51280.68.....	-0.62 ± 0.76	BTC

^a Zero point: 24.384.

TABLE 28
SN 1998BI-*R*

Julian Day (−2,400,000)	Flux ^a	Telescope
50138.79.....	-1.04 ± 0.91	CTIO
50138.82.....	0.85 ± 0.86	CTIO
50168.80.....	-0.68 ± 0.66	CTIO
50490.86.....	0.40 ± 0.49	BTC
50490.87.....	-0.09 ± 0.48	BTC
50513.83.....	0.26 ± 0.51	BTC
50513.84.....	-0.10 ± 0.53	BTC
50514.83.....	-1.06 ± 0.58	BTC
50514.86.....	-0.05 ± 0.50	BTC
50517.88.....	0.13 ± 0.65	BTC
50517.89.....	-0.11 ± 0.60	BTC
50517.89.....	0.93 ± 0.60	BTC
50517.90.....	-0.29 ± 0.68	BTC
50517.90.....	-0.35 ± 0.74	BTC
50872.89.....	0.52 ± 0.81	BTC
50873.87.....	0.60 ± 0.51	BTC
50895.78.....	3.15 ± 0.63	BTC
50895.84.....	3.11 ± 0.79	BTC
50899.75.....	4.93 ± 0.65	BTC
50899.82.....	4.28 ± 0.70	BTC
50900.76.....	4.44 ± 0.55	BTC
50904.73.....	6.10 ± 0.61	BTC
50904.75.....	5.30 ± 0.61	BTC
50904.75.....	5.38 ± 0.64	BTC
50904.76.....	6.21 ± 0.66	BTC
50904.86.....	5.27 ± 0.77	BTC
50910.15.....	5.27 ± 0.20	HSTPC
50922.18.....	3.75 ± 0.18	HSTPC
51279.71.....	0.94 ± 0.73	BTC
51279.74.....	0.63 ± 0.67	BTC
51279.75.....	-1.14 ± 0.68	BTC
51279.77.....	0.47 ± 0.76	BTC

^a Zero point: 25.213.

TABLE 29
SN 1998BI-*I*

Julian Day (−2,400,000)	Flux ^a	Telescope
50910.16.....	2.07 ± 0.06	HSTPC
50922.20.....	1.83 ± 0.06	HSTPC
50931.99.....	1.25 ± 0.04	HSTPC
50946.38.....	0.54 ± 0.03	HSTPC
50966.88.....	0.20 ± 0.02	HSTPC

^a Zero point: 23.685.

TABLE 30
SN 2000FR-R

Julian Day (−2,400,000)	Flux ^a	Telescope
51671.77.....	1.02 ± 0.07	KECK
51671.77.....	1.05 ± 0.07	KECK
51671.78.....	1.06 ± 0.07	KECK
51671.78.....	0.99 ± 0.07	KECK
51679.98.....	1.66 ± 0.04	HSTPC
51692.91.....	1.43 ± 0.03	HSTPC
51706.26.....	0.73 ± 0.02	HSTPC
51718.04.....	0.39 ± 0.01	HSTPC
51733.86.....	0.16 ± 0.01	HSTPC
52014.72.....	−0.01 ± 0.07	NTT
52014.73.....	−0.08 ± 0.07	NTT
52014.74.....	0.04 ± 0.08	NTT
52014.75.....	−0.04 ± 0.06	NTT
52014.76.....	−0.04 ± 0.07	NTT
52014.77.....	−0.08 ± 0.10	NTT
52014.78.....	−0.07 ± 0.09	NTT
52014.79.....	−0.04 ± 0.10	NTT
52014.80.....	−0.16 ± 0.14	NTT
52376.98.....	0.01 ± 0.04	CFHT
52376.99.....	−0.00 ± 0.03	CFHT
52377.04.....	0.01 ± 0.04	CFHT
52377.05.....	−0.02 ± 0.04	CFHT
52382.01.....	0.03 ± 0.05	CFHT
52384.98.....	−0.00 ± 0.09	CFHT
52386.85.....	−0.14 ± 0.10	CFHT

^a Zero point: 22.998.TABLE 31
SN 2000FR-I

Julian Day (−2,400,000)	Flux ^a	Telescope
51641.99.....	0.03 ± 0.04	CFHT
51664.95.....	0.40 ± 0.05	CFHT
51664.99.....	0.40 ± 0.06	CFHT
51672.86.....	1.14 ± 0.02	HSTPC
51679.97.....	1.59 ± 0.03	HSTPC
51692.91.....	1.46 ± 0.03	HSTPC
51706.20.....	1.02 ± 0.03	HSTPC
51717.98.....	0.66 ± 0.02	HSTPC
51733.79.....	0.40 ± 0.02	HSTPC
51997.93.....	0.05 ± 0.06	CFHT
51997.94.....	0.01 ± 0.06	CFHT
51997.99.....	0.19 ± 0.05	CFHT
51998.00.....	0.03 ± 0.06	CFHT
51998.01.....	0.08 ± 0.06	CFHT
52376.96.....	0.04 ± 0.06	CFHT
52376.97.....	−0.06 ± 0.06	CFHT
52377.00.....	0.13 ± 0.06	CFHT
52377.00.....	−0.09 ± 0.06	CFHT
52377.01.....	−0.01 ± 0.06	CFHT
52377.03.....	0.01 ± 0.07	CFHT

^a Zero point: 22.805.

REFERENCES

- Aguirre, A. 1999a, *ApJ*, 512, L19
—, 1999b, *ApJ*, 525, 583
Aguirre, A., & Zoltan, H. 2000, *ApJ*, 532, 28
Alcock, C., et al. 2000, *ApJ*, 542, 281
Aldering, G., Knop, R., & Nugent, P. 2000, *AJ*, 119, 2110
Allen, A. W., Schmidt, R. W., & Fabian, A. C. 2002, *MNRAS*, 334, L11
Amanullah, R., Mörtzell, E., & Goobar, A. 2003, *A&A*, 397, 819
Appenzeller, I., et al. 1998, *Messenger*, 94, 1
Bahcall, N. A., Ostriker, J. P., Perlmutter, S., & Steinhardt, P. J. 1999, *Science*, 284, 1481
Bahcall, N. A., et al. 2003, *ApJ*, 585, 182
Benitez, N., Riess, A., Nugent, P., Dickinson, M., Chornock, R., & Filippenko, A. V. 2002, *ApJ*, 577, L1
Bennett, C. L., et al. 2003, *ApJ*, 588, 331
Bergström, L., Goliath, M., Goobar, A., & Mörtzell, E. 2000, *A&A*, 358, 13
Bessell, M. S. 1990, *PASP*, 102, 1181
Blakeslee, J. P., et al. 2003, *ApJ*, 589, 693
Branch, D., Romanishin, W., & Baron, E. 1996, *ApJ*, 465, 73
Branch, D., & van den Bergh, S. 1993, *AJ*, 105, 2231
Cardelli, J. A., Clayton, G. C., & Mathis, J. S. 1989, *ApJ*, 345, 245
Coil, A. L., et al. 2000, *ApJ*, 544, L111
Csáki, C., Kaloper, N., & Terning, J. 2002, *Phys. Rev. Lett.*, 88, 1302
Dalal, N., Holz, D. E., Chen, X., & Frieman, J. A. 2003, *ApJ*, 585, L11
Dolphin, A. E. 2000, *PASP*, 112, 1397
—, 2003, *WFPC2 CTE Characterization*
Efstathiou, G., et al. 2002, *MNRAS*, 330, L29
Falco, E. E., et al. 1999, *ApJ*, 523, 617
Frieman, J. A. 1997, *Comments Astrophys.*, 18, 323
Garnavich, P. M., et al. 1998a, *ApJ*, 493, L53
—, 1998b, *ApJ*, 509, 74
Goldhaber, G., et al. 2001, *ApJ*, 558, 359
Goobar, A., Bergström, L., & Mörtzell, E. 2002a, *A&A*, 384, 1
Goobar, A., Mörtzell, E., Amanullah, R., Goliath, M., Bergström, L., & Dahlén, T. 2002b, *A&A*, 392, 757
Hamuy, M., Phillips, M. M., Maza, J., Wischnjewsky, M., Uomoto, A., Landolt, A. U., & Khatwani, R. 1991, *AJ*, 102, 208
Hamuy, M., Phillips, M. M., Suntzeff, N. B., Schommer, R. A., Maza, J., & Aviles, R. 1996a, *AJ*, 112, 2391
Hamuy, M., Trager, S. C., Pinto, P. A., Phillips, M. M., Schommer, R. A., Ivanov, V., & Suntzeff, N. B. 2000, *AJ*, 120, 1479 (erratum 122, 3506 [2001])
Hamuy, M., et al. 1996b, *AJ*, 112, 2408 (H96)
Hatano, K., Branch, D., & Deaton, J. 1998, *ApJ*, 502, 177
Hawkins, E., et al. 2002, *MNRAS*, submitted
Henry, R. B. C., & Worthey, G. 1999, *PASP*, 111, 919
Hoeftich, P., Wheeler, J. C., & Thielmann, F. K. 1998, *ApJ*, 495, 617
Holtzman, J. A., Burrows, C. J., Casertano, S., Hester, J. J., Traugher, J. T., Watson, A. M., & Worthey, G. 1995, *PASP*, 107, 1065
Holz, D. E. 1998, *ApJ*, 506, L1
—, 2001, *ApJ*, 556, L71
Howell, D. A. 2001, *ApJ*, 554, L193
Ivanov, V. D., Hamuy, M., & Pinto, P. A. 2000, *ApJ*, 542, 588
Jaffe, A. H., et al. 2001, *Phys. Rev. Lett.*, 86, 3475
James, F., & Roos, M. 1975, *Comput. Phys. Commun.*, 10, 343
Jha, S. 2002, Ph.D. thesis, Harvard Univ.
Kantowski, R. 1998, *ApJ*, 507, 483
Kim, A., Goobar, A., & Perlmutter, S. 1996, *PASP*, 108, 190
Kim, A., Linder, E., Miquel, R., & Mostek, N. 2003, *MNRAS*, submitted
Kobayashi, C., Tsujimoto, T., Nomoto, K., Hachisu, I., & Kato, M. 1998, *ApJ*, 503, L155
Krist, J., & Hook, R. 2003, *The Tiny Tim Users Guide*
Landolt, A. U. 1992, *AJ*, 104, 340
Leibundgut, B. 2001, *ARA&A*, 39, 67
Lentz, E. J., Baron, E., Branch, D., Hauschildt, P. H., & Nugent, P. E. 2000, *ApJ*, 530, 966
Lewis, G. F., & Ibata, R. A. 2001, *MNRAS*, 324, L25
Li, W., Filippenko, A. V., & Riess, A. G. 2001, *ApJ*, 546, 719
Linder, E. V., & Jenkins, A. 2003, *MNRAS*, submitted
Lira, P., et al. 1998, *AJ*, 115, 234
Malmquist, K. G. 1924, *Medd. Lund. Astron. Obs. Ser. II*, 32, 64
—, 1936, *Stockholm Observatory Medd.*, 26
Metcalf, R. B. 1999, *MNRAS*, 305, 746
Metcalf, R. B., & Silk, J. 1999, *ApJ*, 519, L1
Minty, E. M., Heavens, A. F., & Hawkins, M. R. S. 2002, *MNRAS*, 330, 378
Mörtzell, E., Bergström, L., & Goobar, A. 2002, *Phys. Rev. D*, 66, 047702
Mörtzell, E., & Goobar, A. 2003, *J. Cosmology Astropart. Phys.*, 04, 003
Mörtzell, E., Gunnarsson, C., & Goobar, A. 2001, *ApJ*, 561, 106
Nobili, S., Goobar, A., Knop, R., & Nugent, P. 2003, *A&A*, 404, 901
Nomoto, K., Nakamura, T., & Kobayashi, C. 1999, *Ap&SS*, 265, 37
Nugent, P., Kim, A., & Perlmutter, S. 2002, *PASP*, 114, 803
Nugent, P., Phillips, M., Baron, E., Branch, D., & Hauschildt, P. 1995, *ApJ*, 455, L147

- O'Donnell, J. E. 1994, *ApJ*, 422, 158
- Oguri, M., Suto, Y., & Turner, E. L. 2003, *ApJ*, 583, 584
- Oke, J. B., et al. 1995, *PASP*, 107, 375
- Perlmutter, S., & Schmidt, B. 2003, in *Supernovae and Gamma Ray Bursts*, ed. K. Weiler (Berlin: Springer)
- Perlmutter, S., et al. 1995, *ApJ*, 440, L41
- . 1997, *ApJ*, 483, 565
- . 1998, *Nature*, 391, 51
- . 1999, *ApJ*, 517, 565 (P99)
- Phillips, M. M. 1993, *ApJ*, 413, L105
- Phillips, M. M., Lira, P., Suntzeff, N. B., Schommer, R. A., Hamuy, M., & Maza, J. 1999, *AJ*, 118, 1766
- Richmond, M. W., et al. 1995, *AJ*, 109, 2121
- Riess, A. G., Filippenko, A. V., Li, W., & Schmidt, B. P. 1999a, *AJ*, 118, 2668
- Riess, A. G., et al. 1998, *AJ*, 116, 1009
- . 1999b, *AJ*, 117, 707 (R99)
- . 2000, *ApJ*, 536, 62
- . 2001, *ApJ*, 560, 49
- Rowan-Robinson, M. 2002, *MNRAS*, 332, 352
- Ruiz-Lapuente, P. 2003, in *3K, SNs, Clusters: Hunting the Cosmological Parameters*, ed. D. Barbosa et al. (Dordrecht: Kluwer)
- Schlegel, D. J., Finkbeiner, D. P., & Davis, M. 1998, *ApJ*, 500, 525
- Schmidt, B. P., et al. 1998, *ApJ*, 507, 46
- Seljok, U., & Holz, D. E. 1999, *A&A*, 351, L10
- Spergel, D. N., et al. 2003, *ApJS*, 148, 175
- Sullivan, M., et al. 2003, *MNRAS*, 340, 1057
- Suntzeff, N. B., et al. 1999, *AJ*, 117, 1175
- Tonry, J., et al. 2003, *ApJ*, 594, 1
- Turner, M. 2001, *PASP*, 113, 653
- Verde, L., et al. 2002, *MNRAS*, 335, 432
- Wambsganss, J., Cen, R., Xu, G., & Ostriker, J. P. 1997, *ApJ*, 475, L81
- Wang, L., Goldhaber, G., Aldering, G., & Perlmutter, S. 2003, *ApJ*, 590, 944
- Wang, L., Hoeflich, P., & Wheeler, J. C. 1997, *ApJ*, 483, L29
- Wang, Y., Holz, D. E., & Munshi, D. 2002, *ApJ*, 572, L15
- Wells, L. A., et al. 1994, *AJ*, 108, 2233
- Whitmore, B., Heyer, I., & Casertano, S. 1999, *PASP*, 111, 1559
- Wu, H., Yan, H. J., & Zou, Z. L. 1995, *A&A*, 294, L9